PCCP

PERSPECTIVE

View Article Online
View Journal | View Issue

Cite this: *Phys. Chem. Chem. Phys.*, 2014, **16**, 1719

Principles of phosphorescent organic light emitting devices

Boris Minaev,*[ab] Gleb Baryshnikov[b] and Hans Agren[a]

Received 6th September 2013,
Accepted 15th October 2013

DOI: 10.1039/c3cp53806k

www.rsc.org/pccp

Organic light-emitting device (OLED) technology has found numerous applications in the development of solid state lighting, flat panel displays and flexible screens. These applications are already commercialized in mobile phones and TV sets. White OLEDs are of especial importance for lighting; they now use multilayer combinations of organic and elementoorganic dyes which emit various colors in the red, green and blue parts of the visible spectrum. At the same time the stability of phosphorescent blue emitters is still a major challenge for OLED applications. In this review we highlight the basic principles and the main mechanisms behind phosphorescent light emission of various classes of photofunctional OLED materials, like organic polymers and oligomers, electron and hole transport molecules, elementoorganic complexes with heavy metal central ions, and clarify connections between the main features of electronic structure and the photo-physical properties of the phosphorescent OLED materials.

1. Introduction

The phenomenon of electroluminescence (EL) by which materials emit light in response to an applied voltage is widely used in modern lighting technology. This electroluminescence should be distinguished from black body radiation when light results from heating by an electric current (incandescence). Usually EL results from radiative recombination of electrons and holes in a photo-electrofunctional material, typically a semiconductor. The first traditional inorganic EL device, based on gallium arsenide (GaAs), was developed and become available in the 1960s in the form of light-emitting diodes (LEDs).[1] In such inorganic LED devices the electrons and holes may be separated prior to recombination by doping the material to

[a] *Division of Theoretical Chemistry and Biology, School of Biotechnology, KTH Royal Institute of Technology, SE-106 91 Stockholm, Sweden. E-mail: boris@theochem.kth.se*
[b] *Bohdan Khmelnytsky National University, 18031 Cherkasy, Ukraine. E-mail: bfmin@rambler.ru*

Boris Minaev

Boris Minaev was born in Yekateriburg, Russia in 1943. He graduated from Tomsk State University with a PhD in physics on EPR and phosphorescence lifetime calculations. In 1974 he became assistant professor at Karaganda State University, Kazakhstan and chief of physical chemistry in 1976. Since 2007 he has been chief of the Organic Chemistry Department and director of Scientific Institute of Physics and Chemistry of Functional Materials at Bogdan Khmelnitsky National University in Cherkassy. He has delivered lectures as a guest professor at the Royal Institute of Technology. Prof. Minaev is a specialist in the field of spin chemistry and phosphorescence theory.

Gleb Baryshnikov

Gleb Baryshnikov was born 1989 in the town of Kramatorsk in the eastern Ukraine. He graduated 2011 in Ukraine and then continued his study in the graduate school under the supervision of Prof. B. Minaev. Gleb Baryshnikov is the winner of the young scientist's prize of the National Academy of Sciences of Ukraine (2012) for the work in theoretical design of structure and spectral properties of sensitizing dyes for DSSCs. Gleb Baryshnikov is an author of 30 publications in international journals. His research interests are focused on heterocirculenes photophysical properties and theoretical design of organic materials for the DSSCs.

form a p–n junction. The EL phenomenon was observed for the first time in ZnS phosphors as early as 1936.[2] Other typical inorganic EL materials comprise indium phosphide, powdered zinc sulfide doped with manganese (producing an orange–red color), with copper (greenish light) or with silver dopants (producing bright blue color).[1] Thus white light can be provided with LED technology.

Beside these inorganic EL devices and fluorescent lamps, new organic light-emitting diodes (OLEDs) have increasingly become popular in recent decades; these are progressive techniques incorporated into lighting industry being important alternatives to incandescent lamps. Nowadays, it is widely assumed that phosphorescent OLEDs, based on organic complexes with heavy metals, are required to reach sufficiently high efficiencies. However, still some problems exist, such as good quality blue emission light, and the search for better photofunctional materials for OLEDs remains a great challenge.

In connection to a historical analysis of OLED development one should mention the discovery in 1947 concerning a transparent anode constructed by depositing a layer of indium tin oxide (ITO) onto a glass surface.[1] This discovery opened the possibility to obtain the light-emitting planar surfaces used in all modern OLED applications. The fact that many organic π-conjugated molecules and dyes possess intense luminescence[3,4] indicated their potential use in EL devices and the first observation of organic electroluminescence came already in the early 1950s: Andre Bernanose *et al.*[5] applied high-voltage alternating current fields to the acridine orange dye, deposited on cellophane thin films and detected EL as the dye fluorescence.

Another important observation of organic EL based on molecular single crystals was made by Martin Pope *et al.* with the first fabrication of a monolayer EL device.[6,7] They observed for the first time a direct current electroluminescence applying a high voltage to the pure single crystal of anthracene under vacuum. While the double injection mechanism and correct explanation of the anthracene single crystal EL as an electron–hole recombination was given as long as a half-a-century ago,[8] the organic EL phenomenon remained unexploited for a long time because the anthracene single crystals used that time were expensive and difficult to process.[7,9] Practical applications of this scientific achievement were hindered by the need for high voltage (about 400 V) and a large size of the high-quality single crystal. Thus large scale applications of the organic light-emitting diode (OLED) technique based on monolayer single-crystal EL were not developed at that time.

The first efficient organic electroluminescent diode was fabricated by Tang and VanSlyke[10] at Eastman Kodak in 1987. It was constructed as a double layered organic thin film sandwiched between two electrodes. One layer consisting of aromatic diamine was capable of only hole transport, while the second organic layer composed of a tris(8-hydroxyquinoline) aluminium (Alq_3)[10] film was used as a light emitter (Fig. 1) being in the micro crystalline form with a nano grain size. The Alq_3 microcrystal provides, besides emission, an efficient electron transport from the cathode.

Such an emissive layer has proven to be very useful[11] and boosted further progress in OLED technology accompanied by the development of new polymers and doping materials.[9] This novel two-layer structure with separated hole transporting and electron transporting layers leads to the result that electron–hole recombination and light emission occurs in the middle of the organic layer. This provides a reduction in the operating voltage and improvements in the device efficiency.[10] It led finally to the current era of OLED research and production.

Nowadays the display market is still dominated by liquid crystal displays with amorphous silicon thin-film transistor backplanes processed on glass.[9] Within the last years, active-matrix OLED displays have rapidly expanded their market.[9b] The incorporation of different polymers in the interlayer, like parylene and polyphenylene vinylene (PPV), has been optimized in terms of their deposition and patterning in order to use a low temperature process for making organic backplanes for OLED displays.[9b]

The OLED research is thus growing due to their potential for future flat panel displays and solid state lighting applications. The first OLEDs were commercialized in 1997 as flat displays in the form of organic polymers in which only singlet excitons are

Hans Agren

Hans Ågren was born 1950 in the town of Skellefteå in northern Sweden. He graduated in 1979 with a PhD in experimental atomic and molecular physics at the University of Uppsala under the supervision of Kai Siegbahn and became assistant professor in Quantum Chemistry there in 1983. He became the first holder of the chairs in Computational Physics at Linköping University in 1991 and in Theoretical Chemistry at the Royal Institute of Technology, Stockholm, in 1998. He heads the Department of Theoretical Chemistry and Biology at KTH with research activities in theoretical modeling, molecular/nano/biophotonics and electronics, catalysis and X-ray science.

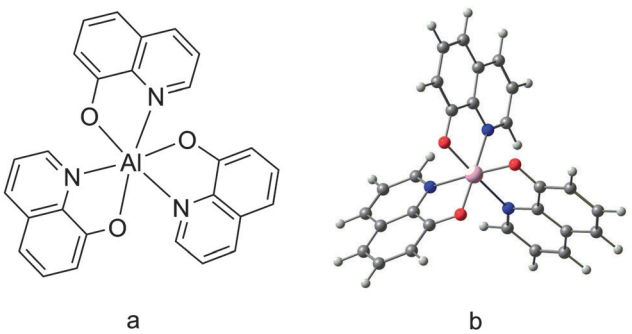

Fig. 1 Structure (a) and (b) 3D model of the Alq_3 complex.

light emitting. Spin–orbit coupling (SOC) effects are very weak in organic molecules and electrically generated triplet excitons (in ratio 3 : 1 to singlets) are then not emissive. Full use of all singlet and triplet excitons and 100% of internal quantum efficiency in OLEDs are possible when SOC effects provide strong mixing of spin multiplets. This is in fact realized in heavy element (Ir, Pt) complexes with organic ligands when the triplet state emission harnesses all electro-generated excitons. This approach has begun to develop since 1998 and the first such phosphorescent red OLED has already been used in mobile phones in 2003 as sun-displays. Recently red, green and blue (RGB) platforms of highly efficient phosphorescent dyes have been achieved and OLEDs TV is now undergoing commercialization.

Since the SOC effects play a crucial role in modern OLED we present in this review a general introduction of basic principles of electroluminescence in organic semiconductors in order to illustrate how the spin of many electron systems provides control of OLED efficiency. We then consider the nature of atomic multiplet splitting with the method of SOC calculations and how the results of this can be used in the explanation and rational design of efficient photofunctional materials for modern OLED devices.

2. Principles of organic electroluminescence

2.1. Operation principle of organic light emitting diodes

Organic unsaturated molecules in the form of polymers and crystals are electrically conductive because of the delocalization of π electrons, which can provide conjugation over the whole species.[6] The corresponding materials exhibit various conductivity levels ranging from insulators to conductors, and are therefore considered as organic semiconductors. The highest occupied and lowest unoccupied molecular orbitals (HOMO and LUMO) of such organic semiconductors are analogous to the valence and conduction bands of inorganic species like GaAs.[9]

To illustrate the principles of polymeric OLED operation we present a simple scheme (Fig. 2). In this scheme the monomer molecules, denoted by a circle with the HOMO (ϕ_i) and LUMO (ϕ_u) inside, present the polymer chain. This can be PPV, for example, representing one layer, as it was realized by Burroughes *et al.*[12] in the first polymeric OLED. In the ground state of the polymer, Fig. 2a, all conjugated PPV molecules have closed-shell structure (the HOMO is doubly occupied) each being in the singlet ground state (S_0). The homogeneous and dense PPV film (100 nm thick) formed on a bottom electrode (indium oxide deposited by ion-beam sputtering), is typically used as the anode (left side in Fig. 2), in the fabricated OLED device.[12] In the form of the cathode (electron-injecting contact) alkali-earth metals, or aluminum, magnesium silver alloys and amorphous silicon hydrogen alloys, are suitable (right side in Fig. 2). Usually a number of layers of different electron- and hole-conductive materials are implemented in modern multilayer OLEDs. The electron conductive layers can be introduced near the cathode for more effective electron transfer to the emissive layer; the additional hole-conductive film, such as CuI, can also cover the ITO-anode for better transfer of the injected holes.[13] Fig. 2 just represents one emitting layer of the organic thin film, or molecular single crystal in the experiments of Martin Pope *et al.*,[6,7] which oversimplifies the real structure of a modern multilayer OLED.

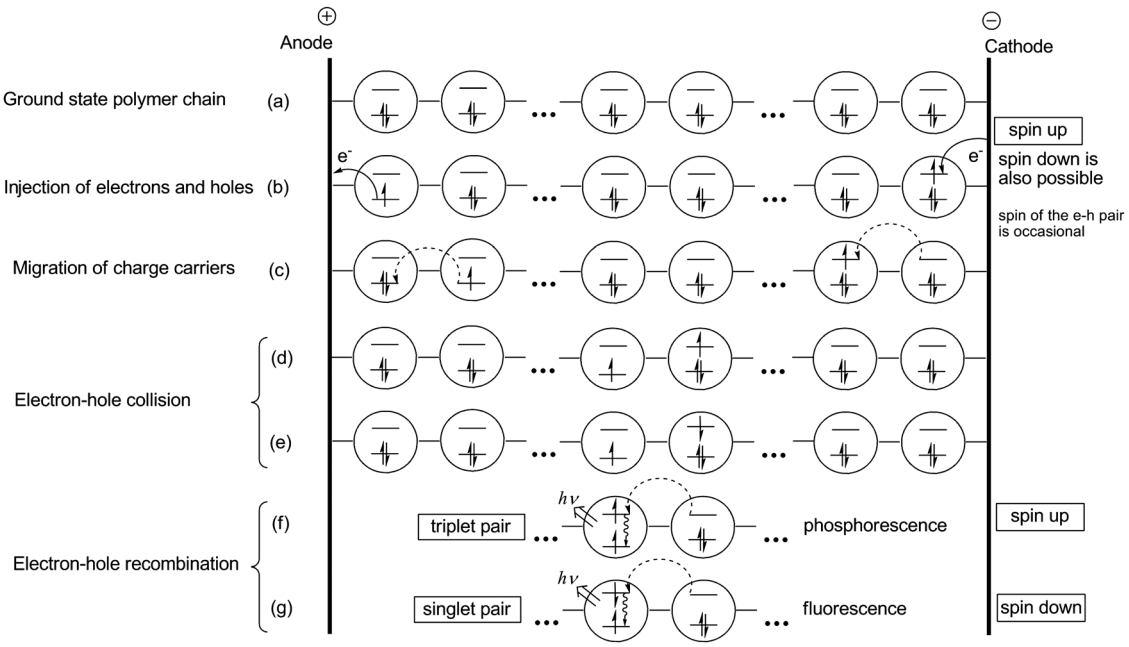

Fig. 2 Scheme of EL generation in a polymer chain.

Electrons and holes are injected by applying a bias, Fig. 2b. The threshold for substantial charge injection in the OLED device of Burroughes *et al.* was just below 14 V and the light output was almost linear with current.[12] This means that the charge carriers migrate through the polymer being driven by the applied voltage right from the beginning, Fig. 2c. At shorter distances between electrons and holes they start to attract each other and form excitons, Fig. 2d and e. This is analogous to ion–radical pairs in solvents,[14] but with a rather different type of diffusion mechanism. One should note that both electrons (LUMO) and holes (singly occupied HOMO) have arbitrary spin from the beginning of the injection processes, and are not spin-correlated. If the spin-down electron is transferred to the anode (and spin-up hole is created), as shown in the left side of Fig. 2b, any spin orientation is possible for the injected electron from the cathode. On the right side of Fig. 2b the spin-up electron is shown: thus the electron–hole (e–h) pair is present in the common triplet (T) spin state by addition of the two parallel spins. At the same time, the spin-down electron at the cathode can also be injected. In this case, the electron–hole pair will have singlet (S) spin state (zero total spin). This is schematically shown as (d) and (e) examples in Fig. 2, for the T and S e–h pairs, respectively. Since we do not deal with spintronic devices in this review,[11] the electrode materials considered are not able to inject spin-polarised charge carriers. Furthermore, since the cathode- and anode-injective processes are not spin-correlated, the T and S pair formation events are equally probable. In order to describe S and T states in terms of a HOMO–LUMO approach one can consider their wave function Ψ as a product of the spatial (Φ_{i-u}) and spin (Ω) parts:[15]

$$\Psi = \Phi\cdot\Omega, \tag{1}$$

$$^{1,3}\Phi_{i-u} = \frac{1}{\sqrt{2}}[\phi_i(1)\phi_u(2) \pm \phi_i(2)\phi_u(1)], \tag{2}$$

where sign "+" corresponds to the singlet state $^1\Phi$ and sign "−" corresponds to the triplet spatial state $^3\Phi$, $\phi_i(1)$ means HOMO, which depends on the spatial coordinates x_1, y_1, z_1 of the first electron, $\phi_u(2)$ means LUMO, which depends on the spatial coordinates x_2, y_2, z_2 of the second electron. In general, all spin functions are determined through the S^2 operator:

$$S^2\Omega = S(S+1)\hbar^2\Omega, \tag{3}$$

where Ω is a spin eigen-function and S is the total spin quantum number, respectively. For the triplet state $S = 1$ and for the singlet state $S = 0$; Ω is also an eigen-function of the S_z operator; this is a projection of the total spin on the z-axis (in the case of external magnetic field directed along the z-axis):

$$S_z\Omega = M_S\hbar\Omega, \tag{4}$$

where M_S quantum number is equal to zero for the singlet state; $M_S = \pm1, 0$ for the triplet. For two electrons the triplet state spin functions $^3\Omega$ can be determined in a form of the $|S,S_z\rangle$ eigenfunctions for three substates like the following:

$$\begin{aligned} &|1,1\rangle = \alpha(1)\alpha(2); \quad |1,-1\rangle = \beta(1)\beta(2); \\ &|1,0\rangle = \left(1/\sqrt{2}\right)[\alpha(1)\beta(2) + \beta(1)\alpha(2)] \end{aligned} \tag{5}$$

and for the singlet state

$$^1\Omega = |0,0\rangle = \left(1/\sqrt{2}\right)[\alpha(1)\beta(2) - \beta(1)\alpha(2)], \tag{6}$$

where α and β are eigenfunctions of the single electron S_z operator, eqn (4), with $M_S = \pm1/2$ quantum numbers, respectively, and $S = 1/2$ in eqn (3).

For OLED applications it is important to stress that the triplet state consists of three spin-sublevels, eqn (5), and that the S state is a single one, eqn (6). Thus, the statistical ratio for the triplet and singlet excitons induced by the applied voltage is 3 : 1. One should mention that the simple configurations with spin-arrows in Fig. 2 cannot represent proper spin states, eqn (5) and (6), with zero spin projection, $M_S = 0$. In accordance with the Pauli principle all states, eqn (1)–(6), are antisymmetrical with respect to coordinate permutation of two electrons; the S and T states differ in such symmetry for the spatial and spin parts. The electric dipole moment operator for the two electrons $M = er_1 + er_2$ is symmetrical with respect to their permutation. Thus the electric dipole transition moment between triplet and singlet states is equal to zero because of integration by both the spatial and spin parts (for example for the $T_1 \rightarrow S_0$ transition). Such double prohibition leads to a rather strict selection rule. Any perturbation which depends on electrostatic interaction (the most important one in chemistry) cannot overcome this double prohibition for S–T transitions. In the absence of an external magnetic field the only possible perturbation which can overcome the S–T selection rule is spin–orbit coupling (SOC). Its analysis (chapter 4) indicates that SOC is very weak for the first row elements and depends on spatial properties of the wave functions, eqn (2). When electrons and holes are localized at the neighboring molecules (Fig. 2d and e) they have overlapping HOMO wave functions with close-lying energy levels. This leads to a high probability of an electron "jump" from the right to the left molecule, or to an electron–hole recombination (Fig. 2). Vibrations of the nuclear core contribute also to the probability for such an electron "jump". Here we need to consider in some detail the relative energy and radiative properties of the S and T states which are generated inside one molecule after the electron–hole recombination.

When the recombination occurs for the singlet electron–hole pair the excited singlet state (S_1) of one molecule is formed and fluorescence emission is produced by the $S_1 \rightarrow S_0$ spin-allowed transition (Fig. 2). Accounting for the wave function for the ground singlet state:

$$\Psi(S_0) = {}^1\Phi_{i,i}{}^1\Omega = \phi_i(1)\phi_i(2)(1/\sqrt{2})[\alpha(1)\beta(2) - \beta(1)\alpha(2)], \tag{7}$$

one can derive the $S_1 \rightarrow S_0$ transition dipole moment as

$$M^{\gamma}_{1,0} = \langle S_1|\hat{M}_{\gamma}|S_0\rangle = \sqrt{2}e\langle\phi_i|r^{\gamma}|\phi_u\rangle = \sqrt{2}m^{\gamma}_{i-u}, \tag{8}$$

where $\gamma \in \{x,y,z\}$ are Cartesian projections. The single-electron integral m^{γ}_{i-u} depends on the properties of ϕ_i and ϕ_u MOs and on their ability to be concentrated in the same parts of the space. If the HOMO and LUMO are delocalized simultaneously in far separated moieties of the polymer stretched along the γ axis, the $S_1 \rightarrow S_0$ transition dipole moment, eqn (8), will be large and proportional to this separation. This is an actual situation for many conjugated organic polymers.

The rate constant for spontaneous emission $n \rightarrow m$ (k_r) and radiative lifetime (τ_r) can be determined by eqn (9):[4]

$$k_r = \frac{1}{\tau_r} = \frac{64\pi^4(\Delta E_{n-m})^3}{3h^4c^3}|M_{n-m}|^2, \quad (9)$$

where ΔE_{n-m} is the transition energy, M_{n-m} is the transition dipole moment, which is equal for fluorescence. For fluorescence

$$|M_{n-m}|^2 = M_{1,0}{}^2 = \sum_{\gamma} \langle S_1|\hat{M}_{\gamma}|S_0\rangle^2 \quad (10)$$

A typical τ_r value is of the order of nanoseconds for fluorescence of the π-conjugated organic chromophore.

Usually the first excited triplet state (T_1) is lower in energy than the singlet counterpart (S_1). This is a molecular analogue of the atomic Hund's rule.[15a] In the HOMO–LUMO approach, eqn (2), the singlet–triplet splitting is equal to

$$\Delta E_{S-T} = E(S_1) - E(T_1) = 2K_{i,u}, \quad (11)$$

where

$$K_{i,u} = \iint \phi_i(1)\phi_u(1)\frac{e^2}{r_{1,2}}\phi_i(2)\phi_u(2)\mathrm{d}v_1\mathrm{d}v_2 \quad (12)$$

is the exchange integral.[15a] It can be easily estimated for a simple typical example. For the ππ* excited state in the planar ethylene molecule within the zero differential overlap approximation

$$\phi_i = \sqrt{1/2}(\varphi_1 + \varphi_2) \quad \phi_u = \sqrt{1/2}(\varphi_1 - \varphi_2), \quad (13)$$

where φ_1 is the $2p_z$ atomic orbital (AO) at the first carbon atom, one can get

$$K_{i,u} = \tfrac{1}{2}[(11|11) - (11|22)] \quad (14)$$

$$(11|22) = \iint \varphi_1(1)\varphi_1(1)\frac{e^2}{r_{1,2}}\varphi_2(2)\varphi_2(2)\mathrm{d}v_1\,\mathrm{d}v_2 \quad (15)$$

Eqn (15) presents an example of a Coloumb repulsion integral between two electrons at two atoms. The intra-atomic repulsion integral (11|11) analogue can be estimated from spectral data for the carbon atom. Accounting (11|11) = 10.98 eV and (11|22) = 7.22 eV by semiempirical estimations, one can get $K_{i,u}$ = 1.88 eV. The energy gap between S and T vertically excited ππ* states in planar ethylene is quite big (3.76 eV) in agreement with observations.[4] This is a typical result for ππ* excitations in planar hydrocarbons.[3] In ethylene molecule the ππ* excitation is strongly localized on the C=C bond, therefore the exchange interaction is relatively high; it goes down upon delocalization and reaches an order of about 1 eV for many π-conjugated chromophores. As follows from the above simple example, the exchange interactions, eqn (14), are weaker than the Coloumb forces, eqn (15); both have the same electrostatic nature, but the former have numerous important consequences for the OLED operation.

The $S_1 \rightarrow S_0$ (π–π*) transition dipole moment, eqn (8), for the planar ethylene molecule with the HOMO–LUMO wave functions, determined by eqn (13), is equal to $m^{z}_{i-u} = \frac{1}{2}eR_{C=C}$, where z is the C=C axis. For longer polyene chains the HOMO–LUMO π–π* transition dipole moment is also proportional to the chain length and is characterized by the chain direction z-polarization. In fact, for polymers of the PPV type the excitations are polarons (polaron excitons) which are delocalized on a few units of the chain.[16–26] The transition dipole moment, eqn (8), is large (about 10 Debye); therefore light absorption and fluorescence of such polymers is quite intense. Thus, in Fig. 2e the situation with electron–hole recombination is oversimplified for conjugated organic polymers, but is more reliable for molecular crystals, nanoparticles, glasses and other molecular materials bound by van-der-Waals forces. It can be applied also for non-conjugated organic polymers. In contrast to singlets, emission from the triplet state of organic chromophores has a very low rate constant (because of strong spin prohibition for T–S transitions) and cannot compete with non-radiative quenching at room temperature. By statistical reasoning there are three triplet e–h pairs and only one singlet counterpart for each four electron–hole collisions. In the volume of such material (close to the central part of the layer) a huge part of the charge carriers – about 75% of all electron–hole pairs – recombine to produce triplet exited states which cannot emit light. At ambient temperature they are quenched by intramolecular vibrations and by phonons; thus 75% of the applied electric power are spent for heating of the device. This leads to the assumption that the emission quantum yield has an upper statistical limit of 25% in a pure organic polymeric LED.[31,32] In order to compel the triplet excitons to emit light (to compete with non-radiative deactivation at room temperature) and to do useful work in OLEDs it is necessary to incorporate special organometallic dyes into the organic polymers, containing heavy transition metals, which will participate in the charge carrier recombination and provide a strong SOC in order to overcome spin-prohibition of the $T_1 \rightarrow S_0$ transition. Therefore, the problem of SOC-induced mixing of the triplet and singlet states is a crucial one for efficient OLED devices.

Fig. 2 provides an additional oversimplification since it does not account explicitly for the driving force of charge injection and transport – the applied bias; it concentrates attention on the spatial organization of molecules in the material (polymer chain), spin behavior and direction of charge migration. This process is induced by the applied voltage and the simple scheme (Fig. 2) should be modified as is shown in Fig. 3, which accounts for more energetic details including the dependence of the MO levels on the bias.

A single layer OLED is shown in Fig. 3 with an applied bias voltage V and a vacuum energy level W_{vac}. Cathode and anode materials are characterized by their Fermi levels W_F and work functions φ. It is known that the bias provides a lowering of all MOs levels of the molecules close to the anode and increases

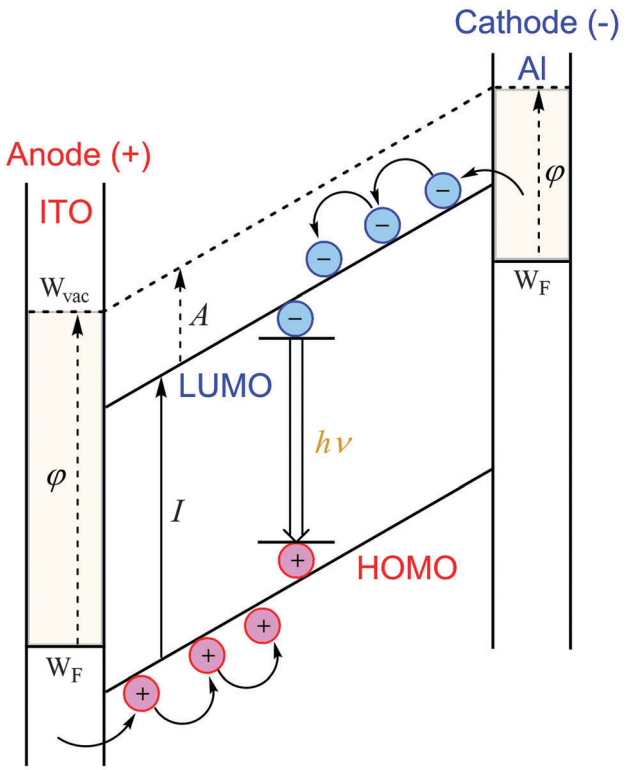

Fig. 3 Position of MO levels in OLED depending on the applied bias.

the energy of all MO levels for the molecules at the cathode junction (Fig. 3). These can be easily checked by self-consistent field (SCF) simulations. For example, SCF calculations of the benzene molecule at a distance of 3.6 Å from a positive proton charge (anode model) provides a down shift of about 4.5 eV for all MO energy levels; for a similar benzene complex with the H^- anion all MO levels are shifted up by 3.7 eV. Various modifications of the charged anode and cathode materials by metal and halogen ions (and by their clusters), respectively, do not change the qualitative results for the "up-and-down" shifts of the MO energy levels. The electronic polarization and MO energy shifts depend on the donor–acceptor properties of the organic species. Such microscopic simulation of the applied bias by the charged ions corresponds to a high voltage; at the same time it simulates coordination bonding of the adjacent organic species to the electrode surface. Quantum mechanics/molecular mechanics QM/MM calculations[27] of these models with long PPV chains (n = 5) have demonstrated the importance of intermolecular vibrations in the charge injection process. Calculations of the metal–molecular junction within the many-body Green's function framework could reproduce successfully the observed conductance switching behavior.[27] The latter is induced by conformation changes of the intercalated oligomers in the junction. It was revealed in that study that the bonds between the terminal oligomer atom and the Pd electrodes are quite weak.[27] Modern OLEDs already meet many requirements for practical applications in portable electronics (for example, in mobile phones or digital cameras) and large area displays, however, a continuous effort to improve charge carrier injection, light emission and morphology changes to suppress various quenching processes, is still in progress.[27,28]

Since the triplet states are generated in a great excess and therefore are very important for OLEDs we need to consider their properties in more detail. If the triplet electron–hole pair recombines, as is shown in Fig. 2d, the lowest triplet excited state (T_1) of the molecule is produced, which can emit spontaneous radiation in the form of a $T_1 \rightarrow S_0$ spin-forbidden transition under special conditions, which are determined mostly (or even entirely) by SOC.

Photoluminescence of organic molecules and dyes exhibits behind the fast fluorescence ($S_1 \rightarrow S_0$ transition) a delayed emission of a rather long lifetime. It can be of two types: emission of the same wavelength like the $S_1 \rightarrow S_0$ transition (delayed fluorescence), and a new-type afterglow shifted to the red side of the photoluminescence spectrum. Both types of emissions occur during seconds. The latter phenomenon was observed in viscous and frozen solid solvents of organic molecules at low temperature and has, since the 1890s, been called phosphorescence.[3,4] Half of a century proceeded with numerous discussions[3,4] before the first true interpretation of the phosphorescence phenomenon appeared. It was assigned to the $T_1 \rightarrow S_0$ spin-forbidden transition by the Russian academician A. N. Terenin in 1943 for the first time.[29] In spite of very convincing proof,[29] this interpretation was not generally accepted until the sixties when the first EPR measurements recognized definitely the paramagnetic properties of the triplet state.[4] Terenin established the triplet state nature in a very clear way by analysis of various examples of phosphorescent emissions with a reference to the first calculation of benzene spectra by Goeppert-Mayer and Sklar, where the triplet $^3B_{1u}$ and $^3B_{2u}$ states were predicted naturally by configuration interaction (CI) calculations for excitations between degenerate molecular orbitals of the e_{1g} and e_{2u} types[30] in the D_{6h} symmetry group of the benzene molecule.[30] Terenin had generalized these results for all known luminescence spectra of a large series of conjugated molecules and dyes and proposed the so-called modified Jablonsky diagram, where the role of the metastable state had been ascribed to the lowest T_1 triplet excited state. Fig. 4 represents

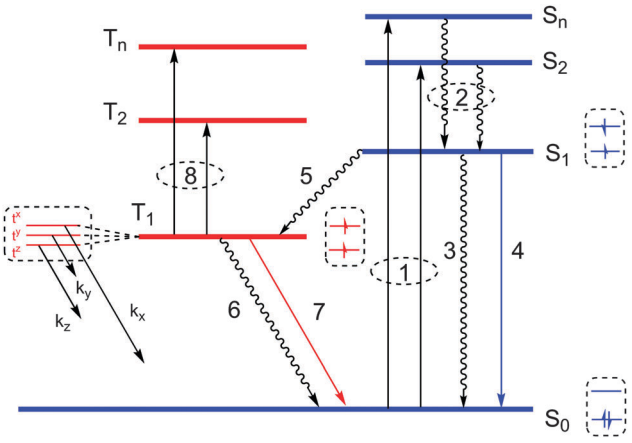

Fig. 4 The modified Jablonsky diagram.

these ideas in the form of the modified Jablonsky diagram and illustrates the main photoprocesses following light absorption (1) by organic molecules. A fast internal conversion (2) takes place after absorption of the incident light and excitation of the molecule into excited singlet states S_n. This thermal relaxation of an electronically and vibrationally excited molecule is quite rapid through transfer of excess energy from the solute molecule to the solvent. It occurs also in the gas phase because the intramolecular electron–vibrational interaction is generally found to be the main driving force. This process occurs in 10^{-13} s.[4]

When the molecule relaxes into the lowest singlet excited state S_1, the further non-radiative transition into the ground S_0 state (3) is hindered by a large energy gap and cannot compete with the fast $S_1 \rightarrow S_0$ emission (fluorescence, 4). The typical radiative fluorescence lifetime ($\tau_f = k_4^{-1}$) is on the order of 1–100 ns for organic dyes.[4] The radiationless process (3) is called internal conversion, that is when molecules in the S_1 excited singlet state may return to the ground state without emission of a photon and convert all the excitation energy into heat. It is an inefficient process in aromatic hydrocarbons and polymers, which are used in OLEDs.

In terms of the HOMO–LUMO approach, the T_1 state is lower in energy than the S_1 counterpart by the double exchange integral $2K_{i,u}$, eqn (13). This energy gap is not big (comparable with few vibrational quanta) and the non-radiative $S_1 \rightsquigarrow T_1$ transition (intersystem crossing, ISC, k_5) provides an effective electronic energy conversion into nuclear movement. The SOC between the S_1 and T_1 state is enhanced by nuclear vibrations, which generally play a crucial role in the ISC process (one can remember that spin prohibition for ISC is not very severe). The singlet–triplet processes in organic molecules are generally less probable than the singlet–singlet processes by a factor of 10^6. Accounting that radiationless vibrational processes (such as internal conversion between excited states) occur in approximately 10^{-13} s, the time required for a spin-forbidden vibrational relaxation process would be approximately 10^{-7} s, which is of the same order of magnitude as the reciprocal lifetime of an excited singlet S_1 state. Thus the ISC rate (k_5) can be, in principle, competitive with the fluorescence rate (k_4). In such a case the T_1 state can be populated with relatively high quantum yield.

The further fate of the triplet excited molecule is determined by the fact that the non-radiative $T_1 \rightsquigarrow S_0$ transition (6) strongly depends on temperature and aggregate conditions. The intrinsic spontaneous $T_1 \rightarrow S_0$ radiative rate constant (k_7^r) in π-conjugated organic molecules, being a factor of 10^6 smaller than the k_4 rate, could be expected in the range 10–10^3 s^{-1}, which thus corresponds to a phosphorescence lifetime ($\tau_p = 1/k_7$) of a fraction of a second. At ambient temperature in liquid solution a molecule experiences millions of collisions with the solvent species during this lifetime and is definitely quenched by the effective collisional deactivation before emission can occur. In molecular crystals and in polymers the triplet exciton can migrate through the lattice core and encounter other T excitons because of their long lifetime. Upon collision of two triplet molecules singlet, triplet and quintet ($S = 2$ in eqn (3)) states are possible. Statistically, for nine collisions we have one singlet, three triplets and five quintet states ($M_S = \pm 2, \pm 1, 0$ in eqn (4)). The singlet state of the collision complex with the energy $2E(T_1)$, which is usually higher than the $E(S_1)$ energy of one molecule (Fig. 4), can easily relax to the first excited singlet state S_1 and then produce a delayed fluorescence with a lifetime equal to $\tau_p/2$:[3,4]

$$^1(T_1 + T_1) = S_1 + S_0;\ S_1 = S_0 + h\nu. \quad (16)$$

The process described above is referred to as P-type delayed fluorescence and is one of the processes which is important in OLEDs because of the large concentration of triplet states generated in the emissive layer at high voltage. In the case of a low $\Delta E(S_1 - T_1)$ energy gap the thermally activated reversed ISC (5) process is possible which leads to delayed fluorescence of the E-type.[3] It is found recently to be important in a new type of highly efficient OLED.[28]

In photoluminescence of organic solvents the delayed fluorescence of the P-type is a common phenomenon at high concentrations.[3] In frozen and viscous solvents, where collisions are suppressed, the non-radiative quenching rate k_6 is also suppressed and spin-forbidden phosphorescence (intrinsic spontaneous $T_1 \rightarrow S_0$ radiation, 7, in Fig. 4) can be observed with its long natural lifetime ($\tau_p = 1/k_7$). In this explanation of all known photoluminescence phenomena Terenin employed for the first time the important notion of electron spin for phosphorescence and spin statistics (spin-allowed character) for the delayed fluorescence of the P-type.[29] Besides the first phosphorescent assignment there are other important findings about the role of the triplet states in organic photochemistry (including the role of molecular oxygen in the triplet state quenching).[29] Tribute to these discoveries[4,29] should be certainly made when discussing the modern OLED development, since triplet states and the phosphorescence phenomenon are extremely important for all types of electroluminescence – they are especially important for the modern generation of OLED devices based on implementation of metallo-organic complexes.[9,31–35] It is worth mentioning that A. N. Terenin was probably the first who studied photoconductivity of organic dyes in the solid state[36] and sensitized phosphorescence in organic solutions at low temperature, which led to the discovery of energy transfer between triplet states.[37]

From this brief historical note we return back to the role of singlet and triplet states created by charge carrier recombination, Fig. 2, and the luminance efficiency of OLEDs. For all OLED applications the energy of the triplet T_1 state is of great importance since it is this state that is mostly populated during electron–hole recombination. The rate of intersystem crossing (k_5) in most conjugated organic molecules and polymers is apparently rather low with some exceptions like fullerenes and anthracenes. Deuteration of organic molecules often suppresses the k_5 and k_6 rate constants; the C–H vibrational frequency is much higher than that of the C–D bond vibration and higher overtones should be excited in the deuterated species in order to accept the excess energy $E(T_1) - E(S_0)$ and

transfer it into vibrational relaxation. From this example one can realize that the nonradiative energy transfer is determined by electron–vibrational (vibronic) interaction to a large extent.[34,44] This notion can also be applied to the electron–hole injection, migration and recombination processes.[9a,44c] We will analyze vibronic and other corresponding problems of organic electroluminescence starting with popular OLED materials like π-conjugated polymers.

2.2. The nature of excitons in π-conjugated polymers and in organic crystals

Most polymers employed in organic photovoltaic cells and in the first efficient OLEDs[26] have π-conjugated backbones. Since we have started our review with such OLEDs[12] some more comments about PPV and similar polymers, like polyfluoren (PF) and polythiophene (PT), are necessary. We need here to analyze more the nature of the lowest excited S_1 and T_1 states in the conjugated polymer of the PPV type, since it rules the former OLED emission.[12,26] In the case of PPV this problem has been extensively discussed in the literature with supporters of the idea that the S_1 state defines the true band gap as when electron and hole is separated,[19] and those who consider the S_1 state as an exciton with tightly bound electrons being additionally stabilized by Coulomb attraction (the order of this stabilization energy was debated).[26] In fact, an exciton is a bound state of an electron and a hole, which are attracted to each other by the electrostatic Coulomb force with a particular contribution of exchange interaction depending on their spatial distribution and ranging from as little as 0.01 eV up to as large as 0.2 eV.[22]

In spite of some deviations from planarity, the π-conjugated backbones still exist and embrace almost the whole polymer. It was shown for a number of polyfluorene (PF)[20–24] and PPV oligomers[26] that some additional planarization occurs in the excited state across a long region. The binding energy can be quite small and the exciton size much larger than a molecule. This is because of the screening of the Coulomb force by other electrons in the semiconductor, determined by its dielectric constant, ε. One can introduce the critical radius R_C for the mutual interaction inside the electron–hole pair, which is defined as the distance at which the Coulomb attraction is equal to the thermal energy, $kT = \frac{e^2}{4\pi\varepsilon\varepsilon_0 R_C}$, where ε_0 represents the dielectric constant of vacuum.[9] In materials with a small dielectric constant, the Coulomb interaction between an electron and a hole may be strong and the capture radius R_C can embrace a long chain. From the above equation one obtains for a typical organic polymer, with $\varepsilon = 3$ at room temperature, a big critical radius value of about $R_C = 19$ nm. At this separation the Coulomb interaction binds the charge carriers together and they are no longer able to escape one another by thermal diffusion. In comparison to inorganic semiconductors, like silicon ($\varepsilon = 11.68$), this attraction is much stronger, enabling instantaneous exciton formation. Starting from this distance, the evolution of the electron–hole pair is determined by its own dynamics and by internal Coulomb and exchange interactions being slightly different for the S and T pairs. The time evolution leads to formation of a stable exciton which involves 3–5 molecular blocks in the conjugated polymer.[20] The triplet states are more localized than singlets. In materials with small molecules (and in non-conjugated polymers) the excitons tend to be small, of the same order as the size of the unit cell (one monomeric unit in the polymer chain). Molecular excitons may even be entirely located on the same molecule, as it is shown in Fig. 2.

For PPV and similar materials it was shown that the optical absorption and emission spectra of the polymer and oligomers present clear manifestations of strong vibronic effects.[12,22–26] From analysis of the vibronic progressions in few oligomers the relaxation energy in the long chains has been estimated to be of the order of 0.15–0.2 eV.[26] Just the presence of the vibronic progressions in such polymers show that the electronic excitation produces a localized geometry relaxation across the exciton. Semiempirical AM1/CI calculations of the five-ring PPV oligomer indicate that the distortion region can extend over 20 Å;[23] of course such electronic excitation cannot be related to a pure band gap transition.[26] This value represents a lower limit for the delocalization length of the electronic wave function of the exciton. A detailed analysis of the PPV oligomers wave functions suggests that most of the delocalization takes place over 5 monomer units (approximately 30 Å).[23] Similar results have been obtained for other polymers of the polyfluorene type by TD DFT calculations.[20,21]

Vibrational effects in molecular optical spectra are usually considered within the Born–Oppenheimer adiabatic approximation: the total wave function is presented as a product of electronic, eqn (1), and nuclear (χ) wave functions. The former one is an eigenfunction of the adiabatic Hamiltonian: $H(e,Q)\Psi_n(e,Q) = E_n(Q)\Psi_n(e,Q)$ were e and Q represent all electronic and nuclear coordinates and $\Psi(e,Q)$ is solved by the Schrödinger equation at a particular nuclear configuration Q with fixed atomic positions. There are $3N - 6$ vibrational coordinates for a molecule with N atoms and the same number of normal modes Q_i. The potential energy surface (PES) $E_n(Q)$ has a particular global minimum $E_n(Q_0)$ at the equilibrium molecular structure for each quantum state Ψ_n. For the excited S and T states these minima are usually shifted from the ground state equilibrium with a particular displacement d_i along each normal mode. In the harmonic approximation the nuclear wave functions are presented by Hermit polynomials for each mode $\chi_v(Q_i)$ and the total nuclear wave function is presented by their product. The vibrational energy $\varepsilon_v = h\nu(v + 1/2)$ has to be added to the $E_n(Q_0)$ value. The Hessian matrix $(\partial^2 E/\partial Q_i \partial Q_j)_0$ can be diagonalized and with account of the reduced masses (μ_i) it determines vibrational frequencies ν_i and normal modes.

The vibronic progressions in molecular spectra can be calculated in terms of the linear coupling model (LCM). It assumes that the excited-state normal modes are identical to those of the ground state, apart from a displacement d_i from the equilibrium for i-th vibrational mode, which is estimated by the excited-state energy gradients $(\partial E_n/\partial Q_i)_0$ computed at the

equilibrium geometry Q_0 of the ground singlet state.[18] The electronic transition dipole moment, eqn (8), depends, in general, on the nuclear coordinates Q. This dependence will be taken into account in Section 4 in terms of Herzberg–Teller theory. The LCM procedure is able to give a reasonable description of the low-resolution spectra which are available for PPV and other polymers. At this stage we use the Condon approximation which assumes that the electronic transition dipole moment M is independent on the nuclear coordinates.

A number of theoretical[20–23,26] and experimental studies[16,17,24,25] have been carried out in order to investigate the chain length dependence of the energies of the singlet S_1 and triplet (T_1 and T_n) excited states of a homologous series of conjugated fluorene oligomers, and similar systems. In all these polymers the primary photoexcitations have been found to be singlet excitons. The excitons decay either radiatively in the form of fluorescence emission or by nonradiative quenching.

For *p*-phenylene vinylene and many other π-conjugated organic molecules this radiation is characterized by a relatively large electric-dipole transition moment (EDTM) $\langle S_1|\hat{M}_\gamma|S_0\rangle$, determined in eqn (8); here $\hat{M}_\gamma = e\sum_i \gamma_i$ is the electric-dipole moment operator, $\gamma \in \{x,y,z\}$ and summation include coordinates of all electrons. With account of nuclear coordinates one can write the EDTM for a particular vibronic v–v' band of the i-th vibrational mode in the form:

$$\left|M_{S_1,S_0}\right|^2 = \sum_\gamma \left|\left\langle \chi_i^{v1}\Psi_1\middle|M_\gamma\middle|^1\Psi_0\chi_i^{v}\right\rangle\right|^2 = \sum_\gamma \left|M_{1,0}^\gamma\right|^2 \left|\left\langle \chi_i^{v} \mid \chi_i^{v'}\right\rangle\right|^2 \quad (17)$$

where $\left|\left\langle \chi_i^{v} \mid \chi_i^{v'}\right\rangle\right|^2$ is a Franck–Condon (FC) factor. The FC factor of the 0–0 transition can be calculated analytically while the other FC factors can be computed through the recursion relationship proposed by Doktorov *et al.*[18b] For a given vibrational mode Q_i, the dimensionless electron–vibration coupling strength called the Huang–Rhys parameter enters the FC factor determination $S_i = \frac{\omega_i d_i^2}{2\hbar}$, where $\omega_i = 2\pi\nu_i$ and d_i is a displacement.[18c] From electroluminescence of PPV it was expected that the delocalization of the exciton in longer chains has to be accompanied by a slight redistribution in the amplitude of the lattice relaxations taking place in the central part of the oligomer accompanied by appearance of weak geometry distortions in the additional PPV units. Thus it was shown that the relaxation energy continuously evolves as a function of the chain-length.[23] Similar relaxation evolves the Huang–Rhys factors for the active vibrational modes. The displacements from equilibrium structure (d_i) on going from the S_0 ground state to the lowest excited S_1 state reduce successively along the series of increasing oligomer units in the polymer chain. The Huang–Rhys factor is proportional to $(d_i)^2$ and should thus decrease with the chain length. In the experimental luminescence spectra of PPV and of some substituted oligomers the intensity of the 0–0 transition is found to be higher in the longer chain.[23,24] This means that the Huang–Rhys factor for the active modes, which determines the vibronic progression of photoluminescence really gets smaller with the prolongation of the oligomer.

A number of studies of the chain-length evolution of the calculated vertical transition energies both by semiempirical INDO/S type[22,23] and by TD DFT/B3LYP levels[20,21] have been published associated with the absorption and emission processes. Both processes are primarily described by an electronic transition between the HOMO and LUMO levels, as in most conjugated systems. However, the relative weight of the additional electronically excited configurations contributing to the description of the lowest excited state increases as the chain grows.[9,17,18a,23] In general, configuration interaction studies provide the electronic wave function which includes the local excitations inside one block of the polymer, as well as charge-transfer contributions: $\Psi = c_1\Psi(AB^*) + c_2\Psi(A^*B) + c_3\Psi(A^-B^+) + c_4\Psi(A^+B^-) + c_5\Psi(A^*B^*) + c_6\Psi(A^{**}B)$. Here A* indicates the excited A molecule, and A and B refer to different polymer blocks. The wave function can describe polymers with different distortion in various blocks, as well as heterogeneous materials including dopants and heterojunctions. If the ionic terms dominate (c_4, $c_3 \gg c_1$, c_2) the above wave function describes a charge-transfer exciton. The opposite example (c_4, $c_3 \ll c_1$, c_2) corresponds to exciplexes or excimers. In the latter case the expansion corresponds to the Frenkel exciton in a molecular solid if the two molecules are identical (A = B). In some cases the double excitations (c_5, c_6) have to be taken into account (triplet–triplet annihilation, long polyene chain). The bipolaron contributions, $c_7\Psi(A^-B^-) + c_8\Psi(A^+B^+)$, are important under particular conditions which violate the number of particles by electron transfer from the neighboring chains.

2.3. Luminescence polarization measurements in stretched polymers

The results of King *et al.*[17] who measured optical polarization of fluorescence, phosphorescence, and absorption in oriented polymer films in the polyfluorene homopolymer (poly-9,9-diethylhexylfluorene) are very important for analysis of the nature of the exciton wave functions. When the stretched polymer film was oriented parallel ($A^{\parallel}$) and perpendicular ($A^{\perp}$) to the polarizer the polarised S_0–S_1 absorption and fluorescence spectra show a high dichroic ratio ($A^{\parallel}/A^{\perp}$). The S_0–S_1 absorption has been successfully polarised with a dichroic ratio of approximately 10. Similarly, the fluorescence emission is even more strongly polarised showing a dichroic ratio of 20 at the maximum of the emission band. The phosphorescence in this polyfluorene homopolymer, however, has its dominant component orthogonal to the chain orientation.[28] The polarised photoinduced triplet–triplet T_1–T_n absorption shows that the higher excited triplet transitions have a dipole moment along the chain with a high dichroic ratio. Thus the T_1–T_n transition is more like a transition of singlet character, with the change in electron distribution during the transition being along the chain. However, the phosphorescence in this polyfluorene homopolymer has its dominant component

orthogonal to the chain orientation.[28] King *et al.*[17] made interesting conclusions about the nature of the exciton wave functions in polyfluorene and the peculiar behaviour of the triplet excitons with respect to the singlet ones.

There are two directions that are orthogonal to the polymer chain; these are the short axis of the molecule and the out of plane axis. As the chains are only aligned in one dimension and the polymer backbone adopts a helical structure it is not possible to differentiate between the two orientations orthogonal to the backbone. Thus, while the phosphorescence transition dipole moment has a dominant component orthogonal to the chain backbone, without alignment of the polymer in two dimensions, it is difficult to predict accurately the precise direction of the dipole moment from experimental data. We will return to the discussion of the results of King *et al.*[17] for polyfluorene later in Section 5.

3. Phosphorescent OLEDs

3.1. Electron–hole recombination and spin statistics in OLEDs

The triplet state has three projections of the total spin and the singlet has only one microstate, eqn (5) and (6). By statistics the S and T excitons are produced in the ratio 1 : 3. The phosphorescence from the triplet excitons in organic polymers and crystals composed mostly from hydrocarbons is much less intense than the fluorescence.[3,4] The spin-allowed $S_1 \rightarrow S_0$ transition in hydrocarbons has typically a 10^6 times higher radiative rate constant than the $T_1 \rightarrow S_0$ spin-forbidden transition.[38] The phosphorescence gains the dipole activity through spin–orbit coupling (SOC) perturbation. SOC is very weak in π-conjugated hydrocarbons and typical organic polymers since the lowest T_1 and S_n states (which determine the intense UV-vis absorption) all possess ππ* spatial character.[4] The matrix elements of the orbital angular momentum between the spatial parts of ππ* states are negligible. In a way, this is one of the most important reasons for very weak phosphorescence in π-conjugated chromophores and hydrocarbons, as one can see from the theoretical treatment presented below. Thus the triplet excitons in such organic polymers cannot provide useful work in polymeric OLEDs in the form of bright light emission. Their energy is spent by de-excitation through vibrational relaxation and heating the polymer. Thus the quantum yield in such OLEDs based on organic polymers has an upper statistical limit of 25%.[22,39] For this reason, pure organic polymers have been substituted during the last decade by other materials, which are able to involve the triplet excitons in the useful game of light production.

In order to compel the triplet excitons to emit light and to do useful work in OLEDs, one needs to increase dramatically the radiative rate constant of phosphorescence in order to enhance competition with the nonradiative deactivation rate constant. The second way is to compel the triplet excitons of the organic host to share their excitation energy with other species, which are able to emit light.

3.2. Principles of electro-phosphorescence in multilayer devices

Electro-phosphorescent organic light-emitting devices (PhOLEDs) have been shown to harvest 100% of the excitons (singlet and triplet) generated by electrical injection, corresponding to a four-fold increase in efficiency compared to that achievable in singlet-harvesting fluorescent polymeric OLEDs.[32] In modern OLED devices a large number of layers are used.[10,31] Different materials may be chosen to aid charge injection at electrodes as well as improve the conductive properties. Multilayer devices with doping by cyclometalated complexes including heavy ions provide high external quantum efficiency by utilizing both the singlet and triplet excitons.[31–35]

Electro-phosphorescent organic light-emitting diodes have been shown to harvest 100% of the excitons (singlet and triplet) generated by electrical injection, corresponding to a four-fold increase in efficiency compared to that achievable in singlet-harvesting fluorescent polymeric OLEDs.[24] In modern OLED devices a large number of layers are used.[9,31] Different materials may be chosen to aid charge injection at electrodes as well as to improve the conductive properties. Multilayer devices with doping by cyclometalated complexes including heavy ions provide high external quantum efficiency by utilizing both the singlet and triplet excitons.[32]

Since the ratio of singlet and triplet excitons formed under electrical excitation is approximately 1 : 3,[22] the phosphorescent organic light-emitting diodes (PhOLEDs) based on metalloorganic phosphors can approach 100% internal quantum efficiency (in principle) because they harvest both the singlet and triplet excitons simultaneously.[31] All 75% of the generated triplet excitons can be light-emitting because of the strong SOC on the metal ion and huge enhancement of the $T_1 \rightarrow S_0$ transition probability. The singlet excitons (25%) can emit light independently or transfer their energy to the triplet through intersystem crossing (ISC). Thus the heavy-metal phosphor overcomes the limitation of 25% efficiency of the conventional polymeric fluorescent OLED and approaches 100% harvesting. However, the relatively long lifetime of metalloorganic triplet phosphors (about 1 μs) provides additional difficulties: they need to survive before emission. Thus an attempt to increase luminance by high voltage leads to new limitations in PhOLEDs.[31–33] At high current the long triplet lifetime may lead to dominant triplet–triplet annihilation (TTA) and corresponding quenching.

The general scheme of multilayer OLED devices is presented in Fig. 5. The width of each layer is variable depending on the experimental conditions and required luminescence features. Usually the anode material consists of tin-doped indium oxide (ITO) which is deposited into the transparent glass. The opposite cathode is responsible for electron generation and should be characterized by a low electron work function. Such materials include alkaline earth metals and other active metals such as aluminum. To promote efficient electron and hole injection towards the emission layer, thin inorganic materials layers are usually used. In Fig. 5 the hole-injection and electron-injection materials are made of molybdenum trioxide (MoO_3) and lithium

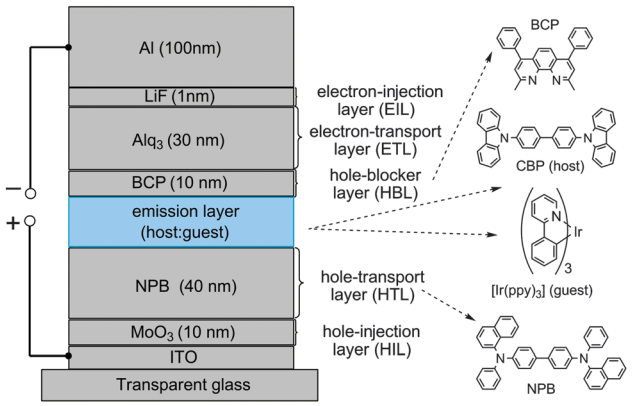

Fig. 5 Principle scheme of an OLED device.

fluoride, respectively. The diversity of OLEDs is mainly due to the different materials of electron-transfer (ETL), hole-transport (HTL) and emission (EML) layers. In general, ETL and HTL are organic materials, containing carbazole, fluorene or arylamine moieties. As can be seen from Fig. 5 the 4,4′-bis[*N*-(1-naphthyl)-*N*-phenylamino]biphenyl (NPB) is an example of the frequently used HTL material, whereas the most popular ETL material is Alq_3 which is also an effective emitter. In order to prevent the hole migration into the ETL the hole-blocker layer (HBL) of 2,9-dimethyl-4,7-diphenyl-1,10-phenanthroline (BCP) can be used.

The emission layer is the most important material of the OLED. Usually, the EML consists of two components: a host material as the solid matrix and a guest material (implemented into the host volume) as the emitter. One example of a host material is 4,4′-*N*,*N*′-dicarbazolebiphenyl (CBP), which is frequently used in OLED technologies and is presented in Fig. 5. In general, all host materials are characterized by a long phosphorescent lifetime and thus their triplet excitons (75% of total) are degraded without the desired emission. As a result, the total efficiency of such an OLED would not exceed 25%. In order to attract the triplets to the emission process, the guest phosphorescent material is commonly implemented into the host matrix. The guest material plays a key role in OLEDs and can determine the color of the device. Since the pioneering attempt of Baldo *et al.*,[32] showing that transition metal complexes with organic ligands doped into organic host matrices provide a great improvement of the OLED efficiency, various phosphorescent organometallic compounds (phosphors) have been studied to optimize the color tuning and luminous efficiency.[31–35] The most popular phosphors are cyclometallated iridium complexes, in particular, the compound of Ir(III) cation with phenylpyridinate (ppy) anions: the $Ir(ppy)_3$ complex is shown in Fig. 5. It is important to stress, that the concentration of the guest material is much lower in comparison with host matrix and thus the emitter cannot capture independently the excitons. Therefore, in order to compel the emitter to start work, an efficient energy transfer from the host to the guest molecules should be carried out.

The microseconds scale of lifetime at high currents may also cause long-ranged triplet exciton diffusion (about 10 nm and more) that could become quenched in the adjacent layers of other materials in the device. Therefore, the metalloorganic phosphors have to be widely dispersed in the host matrix to reduce these competitive factors.[40,41] In Fig. 6 two possible mechanisms of non-radiative energy transfer in the emissive layer of OLED are shown. The host material is presented by excited molecule D* which is generated by electron–hole recombination and considered as an energy donor.

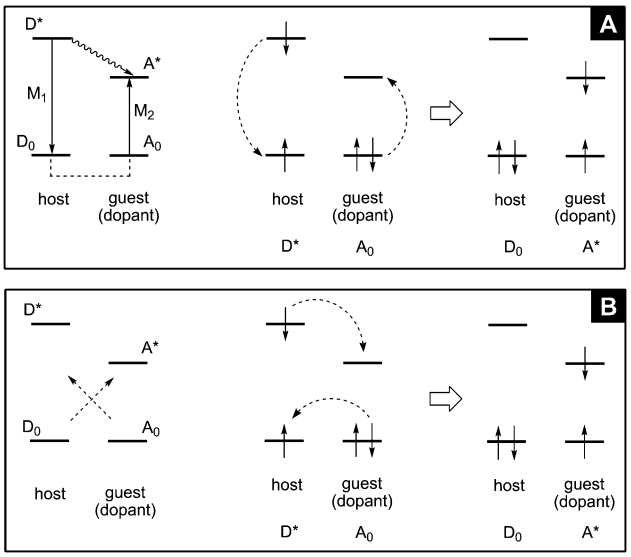

Fig. 6 Transfer processes in host material doped with emissive dye.

The host material layer is doped with the light-emissive molecules (guest) in small concentrations, which are potential acceptors of energy (A). The long-range Förster energy transfer of the singlet excitons (D*) generated on the host matrix to the guest is indicated in Fig. 6A by a wavy arrow: $D^*A_0 \rightsquigarrow D_0A^*$. For the Förster transfer a significant overlap of the emission spectrum of the matrix and the absorption spectrum of the dopant is a crucial parameter. The driving force of the Förster energy transfer mechanism is a dipole–dipole interaction between the dipole transition moments M_1 and M_2 (Fig. 6A). Schematically this can be shown by simultaneous electron "jumps" in HOMO–LUMO configurations (dashed arrows in the middle of Fig. 6A). Information about the transition dipole moments in host and guest molecules is necessary for understanding the fundamentals of the energy transfer processes. Thus, polarization measurements in stretched polymer hosts[17] are very important for energy transfer analysis (Section 5). Nuclear vibrations and vibronic coupling are additional attributes for any type of energy transfer.

The second type of energy transfer is the short-range mechanism of Dexter (Fig. 6B). Its driving force is the exchange interaction expressed by the exchange integral. In the oversimplified scheme (the middle of Fig. 6B) the exchange integral is a measure of the electron exchange rate between the HOMO and LUMO of the donor and acceptor, shown by dashed arrows. Such an heuristic interpretation of the exchange mechanism is quite popular but is not rigorous.

The exchange integral strongly depends on the overlap of donor and acceptor orbitals; this determines the short-range

action of the Dexter energy transfer. The Dexter mechanism can be applied to spin-forbidden transitions, where the Förster energy transfer cannot occur. It determines the T–T energy transfer, triplet–triplet annihilation and other spin-dependent processes.[42–60] The exchange integral is also important for the third type of transfer in OLEDs: the direct generation of S and T excitons on the guest compound, when electrons and holes migrate through the host material. (In such cases the host matrix works solely as a charge-transporting material.) For direct carrier trapping on the phosphorescent guest dopant a significant overlap and offset of the HOMO and LUMO energies of the host and guest molecules is necessary. This is realized for the $Ir(ppy)_3$ dopant in the CBP host matrix (Fig. 5). For several OLED schemes employing cyclometallated iridium complexes, like that shown in Fig. 5, the hole is trapped first.[35] Then the electron is attracted and the process of exciton formation proceeds *via* charge transfer (CT) states, as proposed by Yersin.[34] The process involves the organometallic triplet state emitter and the immediate environment consisting of organic molecules of the host matrix. Since the triplet state of the phosphor emitter has a large CT character the direct exciton formation is enhanced for organometallic complexes.[60a] One should note that OLEDs are more efficient if the charge carriers are trapped on the phosphorescent emitter. In the very common case when the Förster energy transfer is operating (for the singlet–singlet energy transfer between host and guest molecules) a significant power loss occurs because of the host S_1 state population process (the S_1 state energy of the host is larger than that of the guest, and the energy transfer inevitably leads to some part of electronic energy degradation into heat).

In efficient PhOLEDs, where organometallic phosphors are typically used as emitting guests dispersed in a host matrix to avoid TTA or other quenching processes associated with the relatively long τ_p, the choice of the proper host material is a significant challenge for chemists.[13,56] They need to synthesize the matrix, which matches the host and guest triplet states energy – the T level of the host needs to be larger than the phosphorescent dopant T level to prevent undesired back transfer, frontier orbital levels must permit fast charge injection from HTL and ETL and morphological and chemical stability must be maintained. In addition, a good overlap between the emission band of the host and the absorption spectrum of the guest are necessary for Förster-type energy transfer. Various carbazole and fluorine derivatives, small molecules as well as polymers, are especially suitable for the above requirements.[13,16,20,24]

Together with new efficient dopants these hosts have provided great progress in OLED device development during the last two decades, from the hardly visible strip in the dark with a very short operational life (of a few seconds) to extremely bright devices[31] (up to 10^7 Cd m^{-2}) that can work for years at a brightness of typically 10^3 Cd m^{-2}.

A popular device design for highly efficient OLEDs is based on multiple layers deposited by thermal evaporation of small molecules.[31] The simultaneous or successive evaporation of the volatile compounds can afford a high quality optimization of the OLED architecture.[56] A great advantage of the multilayer structure is that each layer can be optimized for its sole purpose (or for a combination of targets); it can be light emission or charge injection and transport. In addition, the quenching mechanisms can be reduced by choice of a suitable charge or exciton blocking interlayer.

It is much more difficult to realize the multilayer structures when one solely uses soluble materials. A rather attractive approach is to use thermally induced or light-induced cross-linking of hole-transporting–electron-blocking layers on a suitable anode material.[56] Hole conducting triarylamine-based materials have been used as a graded hole-injection layer to build highly efficient blue OLEDs.[56b] An alternative approach to the cross-linking is to insolubilize a thin layer of an appropriate semiconducting polymer on a conducting polymer anode such as PEDOT:PSS, or poly(3,4-ethylenedioxythiophene) poly(styrenesulfonate).[56c] This, so-called interlayer approach proposed by Kim *et al.*,[56b] has become increasingly popular in organic photovoltaic and OLED fabrication.[9a]

3.3. Efficiency parameters of white OLEDs

The power efficiency of OLEDs is equal to the ratio of the luminous power going out of the device (as detected by the eye) to the applied electric power. The responsivity of the human eye varies greatly across the visible spectrum. Therefore, a specific unit called the lumen (lm) is introduced to quantify the perceived luminous intensity. The response of the human eye to bright visible light, known as the photopic response ($P(\lambda)$), has a peak maximum of luminous efficiency per incident optical watt of 683 lm W^{-1} at a wavelength of 555 nm (the photopic response in the red and blue regions is much weaker). The eye responsivity Φ is determined by the integral $\Phi = \frac{\int \phi(\lambda) P(\lambda) \mathrm{d}\lambda}{\int \phi(\lambda) \mathrm{d}\lambda}$, where $\varphi(\lambda)$ is an arbitrary spectrum function. To determine the power efficiency of OLED devices the following successive equations series can be used: $\eta_Q = \frac{N_{out}^{photons}}{N_{in}^{electrons}}$, $L = \Phi \frac{hc}{\lambda} \eta_Q \frac{I}{e}$, $\eta_P = \frac{L}{VI} = \Phi \eta_Q \frac{V_\lambda}{V}$, where η_Q is the external quantum efficiency, L – the luminous flux, h – Planck's constant, c – speed of light, I – current, e – electron charge, VI – electrical power, V_λ/V – electrical efficiency, η_P– power efficiency.

Another way to determine the quantum efficiency η_Q is the following equation: $\eta_Q = \chi \eta_X \eta_C \phi_{PL}$, where χ is the fraction of emissive excitons, η_X – the output coupling fraction, η_C – charge balance fraction, ϕ_{PL} – photoluminescence efficiency of the emissive material. Among all parameters, the most important technical characteristics of OLED devices are the photopic response Φ, quantum efficiency η_Q and the electrical efficiency V_λ/V, which define the power efficiency of OLEDs.

In this contest a special attention should be paid to lighting, which accounts for 22% of the electricity consumption in buildings in the US, with a large contribution from inefficient incandescent lamps.[54] Therefore it is easy to understand the great interest in white OLED development owing to their potential for large improvement of efficiency over incandescent lamps combined with low-cost and high manufacturability.

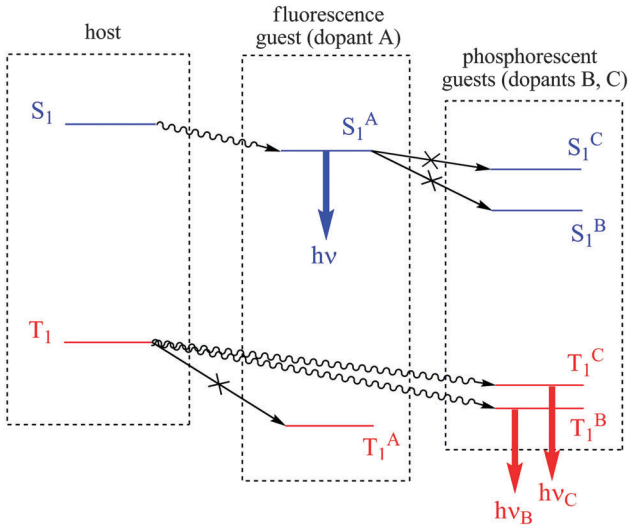

Fig. 7 Energy transfer mechanism in the emissive layer of the combined fluo-phos WOLED.

White OLEDs (WOLEDs) using phosphor dopants, which have the potential for 100% internal quantum efficiency, need to satisfy many special requirements for device architecture.[54–56] The first most efficient WOLEDs have been fabricated using all colors produced by phosphorescent dopants. These devices suffer from the common bottlenecks of requiring strongly increased operating voltages and remaining chemical non-stability. Sun *et al.*[54] first introduced a special device concept that implements a blue fluorescent dopant in combination with green and red phosphorescence from spatially separated guests (Fig. 7). Such WOLED devices yield a stable color balance and high power efficiency while still maintaining the potential for 100% internal quantum efficiency. They exploit the advantages of strong blue fluorescence of organic chromophores (dopant A, Fig. 7) to harness all electrically generated S_1 excitons of the host, and strong emission from two phosphorescent dopants to harvest all triplet excitons. This minimizes exchange energy losses.

Those WOLEDs which use phosphorescent blue dopants excited from the conductive host material introduce a high exchange energy loss $2K_{i,u}$, eqn (13), in power efficiency (this is about 0.8 eV for typical hosts). This results from the energy relaxation following ISC. Such WOLEDs with blue phosphorescence exhibit a short operational life because of photochemical destruction under high exciton energy.

The extended emissive layer of the WOLED shown in Fig. 7 consists of three dopants inside the single host, CBP,[54] similar to EML, presented in Fig. 5. In contrast to Fig. 5, besides the [Ir(ppy)$_3$] green phosphor, there are two additional dopants spatially separated in the host matrix. The EML is sandwiched between the electron-transporting–hole-blocking layer of BCP, and the hole-transporting level of NBP. The device operation mechanism (Fig. 7) is based on the two different types of energy transfer principles involved. The S and T excitons are formed in the host matrix with an approximate 1 : 3 ratio upon bias. The S excitons are transferred by the resonant Förster mechanism into the blue dopant–fluorophor (carbazol-vinylene derivative, CzVD), which has a low concentration (5%). The CzVD (dopant A, Fig. 7) emits strong blue fluorescence since the ISC is suppressed in this molecule. The triplet states of the dopant A are not populated by T–T energy transfer from the host owing to the low doping concentration and short-range operation of the Dexter energy transfer mechanism. In contrast, the triplet states typically have long diffusion paths (about 100 nm in the CBP host) and can migrate into that part of the emissive layer where the phosphor dopants B and C are situated. (C is the green [Ir(ppy)$_3$] phosphor and B is the red Ir(III) bis(2-phenylquinolyl)acetylacetonate phosphor.) They are doped in a separate part of the host matrix, far from the A molecules. The host triplets in the region of the B and C phosphor location provide an efficient T–T energy transfer by the Dexter mechanism, thus green and red phosphorescence occurs. Placing an undoped host spacer of a thickness lager than the Förster effective radius (about 5–10 nm) between the A and B, C layers prevents singlet–singlet energy transfer from the blue fluorophore to the S_1 states of the B and C phosphors.[54] Such construction of the WOLED device allows the S and T excitons to be harvested along completely independent channels of energy transfer from host to guests; each can be separately optimized for the resonant conditions. Thus the energy losses can be minimized supporting an internal quantum efficiency close to 100%. The two channels within one device allow transfer of all the triplet host energy to the phosphor dopants, providing the singlet host energy exclusively to the blue fluorophore dopant. Sun *et al.*[54] have obtained an external quantum efficiency of 18.7% and a power efficiency of 37.6 lm W^{-1} with such a WOLED device architecture.

However, the scheme shown in Fig. 7 used by Sun *et al.*[54] employs the carbazol-vinylene fluorescent emitter, the triplet level of which lies below the triplet levels of the green and red phosphors. Thus the blue fluorophore dopant still remains a potential triplet exciton trap in this device.[55] In order to avoid exciton losses in the triplet manifold, special fluorophore emitters have recently been proposed with small S–T gaps.[55a]

From the above short discussion of WOLEDs illustrating some recent trends in organic electroluminescent technology we must turn back to the general principles which determine the internal and external quantum efficiency of light emission.

4. Spin–orbit coupling effects in OLEDs

In order to understand the important peculiarities and manifestations of spin–orbit coupling in molecules we need to consider first the SOC effects in atoms. The manifestation of SOC in atomic spectra in the form of the multiplet splitting are much more prominent than in polyatomic molecules.

4.1. Spin–orbit coupling in atoms

Simple analysis of the SOC-induced splitting in atomic spectra led to idea of the electron spin quantization, eqn (3) and (4). In atoms the orbital angular momentum $\hat{\mathbf{L}}^2\Psi = L(L+1)\hbar^2\Psi$ is observable and quantized, where the quantum numbers $L = 0, 1,$

and 2 determine the S, P, and D type of states. Together with the total electron spin of the atom, eqn (3), one needs to consider the total angular momentum $\vec{\mathbf{J}}^2\Psi = J(J+1)\hbar^2\Psi$, where the total angular momentum operator is $\vec{\mathbf{J}} = \mathbf{L} + \vec{\mathbf{S}}$. In relativistic theory all atomic states with $L \neq 0$ acquire additional corrections to the total energy, which are equal to the expectation values of the SOC operator.[15] In this way the famous splitting of atomic terms with different J occurs. Calculation of this fine structure can be easily illustrated by an example of the one-electron hydrogen-like atom. The SOC operator for the hydrogen-like atom with a nuclear charge Z was obtained for the first time by Dirac:[4]

$$H_{so} = \frac{e^2\hbar^2}{2m^2c^2}\frac{Z}{r^3}\vec{l}\vec{s} \tag{18}$$

The vector operators $\vec{\mathbf{l}}$ and $\vec{\mathbf{s}}$ are the single electron orbital and spin angular momentum operators, respectively (which are given here in $\hbar$ units). The scalar product of these operators can easily be calculated by the definition $\vec{\mathbf{J}}^2 = (\vec{\mathbf{L}} + \vec{\mathbf{S}})^2 = \vec{\mathbf{L}}^2 + 2\vec{\mathbf{L}}\vec{\mathbf{S}} + \vec{\mathbf{S}}^2$, which can be applied to the single electron example and to many-electron cases as well:

$$\vec{\mathbf{L}}\vec{\mathbf{S}} = \tfrac{1}{2}[J(J+1) - L(L+1) - S(S+1)] \tag{19}$$

For the excited ^{2}P states ($L = 1$, $S = 1/2$) of the hydrogen-like atom one gets two possible spin-sublevels with the quantum numbers $J = 1/2$ and $J = 3/2$. In relativistic theory these sublevels acquire the following energy corrections as expectation values of the SOC operator, eqn (18):

$$\begin{aligned} E(^2\mathrm{P}_J) &= \langle H_{SO}\rangle = \frac{e^2\hbar^2}{2m^2c^2}\left\langle\frac{Z}{r^3}\right\rangle_{np}\left\langle\vec{\mathbf{ls}}\right\rangle_{np} \\ &= \zeta_{np}\frac{1}{2}[J(J+1) - L(L+1) - S(S+1)] \end{aligned} \tag{20}$$

where

$$\zeta_{np} = \frac{e^2\hbar^2}{2m^2c^2}\left\langle\frac{Z}{r^3}\right\rangle_{np} \tag{21}$$

is a SOC constant for the given np state. It is useful to calculate the SOC energy corrections for the doublet split sublevels $^2\mathrm{P}_J$, which are equal to:

$$\begin{aligned} E\left(^2P_{\frac{1}{2}}\right) &= \langle H_{SO}\rangle = \frac{e^2\hbar^2}{2m^2c^2}\left\langle\frac{Z}{r^3}\right\rangle_{np}\left\langle\vec{\mathbf{ls}}\right\rangle_{np} \\ &= \zeta_{np}\frac{1}{2}\left[\frac{1}{2}\left(\frac{1}{2}+1\right) - 1(1+1) - \frac{1}{2}\left(\frac{1}{2}+1\right)\right] = -\zeta_{np} \end{aligned} \tag{22}$$

$$\begin{aligned} E\left(^2P_{\frac{3}{2}}\right) &= \langle H_{SO}\rangle = \frac{e^2\hbar^2}{2m^2c^2}\left\langle\frac{Z}{r^3}\right\rangle_{np}\left\langle\vec{\mathbf{ls}}\right\rangle_{np} \\ &= \zeta_{np}\frac{1}{2}\left[\frac{3}{2}\left(\frac{3}{2}+1\right) - 1(1+1) - \frac{1}{2}\left(\frac{1}{2}+1\right)\right] = \frac{1}{2}\zeta_{np} \end{aligned} \tag{23}$$

One has to stress that the spin sublevel splitting in atoms by J is non-equidistant, and that it follows the Lande interval rule $E(J) - E(J-1) = \lambda J$.

The radial integral for the hydrogen-like atom is equal to:[4]

$$\left\langle\frac{1}{r^3}\right\rangle_{nl} = \frac{Z^3}{n^3(l+1)(l+1/2)a_0{}^3}, \tag{24}$$

where a_0 is the Bohr radius. For the lowest state of the Balmer series ($n = 2$) the radial SOC integral, eqn (21),

$$\zeta_{2p} = \frac{e^2\hbar^2}{2m^2c^2}\left\langle\frac{Z}{r^3}\right\rangle_{2p} = \frac{e^2\hbar^2}{2m^2c^2}\frac{Z^4}{24a_0{}^3} \tag{25}$$

can be easily calculated to be equal to 1.5×10^{-5} eV = 0.24 cm^{-1}. According to eqn (22) and (23) the spin multiplet splitting in the Balmer series of the hydrogen atom can be estimated as $E(^2\mathrm{P}_{3/2}) - E(^2\mathrm{P}_{1/2}) = (3/2)\zeta_{2p} = 0.36$ cm^{-1}. This splitting is exactly equal to the experimental value, which is well-known from the old years of atomic spectroscopy.[4] One can see that the SOC splitting of atomic terms strongly depends on nuclear charge Z. For example, for the He^+, Li^{2+} and Be^{3+} hydrogen-like ions the corresponding ζ_{2p} values, calculated by eqn (25) are equal to 3.84, 19.4 and 61.4 cm^{-1}, respectively.

Similar expressions, eqn (20) and (21), determine the fine structure of the valence np-shell of the many-electron atoms. A simple generalization of the SOC operator in this case can be summarized in the forms:[38]

$$H_{SO} = \zeta\sum_i \vec{l}_i\vec{s}_i = \lambda\vec{L}\vec{S} \tag{26}$$

where

$$\lambda = \pm\frac{\zeta}{2S} \tag{27}$$

The sign "plus" in eqn (27) corresponds to the open shell, which is "less-than-half" occupied, "minus" – to the "more-than-half" occupied open shell. Eqn (19) and (21) are still valid, but Z is a semiempirical parameter, since in many-electron atoms the spin–other orbit coupling (two-electron part of SOC operator) occurs. It enters with a negative sign and produces a screening effect in the effective SOC integral, eqn (21). Thus the effective nuclear charge Z in eqn (21) is much lower than the atomic number; for example $Z_C = 3.6$, $Z_N = 3.9$, $Z_O = 4.55$.[53c]

Eqn (27) is a theoretical background for the third Hund's rule.[15a] In general the Hund's rules determine the relative energy of atomic states with a degenerate open shell which is not fully occupied. For example, for the ^{3}P term ($L = 1$, $S = 1$) with the SOC operator, eqn (26) and (19), one can get the following atomic term splitting: $E(^3\mathrm{P}_2) - E(^3\mathrm{P}_1) = 2\lambda$ and $E(^3\mathrm{P}_1) - E(^3\mathrm{P}_0) = \lambda$. For the carbon atom in the ^{3}P ground state with the $(1s)^2(2s)^2(2p)^2$ open shell, eqn (27) provides $\lambda = \zeta/2$ ("less-than-half" occupied 2p-shell), and the observed energy levels of $J = 0$, 1 and 2 are equal to 0, 15 and 45 cm^{-1}, respectively,[15b] which corresponds approximately to $\zeta_{2p}(C) = 30$ cm^{-1}. For the oxygen atom the ground state is also ^{3}P, but with the $(1s)^2(2s)^2(2p)^4$ open shell which is "more-than-half" occupied; in this case eqn (27) provides $\lambda = -\zeta/2$ and the atomic spectrum exhibits the inverted order of the observed energy levels with $J = 2$ being the lowest one. Its energy is taken as an origin, and the $J = 2$, 1 and 0 levels show the energy 0, 76 and 228 cm^{-1}, respectively.[15b]

This corresponds to $\zeta_{2p}(O) = 153\ cm^{-1}$. The ground state of the nitrogen atom $^4S_{3/2}$ has the exactly half-occupied open shell $(1s)^2(2s)^2(2p)^3$ with $L = 0$, thus its SOC splitting is absent.[15b] The value of the SOC integral can be determined by interpolation in the observed splitting of a series of nitrogen ions: $\zeta_{2p}(N) = 73\ cm^{-1}$.[15a] Using these semiempirical constants one can calculate SOC in organic molecules.

Deviations from the Lande interval rule are determined by the same factors which are responsible for the zero-field splitting (ZFS) in organic molecules; these are spin–spin coupling and the second order SOC effects in perturbation theory.[38] The latter contribution is quite large in heavy atoms, like Ir and Pt; thus estimations of the SOC constant ζ_{5d} for their valence shell from the atomic spectral splitting are rather questionable.[9] Theoretical calculations provide $\zeta_{5d}(Ir) = 4430\ cm^{-1}$, $\zeta_{5d}(Os) = 3351\ cm^{-1}$ and $\zeta_{5d}(Pt) = 4860\ cm^{-1}$ for 5d elements[15c] important in OLED technology. One can see that the strength of the SOC perturbation in these atoms is comparable with atomic exchange integrals of the (dd′|dd′) type,[15d] which determine the relative energy of multiplets with different L and S quantum numbers in the case of the Russell–Saunders (RS) scheme, or L–S coupling.[15a] The well-known hierarchy of Hund's rules is based on the framework of this scheme.

Besides the above-considered third Hund's rule, based on eqn (26) and (27), there are two others which also have connections with the principles of OLEDs. Let us illustrate these by comparison of the carbon and iridium atoms. The first Hund rule states that the lowest state has the highest possible multiplicity (^3P for carbon). The second Hund rule determines the relative energy of states of the same multiplicity (the state with the maximum L quantum number is more stable: ^1D is lower than ^1S for carbon). All these states are connected with the same electronic configuration of the open shell with two electrons on three degenerate 2p-AOs. The energy splitting between ^3P, ^1D and ^1S states is determined by atomic exchange integral $2K_{pp'}$,

$$K_{pp'} = (pp'|pp') = \tfrac{1}{2}[(pp|pp) - (pp|p'p')], \qquad (28)$$

where p and p′ denote two degenerate 2p-AOs and notations similar to eqn (12) and (15) are used. Thus the first Hund rule in atoms has a direct molecular analogy for excited S and T states.

4.2. Heavy elements

The Ir(III) ion has $(5d)^6$ configuration: thus its ground state is a quintet ^5D which is split in five sublevels. According to the third Hund's rule the lowest one is $^5D_4$ since the open shell $(5d)^6$ is "more-than-half" occupied and the "minus" sign is used in eqn (27). The energy level with the maximum $J = 4$ value provides the SOC energy correction 4λ and the next levels with $J = 3$ has zero SOC contribution by eqn (19). From this equation the levels with $J = 2$, 1 and 0 have positive SOC corrections -3λ, -5λ and -6λ, respectively. Here $\lambda = -\zeta_{5d}(Ir)/4 = -1107.5\ cm^{-1}$, eqn (27). This theoretical splitting, derived from eqn (19), does not reproduce well the observed spectrum.[15c] The above RS scheme neglects SOC-induced mixing between different multiplets with the same J values. This mixing can be large for the $^5D_1$ and $^3P_1$ states, for example, and provides large deviations from the RS scheme, since both states are close in energy. The Ir(III) ion is a rather difficult example of the SOC treatment in atoms.[53c,d]

At the first glance the Hund's rules have nothing in common with OLED theory, since the orbital angular momentum is quenched in polyatomic molecules. But the iridium ion in the cyclometalated Ir(III) complexes (Fig. 9) is almost equally perturbed by SOC and by Coulomb interactions, including perturbations by the ligands.[60,61] Thus it still maintains some "atomic" peculiarities of its valence shell in the field of the ligands, though the atomic Ir orbitals are slightly split and mixed with the ligands MOs in non-relativistic DFT calculations. It is difficult to assign the analogues of the $^5D_1$ and $^3P_1$ states of the iridium $(5d)^6$ open shell, since the ground state of all cyclometalated Ir(III) complexes (Fig. 9) is the singlet state S_0 closed shell. Nevertheless, the SOC constant extracted from the atomic spectra or calculated for the separated atom can be used for the perturbation theory treatment of various homoleptic and heteroleptic iridium complexes. In the ECP basis set the same type of AOs, Coulomb and exchange integrals describe the potential of the valence shell and the choice of atomic $\zeta_{5d}(Ir)$ parameter is still reasonable. The expected values of the $\vec{L}$ operator and the SOC corrections are equal to zero in the Ir(III) complexes (Fig. 9), but the nondiagonal integrals of $\vec{L}$ and of the SOC operators are still large, almost as in the separated Ir(III) ion.[61] These nondiagonal terms are similar to those between $^5D_1$ and $^3P_1$ states of the individual ion. This ligand admixture would diminish the SOC matrix elements in the complexes, but the remaining one-center Ir(III) contributions will be correctly estimated. In this respect the connection of all three Hund's rules with the S–T spin mixing in the emissive layers of OLEDs becomes obvious. This concerns also light atoms. Not only the Z value, but also the orbital structure of the S and T excited states, eqn (2), is important. In a way this is similar to the importance of all quantum numbers in the atomic analogues, eqn (20). We shall come back to the Hund's rule analogy later on when the nature of the excited states in cyclometalated Ir(III) complexes will be discussed in more detail.

It is interesting to compare and analyze the light iron atom with the similar ground state $^5D_4$ $(3d^64s^2)$ configuration, which obeys the RS scheme, since the observed spectrum reproduces the Lande interval rule: $E(^5D_4) = 0$, $E(^5D_3) = 416$, $E(^5D_2) = 704$, $E(^5D_1) = 888$, $E(^5D_0) = 978\ cm^{-1}$. An average interval $\lambda = -96\ cm^{-1}$ corresponds to the Lande interval rule (the largest deviation corresponds to the highest value $J = 4$). The SOC constant for the 3d shell of the iron atom obtained from eqn (27) is equal to $\zeta_{3d}(Fe) = 384\ cm^{-1}$.

In the neutral Ir atom the ground state 1^4F $(5d)^7(6s)^2$ splitting is more complicated because of the non-diagonal SOC mixing with the excited configuration 2^4F $(5d)^8(6s)^1$. In the SOC calculations of iridium complexes in ref. 53*cd* an effective core potential (ECP) and basis set for the Ir atom was used, augmented with a set of the 6f polarization functions.

The valence orbitals of this ECP are already adjusted for relativistic contractions and expansions, but the 5d AO are nodeless (even though they should have two inner nodes).

4.3. Spin–orbit coupling in molecules

Instead of the full Breit–Pauli operator[53b] one can use for the cyclometalated iridium complexes (CIC) and Pt compounds an effective one-electron SOC operator with effective nuclear charge for each atom A.[53c,d]

$$H_{\mathrm{SO}} = \frac{e^2\hbar^2}{2m^2c^2}\sum_i \sum_{\mathrm{A}} \frac{Z_{\mathrm{eff}}(\mathrm{A})}{r_{i\mathrm{A}}{}^3}\vec{\mathbf{l}}_i^{\mathrm{A}}\vec{\mathbf{s}}_i \tag{29}$$

This operator was widely used for SOC calculations in molecules and charge-transfer complexes with semiempirical self-consistent field (SCF) configuration interaction (CI) methods[47,48] and also in *ab initio* approaches.[53c,d] For the ECP basis set in heavy elements the effective nuclear charge in eqn (29) looses its physical meaning and becomes a rather large fitted parameter, since the 5d AOs are nodeless. Koseki *et al.* have obtained $Z_{\mathrm{eff}}(\mathrm{Ir}) = 1150.38$, $Z_{\mathrm{eff}}(\mathrm{Pt}) = 1176.24$. For the first row transition metals and for the lighter elements these parameters have the usual meaning.

In the following we concentrate our attention on the SOC matrix elements for the spin-mixing calculations in molecules. To do this we need to rewrite the SOC operator, eqn (29), in the form:

$$\begin{aligned} H_{\mathrm{SO}} &= \sum_i \vec{\mathbf{B}}_i\vec{\mathbf{s}}_i = \sum_i \left(B_i^x s_i^x + B_i^y s_i^y + B_i^z s_i^z\right) \\ &= H_{\mathrm{SO}}^x + H_{\mathrm{SO}}^y + H_{\mathrm{SO}}^z \end{aligned} \tag{30}$$

where

$$\vec{\mathbf{B}}_i = \sum_{\mathrm{A}} \zeta_{\mathrm{A}}\vec{\mathbf{l}}_i^{\mathrm{A}} \tag{31}$$

In a simple two-electron approach, eqn (1)–(7), the excited state molecular wave functions are well described by the single-electron excitations, eqn (2)–(4). In this case only two electrons have to be accounted in the SOC operator, eqn (30). In this case the SOC operator can be presented in the form:

$$H_{\mathrm{SO}} = \vec{\mathbf{B}}_1\vec{\mathbf{s}}_1 + \vec{\mathbf{B}}_2\vec{\mathbf{s}}_2 = \frac{1}{2}\left(\vec{\mathbf{B}}_1 + \vec{\mathbf{B}}_2\right)(\vec{\mathbf{s}}_1 + \vec{\mathbf{s}}_2) + \frac{1}{2}\left(\vec{\mathbf{B}}_1 - \vec{\mathbf{B}}_2\right)(\vec{\mathbf{s}}_1 - \vec{\mathbf{s}}_2) \tag{32}$$

Thus, the SOC operator is divided into products of the spatial and spin parts. The first product $\frac{1}{2}\left(\vec{\mathbf{B}}_1 + \vec{\mathbf{B}}_2\right)(\vec{\mathbf{s}}_1 + \vec{\mathbf{s}}_2)$ includes both symmetrical parts with respect to electron permutation. The spatial part will operate on the spatial wave functions, eqn (2). Therefore, it can mix two different triplet states, the spatial parts of which, ${}^3\Phi_{i\text{–}u}$ and ${}^3\Phi_{i\text{–}v}$, have the same permutation symmetry and differ in occupation of the two MOs, ϕ_u and ϕ_v, being empty orbitals in the ground S_0 state.[4] The spin part $(\vec{\mathbf{s}}_1 + \vec{\mathbf{s}}_2)$ can mix the triplet spin state wave functions, eqn (5), all being symmetrical with respect to electron permutation.

An account of the permutation symmetry is also important in the analysis of the second product in eqn (32):

$$\frac{1}{2}\left(\vec{\mathbf{B}}_1 - \vec{\mathbf{B}}_2\right)(\vec{\mathbf{s}}_1 - \vec{\mathbf{s}}_2) \tag{33}$$

where both terms are antisymmetrical. Thus, this part of the SOC operator can mix singlet and triplet states. For example, the ground state, eqn (7), and the triplet state, eqn (34), can be mixed since in both expressions the spatial and spin wave functions possess the opposite permutation symmetry.

$$\begin{aligned} \Psi(\mathrm{T}_1) &= {}^3\Phi_{i,u}{}^3\Omega_{|1,0\rangle} \\ &= \frac{1}{\sqrt{2}}[\phi_i(1)\phi_u(2) - \phi_i(2)\phi_u(1)]\frac{1}{\sqrt{2}}[\alpha(1)\beta(2) + \beta(1)\alpha(2)], \end{aligned} \tag{34}$$

Only a particular part of the SOC operator, eqn (33), is able to provide interaction between such different singlet and triplet states which are doubly orthogonal by the spatial and spin parts integration. Now the SOC matrix element $\langle \mathrm{T}_1|H_{\mathrm{SO}}|\mathrm{S}_0\rangle$ can be divided into two parts: the spatial part:

$$\begin{aligned} &(1/2\sqrt{2})\langle[\phi_i(1)\phi_u(2) - \phi_i(2)\phi_u(1)]|\left(\vec{\mathbf{B}}_1 - \vec{\mathbf{B}}_2\right)|\phi_i(1)\phi_i(2)\rangle \\ &\quad = -(1/2\sqrt{2})\langle\phi_u|\vec{B}|\phi_i\rangle = -\vec{B}_{u,i}/\sqrt{2} \end{aligned} \tag{35}$$

and the spin part:

$$(1/2)\langle[\alpha(1)\beta(2) + \beta(1)\alpha(2)]|(\vec{\mathbf{s}}_1 + \vec{\mathbf{s}}_2)|[\alpha(1)\beta(2) - \beta(1)\alpha(2)]\rangle = 1 \tag{36}$$

The single-electron spatial integral $\langle\phi_u(1)|\vec{\mathbf{B}}_1|\phi_i(1)\rangle = \langle\phi_u(2)|\vec{\mathbf{B}}_2|\phi_i(2)\rangle = \vec{\mathbf{B}}_{u,i}$ can be easily calculated as a sum of contributions from different atoms, eqn (31). It has three Cartesian components each transforming in the molecular point group as a rotation around an axis. In the minimal basis set the ϕ_i molecular orbital expansion in an organic compound can be written as a sum of atomic contributions:

$$\phi_i = \sum_{\mathrm{A}} \left(C_{i,s}^{\mathrm{A}}\varphi_s^{\mathrm{A}} + C_{i,x}^{\mathrm{A}}\varphi_{p_x}^{\mathrm{A}} + C_{i,y}^{\mathrm{A}}\varphi_{p_y}^{\mathrm{A}} + C_{i,z}^{\mathrm{A}}\varphi_{p_z}^{\mathrm{A}}\right) \tag{37}$$

The orbital angular momentum operator in Cartesian and spherical coordinates has the form:

$$\begin{aligned} l_x &= -i\hbar\left(y\frac{\partial}{\partial z} - z\frac{\partial}{\partial y}\right) = -i\hbar\left(\sin\varphi\frac{\partial}{\partial\theta} - ctg\,\theta\cos\varphi\frac{\partial}{\partial\varphi}\right) \\ l_y &= -i\hbar\left(z\frac{\partial}{\partial x} - x\frac{\partial}{\partial z}\right) = -i\hbar\left(\cos\varphi\frac{\partial}{\partial\theta} - ctg\,\theta\sin\varphi\frac{\partial}{\partial\varphi}\right) \\ l_z &= -i\hbar\left(x\frac{\partial}{\partial y} - y\frac{\partial}{\partial x}\right) = -i\hbar\frac{\partial}{\partial\varphi} \end{aligned} \tag{38}$$

It produces rotation of atomic orbitals on each atom A; accounting that $\vec{\mathbf{l}}^{\mathrm{A}}$ in eqn (31) is given in atomic units ($\hbar = 1$) one gets ($\vec{\mathbf{l}}^{\mathrm{A}}\varphi_s^{\mathrm{A}} = 0$, $l_x^{\mathrm{A}}\ \varphi_{p_x}^{\mathrm{A}}$):

$$\begin{aligned} &l_x^{\mathrm{A}}\phi_{p_y}^{\mathrm{A}} = i\phi_{p_z}^{\mathrm{A}},\ l_x^{\mathrm{A}}\phi_{p_z}^{\mathrm{A}} = -i\phi_{p_x}^{\mathrm{A}};\ l_y^{\mathrm{A}}\phi_{p_z}^{\mathrm{A}} = i\phi_{p_x}^{\mathrm{A}}, \\ &l_y^{\mathrm{A}}\phi_{p_x}^{\mathrm{A}} = -i\phi_{p_z}^{\mathrm{A}}; l_z^{\mathrm{A}}\phi_{p_x}^{\mathrm{A}} = i\phi_{p_y}^{\mathrm{A}},\ l_z^{\mathrm{A}}\phi_{p_y}^{\mathrm{A}} = -i\phi_{p_x}^{\mathrm{A}} \end{aligned} \tag{39}$$

The wave functions of the atomic orbitals are given elsewhere.[14] With account of the typical MO expansions, eqn (37), and results of the $\vec{\mathbf{l}}^{\mathrm{A}}$ operator action, eqn (39), the spatial integral $\vec{\mathbf{B}}_{u,i}$ for organic molecules can be calculated:

$$B^x_{u,i} = i\sum_{\mathrm{A}} \zeta_{\mathrm{A}}\left(C^{\mathrm{A}}_{u,z}C^{\mathrm{A}}_{i,y} - C^{\mathrm{A}}_{u,y}C^{\mathrm{A}}_{i,z}\right),$$
$$B^y_{u,i} = i\sum_{\mathrm{A}} \zeta_{\mathrm{A}}\left(C^{\mathrm{A}}_{u,x}C^{\mathrm{A}}_{i,z} - C^{\mathrm{A}}_{u,z}C^{\mathrm{A}}_{i,x}\right), \quad (40)$$
$$B^z_{u,i} = i\sum_{\mathrm{A}} \zeta_{\mathrm{A}}\left(C^{\mathrm{A}}_{u,y}C^{\mathrm{A}}_{i,x} - C^{\mathrm{A}}_{u,x}C^{\mathrm{A}}_{i,y}\right).$$

If the lowest T_1 state has a $\pi\pi^*$ character, like in the planar ethylene example, eqn (13), all spatial component of the SOC integral $\langle T_1|H_{SO}|S_0\rangle$, eqn (40), are equal to zero since only the $2p_z$ AO enters the π-MO expansions. After analysis of the spatial part, eqn (35), we have to consider the spin part, eqn (36), of the SOC matrix element. First, we need to specify components of the single-electron $\vec{\mathbf{s}}$ spin operator:[14]

$$s_x = \frac{\hbar}{2}\begin{pmatrix}0 & 1\\ 1 & 0\end{pmatrix}, \quad s_y = \frac{i\hbar}{2}\begin{pmatrix}0 & 1\\ -1 & 0\end{pmatrix}, \quad s_z = \frac{\hbar}{2}\begin{pmatrix}1 & 0\\ 0 & -1\end{pmatrix}, \quad (41)$$

where spin functions $\alpha = \begin{pmatrix}1\\0\end{pmatrix}, \beta = \begin{pmatrix}0\\1\end{pmatrix}$ are eigen-functions of the s_z operator, eqn (4), with $m_S = \pm\frac{\hbar}{2}$. Indeed, multiplication of two matrices proves the results: $s_z\alpha = \frac{\hbar}{2}\alpha$ and $s_z\beta = -\frac{\hbar}{2}\beta$. In this way one can get: $s_x\alpha = \frac{\hbar}{2}\beta$, $s_x\beta = \frac{\hbar}{2}\alpha$, and $s_y\alpha = -\frac{i\hbar}{2}\beta$, $s_y\beta = \frac{i\hbar}{2}\alpha$. Calculations of the two-electron integral, eqn (36), includes separate integration for each electron, accounting for orthogonality conditions of the type $\langle\alpha(1)\beta(1)\rangle = 0$. Now one can see that in eqn (36) only the z-component of the spin operator $(\vec{\mathbf{s}}_1 - \vec{\mathbf{s}}_2)$ provides the result. This can be summarized in the form that the starting integral $\langle T_1|H_{SO}|S_0\rangle$, which is the product of the spatial and spin parts, eqn (35) and (36), has to include only the z component of the SOC operator, eqn (30): $H^z_{SO} = \sum_i B^z_i s^z_i$ and only the z-component of the triplet spin function T^z_1 with zero projection of the total spin on z-axis, eqn (5). We need to construct two combinations of two other spin functions in eqn (5) in order to satisfy similar requirements for x and y axes, since there is no preferential direction in the molecular frame. They are presented in eqn (42)

$$|T^x\rangle = (1/\sqrt{2})[|1,-1\rangle - |1,1\rangle]; \quad |T^y\rangle = (i/\sqrt{2})[|1,-1\rangle + |1,1\rangle];$$
$$|T^z\rangle = |1,0\rangle, \quad (42)$$

being eigen-functions of the irreducible $\hat{T}_{2q}$ polarization operator.[42] Each $|T^\alpha\rangle$ function corresponds to the zero projection of the total spin on the α axis. In symmetrical molecules (C_{2v}, D_{2h} and higher point groups) these $\alpha = x, y, z$ axes coincide with internal molecular symmetry axes.[38] In the absence of an external magnetic field only weak internal magnetic interactions are important for the spin-projection quantization in molecular OLED materials. These are the dipole–dipole electronic spin–spin coupling (SSC) and SOC, which determine the zero-field splitting (ZFS) of the triplet state.[4] The internal magnetic interactions are connected with the molecular frame and obey the selection rules of the symmetry point group of the molecule. Diagonalization of the ZFS tensor determines its own axes, which usually coincide with molecular axes in the C_{2v}, D_{2h} and higher symmetry point groups. Thus, eqn (42) determines the eigen-functions of the ZFS tensor.[38,42] With such useful choice of the triplet spin functions, the SOC matrix elements $\langle T^\alpha_1|H_{SO}|S_0\rangle$ can be reduced to the following expressions, derived in the form:[38]

$$\langle T^x_1|H^x_{SO}|S_0\rangle = -\frac{1}{\sqrt{2}}B^x_{u,i}, \quad \langle T^y_1|H^y_{SO}|S_0\rangle = -\frac{1}{\sqrt{2}}B^y_{u,i}, \quad \langle T^z_1|H^z_{SO}|S_0\rangle = -\frac{1}{\sqrt{2}}B^z_{u,i}, \quad (43)$$

For the excited singlet states of the type $\Psi(S_n) = {}^1\Phi_{i,v}\ {}^1\Omega$ and $\Psi(S_m) = {}^1\Phi_{j,u}\ {}^1\Omega$ one can derive the following SOC integrals, respectively:

$$\langle S_n|H^\alpha_{SO}|T^\alpha_1\rangle = -\frac{1}{2}B^\alpha_{v,u}, \quad (44)$$

$$\langle S_m|H^\alpha_{SO}|T^\alpha_1\rangle = \frac{1}{2}B^\alpha_{j,i}, \quad (45)$$

where $\alpha = x,y,z$. In the single-center approximation, eqn (40), we can obtain that the SOC matrix element between singlet and triplet excited states of the $\pi\pi^*$ type is equal to zero. Since the optical spectra of the π-conjugated organic molecules in the visible region used in OLEDs are determined by $\pi\pi^*$ excited states, one cannot expect that the SOC operator, eqn (33), will remove the permutation symmetry restrictions for mixing of the S and T states. This mixing is entirely determined by the orbital structure of the S and T states. The special symmetry of the single-electron $\vec{\mathbf{B}}$ operator, eqn (31), coincides with the symmetry of the orbital angular momentum operator. Since the structure of the part of the SOC operator, eqn (33), allows the S and T state orthogonality to be overcome, owing to permutation symmetry restrictions, the orbital angular momentum operator matrix elements between various MOs are alone decisive for the SOC selection rules. These matrix elements can be obtained from eqn (40) by substitution $\zeta_{\mathrm{A}} = 1$. The degree of change of the orbital angular momentum between S and T states (when we equalize their permutation symmetry) is one of the important factors which determine the strength of their mixing by SOC. The other important factors are the values of ζ_{A}, which depend on the nuclear charge of the atoms constituting the molecule. The latter factor is often considered to be decisive in OLED applications.[24,31–35,54–55] It is known that the introduction of heavy elements usually leads to an increase of the S–T transition rates.[4] These phenomena used to be explained by SOC

enhancement and explanations are usually based on qualitative arguments connected with eqn (18) and (24). Analysis of the external heavy atom effects in phosphorescence[57] indicates the importance of scrutinizing properly the orbital angular momentum. The SOC calculations in charge-transfer complexes also depend on small π–σ deformations and changes in orbital angular momentum.[48] The weight of the element itself cannot explain all peculiarities of S–T mixing of excitons, their transport and electron–hole recombination rates. In the following we will see that all these properties depend crucially on the charge-transfer admixture coefficients and orbital angular momentum deformations during the electrophysical processes which accompany charge currents and light emission in OLEDs.

4.4. Perturbation theory

Let us consider the singlet (S_n) and triplet (T_1) excited states to be solutions of the non-relativistic Schrödinger equation in the adiabatic approximation, eqn (17), with eigenvalues $E(S_n)$ and $E(T_1)$, respectively (the nuclear coordinate dependence is omitted for a while at a fixed molecular structure). With account of SOC perturbation each particular spin-sublevel T_1^α wave function of the lowest triplet state gains some particular admixtures from the singlet states:

$$\tilde{T}_1^\alpha = T_1^\alpha + \sum_n \frac{\langle S_n|H_{SO}|T_1^\alpha\rangle}{E(T_1)-E(S_n)} S_n \qquad (46)$$

The admixture coefficient is larger the larger the SOC integral and the smaller the energy gap in the denominator. Typically these coefficients are of the order 0.001–0.1 making perturbation theory applicable. The irreducible representations of the S_n and T_1 state spatial wave functions determine the non-zero component of the active spin-sublevel T^α: their direct product should coincide with the irreducible representations of rotation around the α axis. This is actually a spatial symmetry of the SOC operator.[4] For the chosen electronic configurations of the S_n and T_1 states in eqn (44), which differ in occupation of two MOs (ϕ_v and ϕ_u), only their spatial symmetry determines the nonzero matrix element. According to eqn (40), the particular nonzero $B^\alpha_{v,u}$ integral defines the spin-sublevel T^α which is active in the triplet–singlet mixing with the S_n state. Thus, each spin-sublevel T^α is characterized by its own pattern of mixing with the singlet states, which is very important for OLED operation.[34,35]

If we shall submit now the perturbed T_1 state wave functions, eqn (46), into the $T_1^\alpha \rightarrow S_0$ transition moment expression, we get the non-zero result:

$$\left\langle \tilde{T}_1^\alpha \middle| M_\gamma \middle| S_0 \right\rangle = \sum_n \frac{\langle S_n|\hat{H}_{SO}|T_1^\alpha\rangle^*}{E(T_1)-E(S_n)} \langle S_n|M_\gamma|S_0\rangle \qquad (47)$$

In that case one can say that the $T_1^\alpha \rightarrow S_0$ transition borrows intensity from the $S_n \rightarrow S_0$ spin-allowed transitions. The electric-dipole activity of the particular spin-sublevel T_1^α and light polarization are determined by the value of the SOC matrix element in eqn (47) and by the optical activity of the corresponding S_n excited state in light absorption (or emission). The energy gap in the denominator of eqn (47) does not depend practically on the spin-sublevel, since the zero-field splitting between sublevels is almost negligible in comparison with the non-relativistic T–S gap.

In a similar manner the ground state is also perturbed by spin–orbit coupling and has some admixture of the triplet excited states.

$$\tilde{S}_0 = S_0 + \sum_\alpha^{x,y,z} \sum_n \frac{\langle T_m^\alpha|H_{SO}|S_0\rangle}{E(S_0)-E(T_m)} T_m^\alpha \qquad (48)$$

This provides additional intensity borrowing from the $T_1^\alpha \rightarrow T_m^\alpha$ transitions; the intensity of those is easily measured by the flash-photolysis technique.[4]

$$\left\langle T_1^\alpha \middle| M_\gamma \middle| \tilde{S}_0 \right\rangle = \sum_m \frac{\langle T_m^\alpha|H_{SO}|S_0\rangle}{E(S_0)-E(T_m)} \langle T_1^\alpha|M_\gamma|T_m^\alpha\rangle \qquad (49)$$

The α and γ components of the active spin-sublevels are determined by symmetry selection rules. In low symmetry point groups (without second order axes) the few spin-sublevels of the same triplet T_m state can be admixed to the ground singlet state wave function, eqn (48). But this is not important if we consider the phosphorescent activity of a particular T_1^α spin-sublevel. Accounting for both S_0 and T_1 state perturbations, eqn (46) and (48), one can get the final expression for the $T_1^\alpha \rightarrow S_0$ transition moment:

$$\left\langle \tilde{T}_1^\alpha \middle| M_\gamma \middle| \tilde{S}_0 \right\rangle = M_\gamma(T_1^\alpha) = \sum_m \frac{\langle T_m^\alpha|H_{SO}|S_0\rangle}{E(S_0)-E(T_m)} \langle T_1^\alpha|M_\gamma|T_m^\alpha\rangle + \sum_n \frac{\langle S_n|H_{SO}|T_1^\alpha\rangle^*}{E(T_1)-E(S_n)} \langle S_n|M_\gamma|S_0\rangle \qquad (50)$$

Since the SOC matrix elements are imaginary values in polyatomic molecules, eqn (40), one should care about the complex conjugation. The absolute value of the square of transition moment is the same for both directions $T_1^\alpha \rightarrow S_0$ and $S_0 \rightarrow T_1^\alpha$ at a fixed geometry.

Here the terms with $m = 1$ and $n = 0$ provide a particular contribution: accounting for $\langle T_1^\alpha|H_{SO}|S_0\rangle = \langle S_0|H_{SO}|T_1^\alpha\rangle^*$ and the different signs in the two denominators of eqn (50) this particular contribution depends on the difference of two permanent dipole moments of the triplet and singlet states. The additional term for the $T_1^\alpha \rightarrow S_0$ transition dipole moment is equal to

$$\left\langle \tilde{T}_1^\alpha \middle| \vec{M} \middle| \tilde{S}_0 \right\rangle = \frac{\langle T_1^\alpha|H_{SO}|S_0\rangle}{E(S_0)-E(T_1)} \langle T_1|\vec{M}|T_1\rangle - \langle S_0|\vec{M}|S_0\rangle \qquad (51)$$

and is important for the charge transfer (CT) triplet state phosphorescence.[38,48] The CT states usually have a much larger dipole moment than the ground singlet state. This contribution is important for many types of excitons in OLEDs and especially for elementoorganic compounds the metal-to-ligand charge transfer states. In organic CT complexes of the donor–acceptor type the SOC integral in eqn (52) always gains additional contributions because of π–σ orbital mixing.[48] This explains

the enhanced phosphorescence of such CT complexes in comparison with the emission of separate donor and acceptor molecules.[48] A simple expansion of Mulliken's theory of CT complexes[58a,b] with an account of eqn (52) provides a reliable interpretation of their luminescence properties[48] and has also applications to the electrophysics of OLED emission layers.

The oscillator strength of the $S_0 \rightarrow T_1^\beta$ absorption is proportional to the square of the absolute value of the integral $M^2_{S-T} = \sum_\beta \sum_\gamma \left| \left\langle \tilde{S}_0 \middle| M_\gamma \middle| \tilde{T}_1^\beta \right\rangle \right|^2$ and is equal to $f_{S-T} = \frac{2}{3}\Delta E M^2_{S-T}$, where M and ΔE values are in atomic units (a.u.). The radiative lifetime of a particular spin sublevel T_1^α and the rate constant of the $T_1^\alpha \rightarrow S_0$ transition (Fig. 4) can be calculated by the equation

$$k_\alpha = \frac{1}{\tau_\alpha} = \frac{64\pi^4(\Delta E_{TS})^3}{3h^4c^3} \sum_\gamma^{x,y,z} \left| M_\gamma\left(T_1^\alpha\right) \right|^2, \qquad (52)$$

where $M_\gamma(T_1^\alpha)$ is determined in eqn (50). Measurements of these emissive parameters are important in OLED applications.[34,35] The spin sublevel selectivity of phosphorescence (all k_a are different in Fig. 4) can be studied in doped crystals and solid solvents at liquid helium temperatures, when spin–lattice relaxation (SLR) is frozen.[34,38,42,60] All photoprocesses of the triplet state optical pumping (ISC) and decay are spin selective, thus the optical excitation of molecules leads to a nonequilibrium population (spin orientation) of the T_1^α sublevels, even in zero magnetic field.[42] The SLR processes are very fast at ambient temperature (even in liquid nitrogen) and thermalize spin sublevel populations to equilibrium before the phosphorescence occurs. Therefore, the averaged lifetime observed at 77 K is

$$\frac{3}{\tau_{av}} = \frac{1}{\tau_x} + \frac{1}{\tau_y} + \frac{1}{\tau_z}. \qquad (53)$$

Spin orientation of the triplet state has been detected for a number of organic doped crystals at 1–4 K by the optical detection of magnetic resonance (ODMR).[60] Yersin *et al.*[34,35] have studied spin orientation and emission decay times of the individual triplet substates of a number of phosphor dyes widely used in OLEDs by phosphorescence kinetic measurements and their temperature dependence. These studies provide detailed information on the dominating SOC contributions and S–T mixing which are extremely important for the design of OLED materials and general principles of device construction. Recent calculations have shed new light and deeper understanding of these experimental results.[60–91]

4.5. Quadratic response method

Time-dependent density functional theory (TDDFT) calculations are now widely used to understand singlet state absorption and fluorescence and how the chemical environment around the molecular complexes used in OLEDs influences its photophysical properties.[55a,69] Generally, the physicochemical and photophysical properties of the emitter in the emissive layer of OLEDs are strongly influenced by the host medium properties, such as thermal stability and photostability, excitation and emission spectra, luminescence efficiency, concentration-quenching rate constants and host–guest energy transfer rates. Phosphorescence rate calculations from first principles is a most important and difficult task for the structure–activity relationships for OLED materials. In this regard we address the quadratic response (QR) methodology[51b,53b,92–94] which is frequently used in order to elucidate spin–orbit coupling effects and the radiative lifetime in the high temperature limit for the Ir(III) and Pt(II) complexes used in PhOLEDs. It was previously demonstrated that the matrix element of eqn (50) is associated with the residue of a quadratic response function:

$$\lim_{\omega \rightarrow \omega_1} (\omega - \omega_1) \left\langle \left\langle x^l; H^k_{SO}; C \right\rangle \right\rangle_{0,\omega}, \qquad (54)$$

where ω and ω_1 are the frequencies of the transition, x^l is the l-th component of the dipole operator, H^k_{SO} is the k-th component of the spin–orbit operator, C is an arbitrary triplet operator.[53] The response function (54) corresponding to the transition moment of eqn (50) can be concretized as follows (Einstein summation convention):

$$\begin{aligned} &\lim_{\omega \rightarrow \omega_1} (\omega - \omega_1) \left\langle \left\langle x^l; H^k_{SO}; C \right\rangle \right\rangle_{0,\omega} \\ &= -N^{\mathbf{r}}_j(\omega_f) H^{[2]}_{SOjl} X_{lf} - N^{SO}_j \left(\mathbf{r}^{[2]}_{jl} + \mathbf{r}^{[2]}_{lj} \right) X_{lf} \\ &\quad + N^{\mathbf{r}}_j(\omega_f) \left(E^{[3]}_{jml} + E^{[3]}_{jlm} - \omega_f S^{[3]}_{jlm} \right) N^{SO}_m X_{lf}, \end{aligned} \qquad (55)$$

where the two linear response vectors $N^{\mathbf{r}}(\omega_f)$and N^{SO} are obtained by solving the two linear response equations:

$$\begin{aligned} N^{\mathbf{r}}(\omega_f) &= \left[\left(E^{[2]} - \omega_f S^{[2]} \right)^{-1} \mathbf{r}^{[1]*} \right]^*, \\ N^{SO} &= \left(E^{[2]} \right)^{-1} H^{[1]}_{SO}, \end{aligned} \qquad (56)$$

and the triplet excitation vectors (X_f) and frequencies (ω_f) are obtained from the solution of the triplet excitation eigenvalue equation:

$$(E^{[2]} - \omega_f S^{[2]}) X_f = 0. \qquad (57)$$

Eqn (55) and (56) include several types of response matrices. The matrices $E^{[2]}$ and $S^{[2]}$ are the Hamiltonian and overlap matrices in the T operator basis:

$$E^{[2]}_{jk} = \left\langle 0 \middle| \left[T_j^*, [H_o, T_k] \right] \middle| 0 \right\rangle, \quad S^{[2]}_{jk} = \left\langle 0 \middle| \left[T_j^*, [H_o, T_k] \right] \middle| 0 \right\rangle. \qquad (58)$$

The one-index matrices over the perturbing operators, with superscript "[1]" are called gradient vectors and are defined as:

$$\mathbf{r}^{[1]}_j = \left\langle 0 \middle| \left[T_j^*, r \right] \middle| 0 \right\rangle, \quad \mathbf{r}^{[1]}_{SO,j} = \left\langle 0 \middle| \left[T_j^*, H_{SO} \right] \middle| 0 \right\rangle \qquad (59)$$

for the dipole and spin–orbit operators, respectively. The two-index matrices with superscript "[2]" are defined similarly with double-commutator expressions.[53b,92] The three-index matrices are higher order generalizations of the two-index matrices. The important point is that they are never constructed explicitly, but are handled directly in matrix–vector products using direct CI techniques in multiconfiguration SCF approaches[53b] and in DFT methods.[92] By inspection of eqn (55) the following four types of expressions are evaluated in case of phosphorescence: (i) $E^{[3]}$ times two vectors; (ii) $S^{[3]}$ times two vectors; (iii) $r^{[2]}$ times a vector; and (iv) $H^{[2]}_{SO}$

times a vector. The computationally dominant operation is evidently the first of these four contractions, the one which contracts a third-order Hessian type matrix with two response vectors.

The main advantages of the employed MCQR theory can be summarized as follows: (1) the sum-over-state expressions, eqn (50), in the QR theory have been replaced by solutions of sets of linear equations. By this one obtains implicitly a complete sum of excited states of the expression for phosphorescence without need for truncation, which is of great theoretical as well as practical numerical advantage. Since these solutions can be determined using direct iterative techniques of the response equations, large dimensions and therefore large orbital and configurational space of MCSCF wave functions can be considered. In the usual MO theory the sum-over-state row, eqn (50), converges slowly; even at large n and m the results are different upon truncation of the row (up to n = 100).[53b] Errors from truncation of the slowly convergent summations, employed in conventional CI procedures, are thus completely avoided in the QR approach. (2) The QR method used is fully analytical and can be considered as an analytic analogue of the finite field calculation of the dipole transition moment from the MCSCF linear response calculation where the SOC operator is the applied field. (3) Both orbital excitation operators and configuration excitation operators describe the electron correlation. Conventional CI approaches use only the latter and require larger CI spaces to obtain an equal correlation level. (4) A full Breit–Pauli form of the spin–orbit operator, including one- and two-center SOC integrals and one- and two-electron terms, is employed.

In order to estimate correctly the phosphorescence lifetime, eqn (52), the SOC operator in eqn (50) is used in a semi-empirical effective single-electron approximation, suggested by Koseki *et al.*[53c,d,95–97] The approximation made by using this operator has been thoroughly evaluated in our previous studies[51,61–64] where the assessment of all electron basis sets as well as effective core potentials (ECP) was considered. In this approximation one reduces the number of electrons and removes the two-electron part of SOC, which greatly facilitates the calculations. For analysis of phosphorescence vibronic activity we need to consider vibrational frequency and modes of the ground and excited states. The general expansion of the total wave function of the ground state in the adiabatic approximation $\Psi_{S_0,n}(q,Q) = S_0(q,Q)\Phi_n(Q)$ can be used, where S_0 is the electronic ground state wave function, q and Q denotes electronic and nuclear coordinates.[51] In the harmonic approximation the nuclear wave function $\Phi_n(Q)$ is a product of wave functions of all vibrational modes Q_i. Only one of them is considered to be excited in the state with n = 1 quantum number, thus we neglect combinational lines and overtones. In such an approach the 0–n vibronic line intensity is determined by the following $T_1^\alpha \rightarrow S_0$ transition dipole moment:[51]

$$\left\langle T_1^\alpha(0)\middle|\vec{q}+\vec{Q}|S_0(n)\right\rangle = \left\langle T_1^\alpha|\vec{q}|S_0(n)\right\rangle_0\langle 0\mid n\rangle + \left(\frac{\partial M^\alpha_{T,S}(Q)}{\partial Q_i}\right)_0\left\langle \Phi_0\middle|\vec{Q}_i|\Phi_n\right\rangle, \quad (60)$$

where

$$M^\alpha_{T,S} = \left\langle T_1^\alpha(q,Q)|\vec{q}|S_0(q,Q)\right\rangle \quad (61)$$

is the electronic T–S transition moment calculated at different displacements Q along the normal mode.

The first term corresponds to the Franck–Condon (FC) mechanism and the second term is determined by spin–vibronic perturbation, *i.e.* by derivative of spin-forbidden transition moment with respect to displacement along the Q_i normal mode. The first term includes the vertical transition weighted by the FC factor $\langle 0|n\rangle^2$, which can be estimated through the Huang–Rhys parameters.[98] The FC mechanism is important for those modes which are changed upon the T → S transition. Displacement of the equilibrium positions for such modes is estimated by gradients of potentials in the S_0 and T_1 states, calculated by the DFT method.[98] The second term in eqn (60) represents our version of the Herzberg–Teller correction, calculated by the QR method from eqn (50) at different points along the displacement Q.

4.6. Alq_3 phosphorescent OLED as an example of quadratic response calculations

Our DFT QR calculations of the phosphorescence rate constant and lifetime in the Alq_3 complex (Fig. 1) have shown that the pure electronic T_1–S_0 transition is very weak and cannot explain the observed phosphorescence lifetime (17 ms) in Alq_3 crystal at 6 K.[11] A calculation of the ten lowest S_0–T_n transitions dipole moments indicates that the phosphorescence of Alq_3 borrows intensity from the upper T–S transitions by vibronic interactions. The active mode (550 cm^{-1}) which is well-seen in the vibronic progression of the phosphorescence band in all studied crystalline and amorphous phases is connected with the metal–ligand vibrations. The calculated ZFS parameters (D = 0.084 and E = 0.005 cm^{-1}) show comparable contributions from both SOC and spin–spin coupling and agree well with the ODMR measurements, indicating the interligand $\pi\pi^*$ character of the T_1 state. Only the upper states with high metal-to-ligand charge transfer (MLCT) character provide an appreciable radiative activity of the observed phosphorescence through the Al–O stretching vibrations.

As a pure LUMO-channel conductor Alq_3 is also a good material for spintronics.[11] On the basis of the calculated SOC integrals, the authors of ref. 11 have proposed that an efficient spin-polarized injection and transport in the long channels of the Alq_3 semiconductor can proceed with a triplet electronic charge–transfer state admixture at the interface which is transmitted to the charge carriers. Indeed, a successful spin injection in one end and the polarized spin recovering at the other electrode have been achieved with a new hybrid organic–inorganic interface.[91b] Enhancement of vibronic and SOC effects at the interface with the presence of a polar LiF thin layer and the energy shift in the HOMO level of Alq_3 permit the spin injection operating even at 100 mV. A very weak SOC for the lowest T state of a pure Alq_3 provides an efficient spin-dependent current in a conductor channel.[11] The doublet states of the electron spin carrier can be mixed by SOC (quenching of spin polarization) only through the exchange-induced admixture of the so-called triple excitations which include a triplet spin state inside a doublet. Calculations of SOC show that this effect is negligible in the Alq_3 channel.[11]

For typical electrodes used in OLEDs the spin-polarized injection vanishes. Nevertheless, SOC effects play essential roles in the mechanisms determining OLED efficiency.

We can conclude that applications of the QR technique at the DFT and MC SCF levels for phosphorescence spectra provide a reliable explanation of numerous T–S emissions in organic and elementoorganic molecules which serves as a useful tool in OLED theory.[51,60–64]

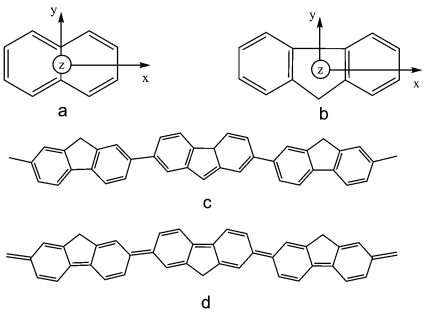

Scheme 1 The choice of axes for the naphthalene (a) and fluorene (b) molecules and the changing of bond alternation in polyfluorene chain (c, d) under excitation to the T_1 state.

5. Phosphorescence of organic molecules and polymers

5.1. Naphthalene as example

Let us consider some general features of phosphorescence of π-conjugated organic chromophores[38,46–51] taking as an example the naphthalene molecule. The $T_1^\alpha \rightarrow S_0$ transition moment with γ polarization of the emitting light, eqn (50), is calculated by the quadratic response (QR) theory[53b] reviewed above. The old semiempirical CNDO/S CI calculations of the radiative phosphorescence lifetime in aromatics[47] have used the one-electron form of the SOC operator, eqn (29)–(31), taking account of only one-center contributions, eqn (40). Therefore the *ab initio* QR treatment[46] provides a good test for the nature of the phosphorescence of π-conjugated organic molecules. The results for naphthalene are presented in Table 1. The double zeta Rydberg (DZR) basis set is used. The choice of axes is shown in Scheme 1. In the D_{2h} point group the *x*, *y* and *z* components of the electric dipole moment (and magnetic dipole, in brackets) are transformed as B_{3u}, B_{2u} and B_{1u} (B_{3g}, B_{2g} and B_{1g}) irreducible representations, respectively. The magnetic dipole (this is actually the orbital angular momentum) symmetry coincides with the irreducible representations of the spin functions, eqn (42), in the double point group.[38]

The CNDO/S CI results as well as the multiconfigurational linear response data (with the ground-state CAS) give energy values in a reasonable agreement with experiment, especially for the two lowest singlet and triplet states (Table 1). The higher lying singlet state energies have been improved by addition of Rydberg orbitals in our MC linear response method (the DZR basis set[46]). By this addition, the energy of the σ → π* excitations in naphthalene ($^1B_{1u}$, states) diminishes drastically, indicating the large Rydberg character of these states.[46] These lowest σπ* states appear in the region of very intense π → π* absorption and have rather small electric dipole transition moments from the ground state.[46,47] Thus, these out-of-plane polarized transitions are overlapped and buried by the in-plane polarized π → π* absorption.

All low-lying B_{3u}, B_{2u} states are of the ππ* type in naphthalene. The SOC matrix elements between the S and T states of this type are equal to zero in the one-center approximation, eqn (40).[47] In this case the T_1–S_0 transition can be out-of-plane polarized. In fact, the lowest $^3B_{2u}$ triplet state emission in the *ab initio* MCQR calculations is predicted to possess 99.3% polarization in the out-of-plane direction.[46] This phosphorescence of the π-conjugated naphthalene molecule is borrowed mostly from the σ → π* and π → σ* transitions of the 1^1A_g–$^1B_{1u}$ type, which occur in the far UV region (Table 1). Small additional contributions to the T_1–S_0 transition moment are produced also from the first term of eqn (50): these are connected with the weak 1^3B_{2u}–$^3B_{3g}$ transitions of the σ → π and π* → σ* types between triplet excited states.

Phosphorescence in naphthalene, the $1^3B_{2u}(T_1) \rightarrow 1^1A_g(S_0)$ transition, is allowed from the $T_1^z(B_{3u})$ and $T_1^x(B_{1u})$ spin-sublevels; in brackets the total symmetry is shown, for example: T_1^z ($B_{2u} \times B_{1g} = B_{3u}$). Thus, this sublevel can be mixed with the singlet $^1B_{3u}(\pi\pi^*)$ state. *Ab initio* calculations with the Breit–Pauli form of the complete SOC operator provide almost negligible mixing of this type. Consequently, the $T_1^z \rightarrow S_0$ transition with the light polarization along the *x*-axis is calculated to be very weak; the rate constant for spontaneous emission $k_x(T^z) = 4.05 \times 10^{-4}$ s^{-1} and the radiative lifetime is equal to 2466 s.[46] In contrast, the $T_1^x(B_{1u})$ spin-sublevel provides the out-of-plane polarized phosphorescence with the higher rate constant $k_z(T^x) = 0.057$ s^{-1} and radiative lifetime of 17.6 s.[46] Optical detection of magnetic resonance (ODMR) at low temperature (4.2 K) permits to measure the individual spin sublevel lifetimes;[60f,g] it indicates that the T_1^x spin sublevel is the most active one in phosphorescence of a naphthalene single crystal.

Table 1 The energies and oscillator strengths (*f*) for the low-lying singlet and triplet states of the naphthalene molecule calculated with various methods

	E/eV				*f*			
State	DZR[46]	CNDO/S[47a]	DFT	Exp.	DZR[46]	CNDO/S[47a]	DFT	Exp.
1^3B_{2u}	2.38	3.11	2.54	2.63	2.3×10^{-10}	0.7×10^{-10}	2.87×10^{-10}	1.6×10^{-10}
1^3B_{3u}	4.19	3.93	3.89	3.71	4.8×10^{-9}	—	2.57×10^{-9}	1.6×10^{-9}
1^1B_{3u}	4.02	4.07	4.39	3.97	3.0×10^{-4}	10^{-3}	10^{-4}	10^{-4}
1^1B_{2u}	6.06	4.33	4.29	4.65	0.12	0.12	0.066	0.1
1^3B_{1u}	7.24	6.17	7.5		6.3×10^{-8}	9.7×10^{-8}	1.0×10^{-8}	

But the observed lifetimes are too short because of very fast nonradiative quenching in nondeuterated naphthalene.[60i] Most phosphorescence measurements are performed in solid solvents frozen at 77 K.[4] At these conditions the nonradiative transitions between spin-sublevels (spin–lattice relaxation) proceed faster than the phosphorescence occurs and a thermal equilibrium can be established before emission; thus, only the averaged lifetime can be measured at 77 K.

The MCQR result in the DZR basis set predicts τ_{av} = 52.4 s,[46] which is almost equal to $3\tau_x$. There are several estimations of the radiative averaged lifetime derived from experiment.[4] The lifetime for naphthalene-h_8 diluted in a durene host crystal at 77 K (2.1 s) increases upon deuteration to 17 s.[4] In the latter case the nonradiative quenching rate (k_6, Fig. 4) is suppressed because the C–D vibrational frequencies are much smaller than those for the C–H bond vibrations and the higher v quantum numbers are necessary to accept the electronic ΔE_{TS} energy. The corresponding Franck–Condon and Huang–Rhys factors, eqn (18), are smaller. Therefore, the quenching rate k_6, diminishes considerably upon deuteration,[35,60i] but the lower limit is difficult to estimate since the total T_1 state decay in naphthalene is very slow. The lifetime of the triplet state is given by $\tau = (k_7 + k_6)^{-1}$ where k_7 and k_6 are the rate constants for radiative (7) and non-radiative (6) decay in Fig. 4.

Ermolaev established[37b] by very sensitive measurements that the nonradiative quenching rate k_6 for naphthalene-d_8 is still six times as great as the k_7 rate constant, which determines the pure radiative lifetime $\tau_{av} = 1/k_7$. Consequently, the radiative lifetime (τ_{av} = 63 s) is much higher than the observed phosphorescent lifetime.[37b] Our result (52.4 s) supports this estimation of Ermolaev for the averaged radiative lifetime of naphthalene phosphorescence.[46]

In this respect it is also interesting to compare the results of the MCQR calculations with the oscillator strength (f) for the $T_1 \leftarrow S_0$ absorption, studied in pure crystalline naphthalene.[4] From absorption measurements the value $f = (1.6\text{–}16) \times 10^{-10}$ has been obtained.[4] The MCQR calculated value $f = 2.3 \times 10^{-10}$ enters this interval. The absorption intensity for the second triplet state $T_2 \leftarrow S_0$ is a factor of 10–100 times higher than that for the T_1 state.[4] This trend is also in agreement with the *ab initio* response calculations (Table 1). The $T_2(^3B_{3u}) \leftarrow S_0(^1A_g)$ transition has a large component $M_z(T^y) = 0.000161$ a.u., while the other symmetry-allowed transition to the T_2^z spin sublevel is less intense: $M_y(T^z) = -0.000015$ a.u. Even for the second $^3(\pi\pi^*)$ state the SOC-induced mixing with the singlet $^1(\pi\pi^*)$ states is very small. This supports the idea that the semiempirical approximation, eqn (40), which neglects spin–orbit coupling between S and T states of $\pi\pi^*$ type, is quite reasonable.[38] Indeed, semiempirical calculations of SOC in terms of the CNDO/S CI approximation[47a] provide quite reasonable agreement with results of the *ab initio* MCQR technique (Table 1).

5.2. Phosphorescence of π-conjugated planar organic molecules

The results for naphthalene are typical for MCQR calculations of SOC in other organic unsaturated molecules.[43,44,47–53] The phosphorescence lifetimes reported from experiments in solid matrices at 77 K (even being scaled by the quantum yield)[4] are typically too low in comparison with the *ab initio* MCQR calculations, because of the difficult measurements of the quenching rate k_6. The ODMR experiments on phosphorescence of organic mixed crystals at the liquid helium cooling provide very good agreement with theoretical prediction of the individual spin sublevel lifetimes.[38,43,44,53]

The phosphorescence of the π-conjugated planar organic molecules corresponding to he lowest triplet state of the $^3(\pi,\pi^*)$ type is borrowed mostly from the $\sigma \rightarrow \pi^*$ and $\pi \rightarrow \sigma^*$ transitions, which provide its out-of-plane polarization. For organic molecules with heteroatoms the occurrence of the low lying $^{1,3}(n,\pi^*)$ states can lead to essential change of the luminescence properties depending on their relative positions.[3,4] These known peculiarities[4] are reasonably well reproduced in our MCQR calculations.[44,46]

If the electronic $T_1^z \rightarrow S_0$ transition is forbidden by symmetry (even with taking SOC into account), the vibronic spin–orbit coupling perturbation is well reproduced at the MCQR level.[43,50,53a]

Extension of the quadratic response approach at the level of density functional theory (DFT)[51b] provides a similar level of accuracy for phosphorescence lifetime calculations in very large organic[51] and elementoorganic molecules.[59–64] This gives background for a useful phosphorescence analysis in numerous OLED applications.[65–70]

5.3. Use of polymer luminescence in modern OLEDs

The development of polymeric light-emitting diodes provided considerable advantages in comparison with traditional ones[1] because polymeric materials could be applied to low-cost production of EL devices exhibiting efficient luminescence for flat-panel displays.[9] The polymeric property of the OLED materials enables efficient device fabrication processes, such as spin-coating, screen printing, and ink-jet printing,[9] large-area and fine-pixel displays that could be easily developed in comparison with the vapor deposition process.[9c] Pure polymeric OLED devices are now available on the market even though the polymers still have a drawback in lower luminescence efficiency.[9b,d] Such pure polymeric OLEDs require a smaller number of layers in the EL device, which enables a low driving voltage and low cost.[9d]

Many OLEDs use widely developed fluorescent π-conjugated polymers, such as polyfluorenes (PFs) and polyphenylene vinylenes (PPVs), as well as non-conjugated polymers of the polyvinylcarbazole (PVK) type. Considering PVK as a good example one can certify that this semiconducting polymer acts as a high-performance hole transport layer in OLED technology.[71] Being doped by cyclometalated iridium complexes, PVK can be used as an emitting layer in the same OLED devices. The PVK polymer has a larger emission cross section for singlet than for triplet states, and the presence of the phosphorescent iridium complexes is expected to cause a total energy transfer from PVK already at very low doping concentrations.[71,72]

Pure polymeric phosphorescent OLED materials consist of host polymers such as PVK and poly(9,9-di-*n*-octyl-2,7-fluorene) (PFO), into which the phosphorescent small molecules are doped. In such polymers the phase separation and crystallization of the small molecules in the polymer matrix may reduce the luminescence efficiency due to the self-quenching mechanism.[9c] Another type of polymers having phosphorescent pendant units in the side chain is now known.[9d] Non-conjugative copolymers have also been developed in which monomers having luminescent cyclometalated iridium pendant units are copolymerized.[65] Conductive polymers are generally not thermoplastic. Due to their poor processability, conductive polymers have few large-scale applications, the former OLEDs[20] being one of the most important results. Studies of their properties are though still useful for modern OLED technology.

5.4. Luminescence polarization in stretched polymers

At this point we can consider in more detail the results of the luminescence polarization measurements in stretched polymers, such as those of King *et al.*[17] who have measured optical polarization of fluorescence, phosphorescence, and photoinduced absorption in the oriented polyfluorene films. They have found polarized S_0–S_1 absorption, fluorescence spectra and the T–T absorption in stretched polymer films being mostly oriented parallel to the polarizer and the polymer chain with a high dichroic ratio. The emission band was more strongly polarised than the S_0–S_1 absorption.[17] This indicates that the singlet exciton is more planar than the ground state switched polyfluorene; the result is completely confirmed by independent DFT calculations of Ågren *et al.*[20] Indeed, geometry optimization of a series of conjugated fluorene oligomers in the S_0, S_1, and T_1 states indicates a gradually increased strong planarization of the oligomer chain upon these excitations. The dihedral angle (θ) between adjacent monomer units goes from $\theta = 37^\circ$ in the ground state to $\theta = 14^\circ$ upon excitation to the S_1 state, and finally down to 1.9° for the triplet exciton.[20] It is also noted that the structural change in dihedral angles becomes more and more localized as longer oligomers are considered. Analysis of the calculated bond length changes upon S and T excitations indicates that a quinoid structure is formed in the middle of the polymer. These structural deformations are localized almost in two fluorine units, a characteristic feature of exciton structure for all studied oligomers.[20] King *et al.*[17] have shown that the phosphorescence polarization in this polyfluorene homopolymer, in contrast to the S_0–S_1 spectra, has its dominant component orthogonal to the chain orientation.[28] The polarised photoinduced triplet–triplet T_1–T_n absorption shows that the higher excited triplet transitions have a dipole moment along the chain with a high dichroic ratio. Thus, the T_1–T_n transition is more like the transitions of singlet character, with the change in electron distribution during the transition occurring along the chain.

The authors of ref. 17 have suggested that the electron distribution in the T_1 excited state is oriented perpendicular to the backbone of the polymer, while the ground state S_0 and excited S_1 and T_n states are elongated along the polymer chain. This conclusion has to be corrected accounting for the fact that all spin allowed transitions are determined by their own transition dipole moments of $\pi \rightarrow \pi^*$ type, but the spin-forbidden T_1–S_0 transition borrows its intensity mainly from the $\sigma \rightarrow \pi^*$ and $\pi \rightarrow \sigma^*$ excitations, which have perpendicular polarization. All studied excited states in ref. 17 and 20 including the phosphorescent T_1 components have $\pi\pi^*$ character; thus, any deformation of their wave functions upon excitation are elongated along the polymer chain. All $\pi \rightarrow \pi^*$ transitions are polarized along the polymer axis and the anomalous dichroic ratio ($A^{\parallel} < A^{\perp}$) of phosphorescence is just a consequence of the SOC anisotropy and its well-known peculiarity.[41] The T_1 excited state wave function is oriented in the same manner like all other $\pi\pi^*$ states, but only a very small admixture of the singlet $^1\sigma\pi^*$ character, induced by SOC, is responsible for the phosphorescence polarization (this admixture is practically negligible for electron density orientation in the T_1 state, being responsible at the same time for the T_1–S_0 transition moment and optical polarization).

Calculations indicate that the fluorene molecule (Scheme 1) has a long axis (x) polarization of the $S_1 \rightarrow S_0$ transition while the higher absorption band ($S_2 \leftarrow S_0$ transition) is polarized along the short axis (y) – both axes being in the molecular plane as it is necessary for $\pi\pi^*$ excited states. The intense T_1–T_n transition at 416 nm is also calculated to be polarized along the x axis and indicates the $\pi\pi^*$ nature of both states. Thus, all results of ref. 20 are understood without assumption that the T_1 state electron distribution is oriented orthogonal to the chain.

The main contribution to the phosphorescence transition moment of such popular polymeric blocks as dibenzofuran and carbazole monomers (similar to fluorine) originates from direct spin–orbit coupling of the lowest triplet $^3\pi\pi^*$ state with the singlet excited states of the $^1\pi\sigma^*$, $^1\sigma\pi^*$ and $^1n\pi^*$ types.[38,44–53] Thus, they give rise to the large extent of the out-of-plane polarization.[45] The same results are obtained for quinoxaline and naphthalene, both from theory[46] and experiments, in stretched polyethylene films.[45] The in-plane contribution is small since direct spin–orbit coupling between the $^3\pi\pi^*$ and $^1\pi\pi^*$ type levels is very ineffective.[4,38,44,47,48] It is to be ascribed to small three-center spin–orbit integrals,[4,49] and to small second order Herzberg–Teller terms[50,51] in which the promoting modes are the out-of-plane vibrational modes.[46,48,50,53a] The $\pi\pi^*$–$\sigma\sigma^*$ mixing induced by configuration interaction (CI) is efficient only for the singlet (highly excited) states, but not for the triplet lowest state.[47]

From the experimental data it is obvious that the 0–0 phosphorescence band of carbazole and dibenzofuran are more in-plane polarized than that of fluorene.[45] This would mean that the Herzberg–Teller vibronic contribution is larger for carbazole and dibenzofuran than for fluorene, as the spin–orbit coupling is expected to be approximately the same for these compounds. The polarization of vibronic bands in the phosphorescence spectra studied by photoselection experiments confirm the stronger vibronic activity in carbazole compared with fluorene.[45]

5.5. ISC in conjugated polymers

The rate of intersystem crossing (ISC), $S_1 \rightarrow T_1$ in conjugated polymers, like PPV or PF, is determined by the second order effects, since the direct SOC matrix element $\langle S_1|H_{SO}|T_1\rangle$ is negligible. Both S_1 and T_1 states are of the similar $\pi\pi^*$ nature produced mostly by the HOMO $\rightarrow$ LUMO configuration. For all OLED applications the ISC and the phosphorescence rate are of great importance. Besides these other reasons, these ISC processes just provide the possibility to measure the T_1 state energy in photoluminescence studies. Monkman *et al.*[24] reported that the triplet yield in polyfluorene and PFO was found to be 0.05 with an ISC rate $k_5 = 5.4 \times 10^7$ s^{-1}. Because of the spin-forbidden nature the radiative decay rate of the T_1 state is extremely low and very difficult to quantify experimentally. At low temperature (20 K) and low excitation doses Monkman *et al.*[24] determined the decay rate as low as 1 s^{-1}. QR DFT calculations predict the radiative phosphorescence lifetime for polyfluorene oligomer series to be 28.4, 17 and 13.5 s for n = 1, 2 and 3, respectively. All pure radiative decay rates are less than 0.1 s^{-1}. Therefore, the nonradiative quenching rate, k_6, is much higher than k_7 (Fig. 4), calculated by quadratic response.[43] We can see that the triplet states in organic polymers, being highly populated *via* charge recombination in OLEDs upon bias remain dark and useless states doomed for heating degradation. Luminescence of the polyfluorene thin film in the blue region is bright and has a lifetime of few ps.[24] Since the singlet exciton embraces a long distance (1.8 nm) in the polymer chain[20a] the $S_1 \rightarrow S_0$ transition moment is large, being proportional to the length of the exciton delocalization. In spite of the bright fluorescence, this limits the internal quantum efficiency of polymeric OLEDs, which is determined entirely by singlet excitons (25%), while the triplet counterparts (75%) remain useless. The reason for the good and bad features of such OLEDs is connected with the same characteristic property – the π-conjugation in the polymer. All low-lying S and T excited states are of $\pi\pi^*$ nature and there is no room for the orbital angular momentum change between them, determined by eqn (35) and (40). Thus, there is no SOC-induced S–T mixing, which is crucial for the high internal quantum efficiency of OLEDs. This disadvantage of the polymer materials is overcome by insertion of organo-metallic complexes into the OLED emissive layer.

6. The first successes on the way to phosphorescent OLEDs

6.1. Preliminary remarks

Typical values for the triplet state radiative decay rate, k_7 (Fig. 4), range around 0.1 to 100 s^{-1} for organic molecules and polymers[4,24] and around 10^3–10^5 s^{-1} for organometallic dyes[34] as it is established from the measured phosphorescence quantum yields and lifetimes. Accounting that the nonradiative decay rate, k_6, is typically about 10^4–10^6 s^{-1} [4,37] and decreases with the T_1–S_0 energy gap one can see that the phosphorescence lifetime of organic polymers is entirely controlled by non-radiative relaxation. The energy gap law also explains why the first measurements of organic polymer phosphorescence have been made for the blue emitting family of poly(*p*-phenylenes) with a relatively high energy of the T_1 state around 2.3 eV.[56a] For organometallic complexes of Pt and Ir ions the k_6 and k_7 rate constants can become comparable at room temperature and the phosphorescence can compete with non-radiative relaxation.

Therefore, electroluminescent devices based on organometallic triplet state emitters have attracted great attention during last decade because of their potential to achieve the largest possible (100%) internal quantum efficiency for the conversion of electric energy to photons.[9,31,33,34,66–70] The idea to compel triplet excitons to do useful work in OLEDs was proposed in the early nineties.[79a,b] However, the first attempt to incorporate a phosphorescent dopant into polymer matrices was unsuccessful. Hoshino and Suzuki[79c] used benzophenone (BP) as a phosphorescent material doped into poly(methylmethacrylate) but no energy transfer from the host was found. A very low efficient EL from BP was detected at 100 K in poly(methyl methacrylate) (PMMA) with much shorter lifetime (0.047 μs) than the normal photo-phosphorescence, demonstrated at the same conditions (5.3 μs).[79c] Much stronger phosphorescent emitters with shorter radiative lifetimes than the pure organic benzophenone (BP) molecule were thus needed. The averaged phosphorescence lifetime of BP in our DFT QR calculations is about 10 μs, indicating the $^3n\pi^*$ nature of the lower triplet state. An effective quenching of the triplet BP in PMMA matrix occurs for such a long lived emitter even at low temperature.

6.2. Platinum octaethyl-porphyrine dopant

The first success in PhOLED fabrication was achieved by Baldo *et al.* who doped the host material Alq_3 with the phosphorescent octaethyl-porphine Pt(II) complex (PtOEP).[32a] Strong evidence of the Dexter energy transfer mechanism was obtained by comparison of various OLED devices with different thicknesses of Alq_3 layers doped with phosphor and fluorophore emitters.[32a] The OLED efficiency improvement was made possible by participation of triplet excitons in phosphorescence, though the long lifetime (about 0.1 μs) causes saturation of emission at low dopant concentration and high currents.

The presence of Pt(II) ions reduces the phosphorescence lifetime by increasing spin–orbit coupling which enhances the intersystem crossing between the S_1 and T_1 states. Therefore, the radiative and non-radiative decay rates become competitive and comparable (about 10^4 s^{-1}) and the excited triplet state can perform useful work. Really, the singlet emission in the electrophosphorescent spectra of PtOEP-based OLEDs with the different concentration of PtOEP is not observed, but strong emission is observed from the T_1 excited state near 650 nm seen at the vibronic progression with the maxima at 623, 687 and 720 nm.[32a] After this great success in PhOLED fabrication with the PtOEP dopant[32a] an attempt of theoretical interpretation of this result has been performed in terms of TD DFT calculations with quadratic response account of the phosphorescence vibronic activity.[60a]

Table 2 Quadratic response DFT/B3LYP calculations of the phosphorescence rate on the ground of ref. 60*a,c,e*. ΔE is the transition energy, eV, M is the electric dipole $T_1 \rightarrow S_0$ transition moment in a.u., k_b[a] is the rate constants for emission from the T_1[a] spin sublevel, polarized along the *b* axis in s^{-1}; τ_p is the phosphorescent radiative lifetime at the low-temperature limit (4 K) and high-temperature limit (77 K). The *z* axis is perpendicular to the porphyrin plane

Molecule	ΔE	M_z^x	M_x^z	k_z^x	k_x^z	τ_p (4 K)	τ_p (77 K)
FBP($^3B_{2u}$)[51a]	1.46	2.4×10^{-5}	6.0×10^{-7}	0.0018	0.6×10^{-6}	540	1619
FBP, expt.[60b]				0.002		500	Long
MgP (^3E_u)[60c]	1.72	6.6×10^{-5}	1.2×10^{-6}	0.024	1.0×10^{-5}	42.4	127
MgP, expt.[60f]	1.70			0.021			47
ZnP (^3E_u)[60c]	1.81	7.1×10^{-5}	1.8×10^{-4}	0.031	0.203	4.9	12.8
ZnP, expt.[60f]	1.82			0.16	1.0		10
PtP (^3E_u)[60a]	1.95	1.6×10^{-2}	3.0×10^{-2}	1980	6.98×10^{3}	1.4×10^{-4}	3.3×10^{-4}
PtP, expt.[60d]	2.02			0.2[a]	1.0[a]		1.0×10^{-5}

[a] Relative values.

The key problem with porphyrin-based dopants was connected with the fact that porphyrins, and free-base porphine (FBP) in particular, have very weak phosphorescence.[51a,60] For FBP and for porphyrins with light metal-ions the radiative lifetime of phosphorescence is unusually long (for FBP it is estimated as 500 s,[51a,60b] for Mg-porphyrin as 47 s,[60c] Table 2), though the porphyrin core contains nitrogen atoms with lone pairs. It was difficult to estimate from experiment the non-radiative contribution to the observed phosphorescence lifetime for such weak emission[60b] and only DFT QR calculations[51a,60c] could provide strong support for the unusually long pure radiative lifetime. The presence of n-orbitals and nπ* states usually ensures the necessary conditions for strong phosphorescence because of effective mixing between the S and T states of nπ* and ππ* nature induced by one-center spin–orbit coupling. In the case of porphyrins such contributions are cancelled by symmetry for the $T_1 \rightarrow S_0$ transition.[51a,60c]

It is interesting that just the porphyrin derivative PtOEP was used as an effective phosphor dye in the first PhOLED[31] in order to overcome the useless dark triplet excitons in the organic polymer matrix. In fact the ISC process is quite efficient in porphyrins and only the low electric-dipole activity of the $T_1 \rightarrow S_0$ transition provides here a difficult problem.[60a] Photophysical properties of platinum porphyrins cannot be easily explained by simple correlation with atomic number.[60a]

The heavy element of Pt does not perturb greatly the absorption spectra of the whole series of porphyrins: the Q band and Soret bands are only slightly blue shifted. These are the same ππ* transitions in the tetrapyrrole ring like in FBP and light-metal porphyrins, which have very small contributions from d-orbitals of the metal (and small ligand-to-metal CT admixture).[51a,60a] A question arises as to why the luminescence properties of Pt-porphyrin (PtP) and PtOEP change so dramatically? For Pt-porphyrins no detectable fluorescence was observed, meanwhile the phosphorescence yield and rate constant are strongly increased in comparison with FBP and light-metal porphyrins. The lowest triplet state and all spectroscopy-important singlet states observed in UV-vis absorption are of ππ* character with highly predominant excitation in the tetrapyrrole ring. From a phenomenological point of view it is more or less clear that PtOEP could be a useful phosphor emitter in the first successful PhOLED device, since its phosphorescence was known by measurements,[60b] however, from the quantum chemical point of view it was a puzzle.[60] The most important states for the phosphorescence intensity borrowing scheme are hidden and avoid experimental detection although they have low excitation energy in the visible region.[60a] It was shown that the low-lying charge-transfer states of dππ* type provide strong SOC contributions to the phosphorescence transition moment in the PtOEP dye.[60a] These are metal-to-ligand charge-transfer (MLCT) states which can assist in intermolecular interaction with the polarons of the polymer matrix and also induce T–S mixing with the ground state for effective intensity borrowing from the $T_1 \rightarrow T_n$ transitions.

Our TDDFT calculations have indicated an interesting trend in the series of metallo-porphyrins (Tables 2 and 3): the $T_1(^3E_u)$ state energies increase with the rise of the metal atomic number, but the low-lying charge-transfer A_{2g}, B_{2g} and E_g state energies decrease along the series;[51a] the S–T splitting of these CT states is small, not more than 0.3 eV. The former two states are of ππ* type with considerable CT character; these are $4e_g(d\pi) \rightarrow 5e_g(\pi^*)$ excitations. The singlet–singlet CT transition $X^1A_{1g} \rightarrow {}^1A_{2g}$ lies in the region of the first weak Q absorption band of Pt-porphyrin (500 nm), being forbidden by symmetry as an electric-dipole transition it is overlapped by the Q band. At the same time it is characterized by a large magnetic dipole transition moment (1.95 Bohr-magneton). The result correlates with the Zeeman effect measurements of the Q band.[51a,60]

Table 3 Triplet and singlet transition energies (ΔE, eV) and oscillator strengths (*f*) with respect to the ground state of platinum-porphyrin (PtP), calculated by time-dependent QR DFT B3LYP/Lanl2DZ at the ground state geometry (D_{4h} point group) by results from ref. 60*a*

		Triplets		Singlets	
Excited state	Degeneracy	ΔE	*f*	ΔE	*f*
^1E_u	2	1.943	5.5×10^{-5}	2.598	0.0033
^2E_u	2	2.252	2.6×10^{-4}	3.533	0.7158
$^1B_{2g}$	1	2.334	—	2.743	0
$^1B_{1g}$	1	2.432	—	2.790	0
$^1A_{2g}$	1	2.454	—	2.668	0
$^2B_{1g}$	1	2.518	—	4.324	0
^1E_g	2	3.063	—	3.114	0

All these features serve as an explanation of the relatively strong phosphorescence of PtOEP in comparison with other porphyrins and also of the high electron–hole recombination efficiency in the corresponding OLED.[31] The strong magnetic dipole moment for the singlet–singlet CT transition $X^1A_{1g} \rightarrow {}^1A_{2g}$ correlates with a large SOC matrix element between the ground singlet state X^1A_{1g} and the triplet CT state $^3A_{2g}$ (for the T^z spin sublevel, where the *z*-axis is perpendicular to the porphine plane). This becomes clear in terms of permutation symmetry allowing correlation between SOC integrals and changes in orbital angular momentum. In fact, direct SOC calculations support this analysis – the above matrix element is equal to the large absolute value of 1786 cm^{-1}.[51a] This is comparable to the SOC integral between the lowest $^3D_2$ and $^1D_2$ states of the platinum atom (3945 cm^{-1}). The ground triplet state $^3D_3$ $[5d^9(^2D_{5/2})6s]$ is accidentally very close to the $^3D_2$ state energy in the Pt atom (the gap is only 0.096 eV). The small gap is induced by SOC repulsion between the $^3D_2$ and $^1D_2$ states of the same *J* quantum number. Meanwhile, the upper spin sub-level of the same spacial triplet state, $^3D_1$, is as high in energy as 1.256 eV. This illustrates the great importance of spin–orbit coupling account in the spectra of the Pt atom with large deviations from the Lande interval rule.

We need to add that the triplet–triplet $1^3E \rightarrow 1^3A_{2g}$ transition in Pt-porphyrin (and the corresponding $T_1 \rightarrow T_n$ absorption band in PtOEP in the IR region, 0,5 eV, ref. 51*a*) is characterized by a very large electric dipole transition moment (0.92 a.u.). Therefore, the $T_1 \rightarrow S_0$ phosphorescence borrows intensity from the triplet–triplet $1^3E \rightarrow 1^3A_{2g}$ transition, with in-plane polarization. The other mechanism of intensity borrowing from the singlet–singlet Soret band is less efficient in PtOEP, in spite of qualitative proposals,[60a] because of small 5dπ contributions to the corresponding T_1 and S_n states (analogues to the 1^3E_u and 2^1E_u states in the planar Pt-porphyrin).

We summarize that the T_1 ππ* state in PtOEP produces strong phosphorescence from the T^z spin sub-level (in-plane polarized) with a radiative lifetime of about 0.1 μs. Emission from the $T^{x,y}$ sub-levels (out-of-plane polarized) is weaker and has 4–5 times longer decay.[51a] These results of DFT QR calculations are in a good agreement with experimental measurements at 4.2 K in doped crystals.[60]

The $T_1 \rightarrow T_n$ absorption of the charge-transfer character, being the main source of the PtOEP phosphorescence intensity, is predicted to occur in the IR region. Thus it is difficult to observe with a usual flash-photolysis technique. The singlet counterpart of the T_n state is not observable since the corresponding transition from the ground state possesses only magnetic dipole nature and is overlapped by the Q band. Thus the main source of the PtOEP emission deters any spectroscopic observations.

The other charge-transfer state of E_g symmetry (σπ*) is responsible for the out-of-plane polarization. The hypothetical ^3E_g states were thought to be important in the scheme of phosphorescence intensity borrowing proposed in ref. 60*d*, but our QR calculations do not support the main importance of such a mechanism. Earlier it was also proposed[60] that one has to consider SOC between the ^1E_u and 1^3Eu (ππ*) states as the main mechanism of the PtOEP phosphorescence intensity borrowing from the Q and Soret bands. This scheme should correspond to the observed in-plane polarization of the main part of the PtOEP phosphorescence.[60b] Our TD DFT QR calculations indicate that this spin–orbit coupling mechanism is not effective because of small 5dπ AO contributions to the LUMO of $5e_g$ (π*) type.[60a] Account of the metal-to-ligand charge-transfer state 1^3A_{2g} of the ππ* type is a key factor in the PtOEP phosphorescence theory and also for a consistent explanation of OLED efficiency. The low energy of the 1^3A_{2g} CT state (2.4 eV) in Pt porphyrins and its admixture to the ground state explains not only the relatively large phosphorescence rate constant, but also a strong intermolecular interaction between the triplet state of the guest phophor and the excitons in the emissive layer of the host polymer.[60a]

Although the PtOEP dye provides the essential external and internal efficiency improvement, made possible by the triplet exciton participation in light emission, the relatively long phosphorescence lifetime of PtOEP (0.1 μs) and the short-range nature of the Dexter mechanism of triplet energy transfer lead to saturation of the phosphorescence emission at low concentrations of the dye in the polymer matrix.[31] At high current and dopant concentration the T–T annihilation and other bimolecular interactions quench the phosphorescence. Involvement of a low-lying CT state in the phosphorescence leads also to a strong interaction between triplet dyes and efficient T–T annihilation[60a] at high exciton densities. The search for other phosphorescent complexes of heavy metals emitting in the blue and green regions of the spectrum led finally to a new perspective of the dyes as reviewed in the following section.

7. Implementation of Ir(III) complexes in phosphorescent OLEDs

7.1. Cationic and cyclometallated Ir(III) complexes

Soon after fabrication of the PtOEP-based devices, the iridium containing cyclometalated compounds came to represent a new paradigm in OLED technology.[32b] Complexes of the triply ionized iridium atom with organic ligands have attracted the greatest attention among other heavy-metal containing dyes in PhOLED applications.[9,31–35] They permit the the largest possible internal quantum efficiency for electric energy conversion into light to be achieved. Such OLEDs have an additional advantage that their emission spectra can be tuned from blue to red by the peripheral substitution of the ligands with electron-withdrawing and electron-donating substituents.[68,71,72] These properties make such phosphor emitters particularly attractive not only for OLEDs but also for light-emitting electrochemical cells (LECs).[59,68]

The pioneering research of Watts *et al.*[73,74] put forward a surge for phosphorescent cyclometalated complexes of iridium ions which found numerous applications in PhOLEDs of the last generation. In general, OLEDs offer a high-precision display with low power consumption in comparison with that of analogues based on liquid crystals. The PhOLEDs represent a novel and very attractive class of solid-state light sources, which generate a diffuse,

non-glaring illumination with high color performance. Polymeric PhOLEDs also allow for the possibility of flexible displays, being the most promising for the next-generation of mobile phones, TV sets, laptop computers and other microelectronic devices.

The materials used as effective emitters in a new class of OLEDs attract great interest not only because of their technological importance in the fabrication of efficient low-cost lighting devices,[9,76] but also because of their impact on our increased understanding of new photophysical phenomena and conformity to natural laws of molecular electronics. This field of knowledge is based on the quantum theory of molecules in vacuum and in the condensed phase including relativistic effects as an essential part of new scientific areas such as OLEDs and spintronics. Molecular electronics started initially with single crystals and polymers of organic unsaturated molecules with greatly developed p-conjugation chains. Now it is more concentrated on metallo-organic systems and interfaces, graphenes, nanotubes and other materials expanding molecularity to infinite limits. OLEDs are very important in these series because the electricity → light transformations embrace various requirements for materials functionality. The most efficient OLED materials are also useful for other devices intended for the opposite function (electricity ← light). The dye-sensitized solar cells (DSSC)[9,69,77,78] represent valuable addition in terms of a global challenge to utilize solar energy; together with OLEDs they can be integrated into a unique photonic device in order to utilize the captured solar energy for low-consumption lighting during dark periods.

In this review we will concentrate our attention on iridium complexes, containing large π-conjugated ligands, like 2-phenylpyridine anions (ppy) and neutral 2,2′-bipyridines (bpy), that have an advantage that their emission wavelength can be tuned from blue to red by the peripheral substitution of phenylpyridines, by electron-withdrawing and electron-donating substituents or by replacement of chelating ligands. Therefore, we have to begin with a few main chemical concepts connected with this important class of dyes in organometallic chemistry of iridium.

7.2. Synthesis and structure

Cyclometalated Ir(III) complexes are characterized by the quasi-octahedral coordination geometry, which is formed by three anionic bidentate ligands. According to the Chugaev rule, the five-membered Ir-containing cycles are especially stable and chemically inert. Thus, the post-synthetic modification of the ligands can be carried out without disturbance of the complex structure. The typical scheme of synthesis of the homoleptic cyclometalated Ir(III) complexes is presented in Fig. 8, considering the 2-phenylpyridinate ligand as an example.

On the first step of the synthesis the bis μ-chloro dinuclear Ir(III) complex has been formed. The chlorides in this complex are then substituted with the third C^N ligand identical to the other two ligands. Such complexes are usually named as homoleptic (all ligands are identical). If the third ligand is different (L^X or N^N, for example) than the two other C^N ligands, the iridium complexes are named as heteroleptic.

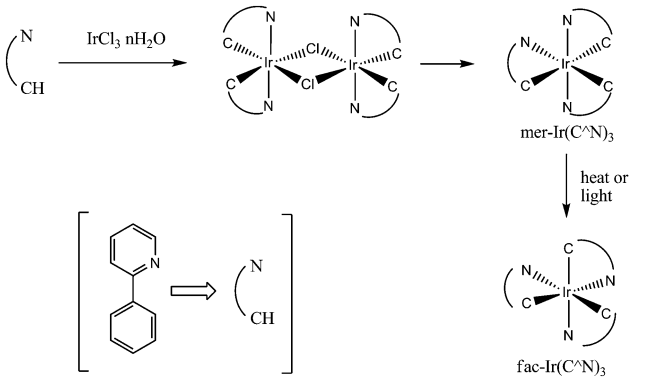

Fig. 8 Synthesis and structure of the homoleptic cyclometalated Ir(III) complexes.

For the homoleptic Ir(III) complexes two geometric isomers do exist known as *mer*- and *fac*-isomers. The *mer*-isomer corresponds to the meridional *N*,*N*-*trans* configuration, whereas the *fac*-isomer corresponds to the facial *N*,*N*-*cis* isomer. As can be seen from Fig. 8, the kinetic product, *mer*-isomer, can be transformed into the more stable *fac*-isomer under the influence of heat or light.[70] Practically, heteroleptic Ir(III) complexes lack isomers since the *N*,*N*-*trans* configuration prevails. Their synthesis proceeds in mild conditions enabling the use of a variety of ligand patterns.

Heteroleptic Ir(III) complexes can exist in the anionic, neutral and cationic forms depending on the nature of the third ligand (Fig. 9). All C^N ligands in Fig. 9 are anionic, where the C–H bond is removed by the dissociative reduction. Those commonly used in OLED device complexes are neutral and are based on 2-phenylpyridine (ppy) anionic derivatives (Fig. 9). While the ppy ligands are structurally similar to bipyridines, it was earlier recognized that the metal–carbon bonds which they form with transition-metal ions provide a specific influence on the properties of their complexes which are distinct from those of the *N*-coordinated bpy analogues.[73] Replacing bpy in $[Ir(bpy)_3]^{3+}$ by 2-phenylpyridine produces a very strong photoreductant, $[Ir(ppy)_3]$. The enhanced photoreducing potential of such complexes is attributed to the increase of electron density around the metal due to the strong donor character of the coordinating carbon atoms. The species containing both bpy and ppy, such as $[Ir(ppy)_2bpy]^+$, have intermediate photoredox properties and can operate as either a photo-oxidant or a photoreductant.[73]

The search for OEL materials was initiated by the classic $[Ru(bpy)_2]^{3+}$ example, which was used as a photocatalyst in solar-driven photoconversion processes.[67,73,79] The first task was to alter the excited state redox potential of similar metal complexes by several modifications: changing the central transition-metal; replacing some of the ligands; and modifying the ligands by adding suitable functional groups. For example, changing the metal center in $[Ru(bpy)_3]^{2+}$ to Ir(III) produces a complex $[Ir(bpy)_3]^{3+}$ with excellent photo-oxidizing power.[73] This change of the Ru(II) ion to a more stable third-row transition-metal ion Ir(III) provides improvement of the chromophore stability.

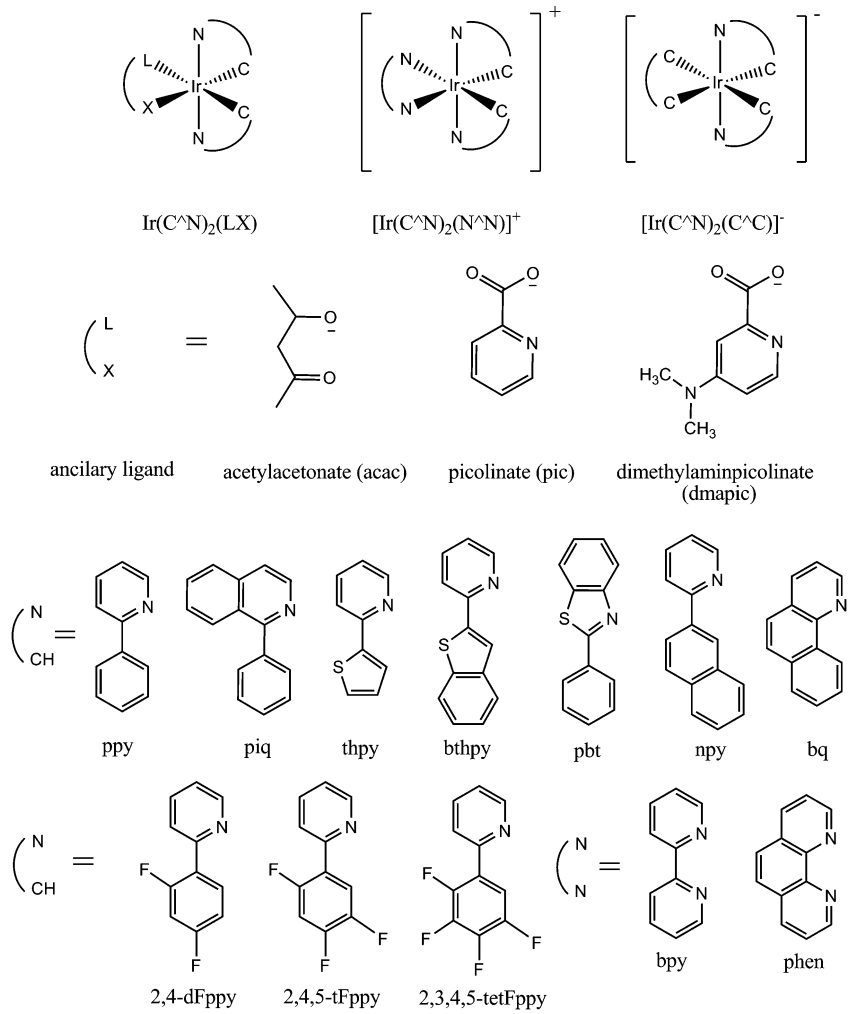

Fig. 9 Structure and notations of heteroleptic cyclometalated Ir(III) complexes (ppy = 2-phenylpyridine, piq = 1-phenylisoquinoline, thpy = 2-(thiophen-2-yl)-pyridine, bthpy = 2-(benzo[*b*]thiophen-2-yl)pyridine, pbt = 2-phenylbenzo[*d*]thiazole, npy = 2-(naphthalen-2-yl)pyridine, bq = benzo[*h*]quinoline, 2,4-dFppy = 2-(2,4-difluorophenyl)pyridine, 2,4,5-tFppy = 2-(2,4,5-trifluorophenyl)pyridine, 2,3,4,5-tetFppy = 2-(2,3,4,5-tetrafluorophenyl)pyridine, bpy = 2,2′-bipyridine, phen = 1,10-phenanthroline).

Besides homoleptic complexes with neutral ligands, we will concentrate attention on the cyclometalated Ir(III) complexes obtained by the Nonoyama reaction[70] (Fig. 8). In the past decade such Ir(III) cyclometalated photocatalytic complexes (Fig. 9) have started a new life as OEL materials in solid-state organic light emitting diodes (OLED)[31–35] and large-area flexible displays.[76,81]

The computational methodology used for the calculation of phosphorescence parameters of Ir(III) complexes typically involves the following steps: the molecular structure of the studied Ir(III) complexes are optimized at the singlet ground state and first excited triplet state without symmetry constraints. This is typically done at the DFT level using hybrid exchange–correlation functionals[99] and basis sets of the Lanl2DZ type[100] with the Gaussian 03 program.[101] For the calculations of excitation energies and transition dipole moments other basis sets for the light elements are used, like 6-31G(d),[102] and the ECP basis sets[103] for the Ir ion. Phosphorescence lifetimes and SOC calculations have usually been performed with the Dalton program.[104]

Transition metals, like iridium, participate in the coordination chemical bonding in such a way that 5d and 5d orbitals are still almost degenerate and the orbital angular momentum at the metal center is not quenched completely. Involvement of such heavy atoms into metal-to-ligand charge-transfer (MLCT) states of different symmetry increases the configuration interaction between them and the $\pi\pi^*$ states of the ligands, which lead finally to a strong singlet–triplet SOC mixing in the cyclometalated Ir complexes. This leads to the weakening of spin-selection rules and strong $T_1 \rightarrow S_0$ phosphorescence from triplet excitons can occur in such organometallic conjugated chromophores.

Incorporation of $Ir(ppy)_3$ into a polymer leads to an attractive EL material for two reasons: the high rate of electron–hole recombination on the $Ir(ppy)_3$ dye and relatively strong SOC at the transition-metal center involved into T–S mixing of the whole compound. This SOC induces a highly competitive $T_1 \rightarrow S_0$ transition probability of the MLCT type and large quantum efficiency of the OLED. At the same time the green color of $Ir(ppy)_3$ phosphorescence (514 nm) is well suited for use

in full color displays. The color can be tunable by applied magnetic fields[87] and also by chemical modification.[67,68,73,81,88,89]

The neutral iridium-cyclometalated complexes of the $Ir(ppy)_3$ type provide up to 19% external quantum efficiencies in OLEDs.[68] These phosphorescent materials have some intrinsic disadvantages, such as saturation of emission sites due to a long lifetime as well as triplet–triplet annihilation and concentration quenching arising from strong bimolecular interaction at high doping levels.[33,83] The use of the neutral iridium-cyclometalated complexes in OLEDs requires a complicated multilayer structure for efficient charge injection and for their transport in order to obtain light emission.[68,83]

The use of ionic cyclometalated complexes is much more profitable.[67,68] Ionic systems like $[Ir(bpy)_3]^{3+}([PF_6]^-)_3$ do not need complicated fabrication of multilayer devices for charge injection and recombination. They are used now in light-emitting electrochemical cell (LECs), which are promising for large-area lighting applications.[67,68,90] Just single-layers of such ionic complexes operate at a low voltage and these LECs have been shown to be rather insensitive to the choice of electrode material, allowing the use of air-stable anodes and cathodes.[67] What makes such ionic materials so different from the neutral organic semiconductors typically used in OLEDs? This is the presence of mobile ions $[Ir(bpy)_3]^{2+}$, which carry a 2+ net positive charge, and two negative counter-ions $[PF_6]^-$. Upon application of a bias, the anions and cations move toward the anode and cathode, respectively, creating high electric fields at the electrode interfaces which enhance charge injection into the polymer layer of the LEC and exciton formation at transition-metal complexes.[91] Holes and electrons are injected at a bias just exceeding the potential to overcome the HOMO–LUMO energy gap in the active material of LEC, irrespective of the energy levels of the electrodes.[67,81,91] The majority of ionic complexes used in these single-layer LEC devices have been ruthenium-based chromophores until very recent times.[67,81,88,89,91] They emit light in the orange–red region 600–650 nm, while for display and other LEC applications white light is needed. This can be obtained by mixing blue with red and green colors. Thus tuning the color to achieve green and blue emission is an important task for the synthesis of new ionic chromophores.

Such systems have been obtained recently in a form of mixed ligand cationic iridium complexes.[67,68] Usually they show low quantum yield compared to the tris-orthometallated Ir complexes.[67,73] An exception is represented by the recently reported green–blue emitting [Ir(2-phenylpyridine)$_2$(4,4′-dimethyl amino-2,2′-bipyridine)](PF_6) complex, labeled as N926, which shows an unprecedented phosphorescence quantum yield of 80% in dichloromethane solution at 298 K (ref. 68) and by the [Ir(2,4-difluorophenylpyridine)$_2$(4,4′-dimethyl amino-2,2′-bipyridine)](PF_6) complex, labeled as N969, which shows an even larger quantum yield of 85%.[68]

The first principles theoretical analysis of the phosphorescence of organometallic compounds has recently become a realistic task with the use of the above reviewed quadratic response (QR) technique in the framework of the time-dependent DFT approach.[51,61,92] We present connections between main features of electronic structures and photo-physical properties including phosphorescence efficiency and energy transfer mechanisms. The SOC effects and the $T_1 \rightarrow S_0$ transition in the $[Ir(ppy)_2(bpy)]^{3+}$, $[Ir(ppy)_3]$ and $[Ir(bpy)_3]^{3+}$ complexes are presented first in order to interpret the high efficiency of the corresponding LEC materials.

8. Phosphorescence of Ir(III) compounds

8.1. Phosphorescence of $[Ir(bpy)_3]^{3+}$

We first consider the cationic $[Ir(bpy)_3]^{3+}$ complex that uses only neutral ligands and that represents an ancestor key species in the genesis of spectral properties in the whole series of Ir(III) compounds.[59] Its phosphorescence has been studied in a mixed EtOH:MeOH glass at 4.2 K (ref. 105) and interpreted as an emission from the triplet state of the bpy ligand being of the ligand-centered $^3\pi\pi^*$ character.[105,106] A comparative study of the tentative ''dual emission'' in the series $[Ir(bpy)_x(phen)_{3-x}]^{3+}$, where phen = 1,10-phenanthroline (Fig. 9) and x = 0–3, indicates that the phosphorescence is not consistent with the ''dual emitter'' concept, but is accounted for by a simple model in which the $^3\pi\pi^*$ state on the phen ligand is in thermal equilibrium with the $^3\pi\pi^*$ state of the bpy ligand at higher (70 cm^{-1}) energy.[105] The influence of the inhomogeneous environment on phosphorescence and zero-field splitting is well known.[105,107–111] The ''dual emission'' characteristics of the x = 2 and x = 1 systems are explained by an independent spread of the ligand-centered $^3\pi\pi^*$ state energies.[105] This analysis is consistent with the line widths, with small shifts in the peak maximum and with the idea that an excitation resides on a single ligand at 4.2 K.[105] Thus after relaxation at the triplet state the electron distribution localizes at one of the ligands, which then moves closer to the iridium ion. This is in good agreement with the phosphorescence spectrum of $[Ir(bpy)_3]^{3+}$ which was interpreted as an emission from the triplet state of one bpy ligand being of the ligand-centered $^3\pi\pi^*$ character.[105,106] Because of this the calculated phosphorescence lifetime of the $[Ir(bpy)_3]^{3+}$ complex is comparatively long (Table 4). Nozaki *et al.*[106] have previously simulated the phosphorescence spectra of a number of tris(2,2′-bipyridine) transition metal compounds without calculation of the S–T transition moments, but taking into account Huang–Rhys factors (S) and some additional fitting parameters. Their simulation of the low-resolution observed spectra of the Ir(III) compound[106]

Table 4 Radiative phosphorescence lifetimes (μs) and energies of $S_0 \rightarrow T_1$ for Ir(III) complexes calculated with QR TD DFT/B3LYP method. Based on ref. 63

Complex	ΔE (S → T)	ΔE (S → T)$_{exp}$	τ_x	τ_y	τ_z	τ	τ_{exp}
$[Ir(bpy)_3]^{3+}$	2.70	2.75	58.3	195.0	158.29	104.9	54
$[Ir(ppy)_3]$	2.52	2.42	1.3	1.3	82.7	2.0	2.0
$[Ir(ppy)_2(bpy)]^+$	2.23	2.25	14.3	1.6	162.8	4.8	4.4
$[Ir(ppy)_2(dtb\text{-}bpy)]PF_6$	2.14	2.13	14.5	1.6	111.2	4.8	2.3

indicates that a large part of the intense red wing is determined by overtones and combination bands. The calculated S factors are not large ($S \sim 0.3$) in agreement with the intensity ratio between vibrational satellites and zero-phonon bands.[106,112] Our calculations[63] of the phosphorescence lifetime (Table 4) and qualitative analysis of vibrational spectra in both S_0 and T_1 states agree with the results of ref. 105, 106 and 112. The long-lived triplet spin-sublevel (T^z, Table 4) is enhanced by spin–vibronic perturbation (with the vibrational mode at 1025 cm^{-1}) and its intensity is determined by the first term in eqn (59). This and other active modes are connected with vibrations in the bpy ligand. This is in agreement with the analysis presented in ref. 106 and 112 and supports the assignment of the relaxed T_1 state as a local $^3(\pi\pi^*)$ excitation.

The zero-field splitting (ZFS) parameters for the phosphorescent state of the $[Ir(bpy)_3]^{3+}$ complex calculated at D_3 symmetry of the S_0 state geometry are very small (about 0.3 cm^{-1}) and are typical for organic $^3(\pi\pi^*)$ phosphorescence.[4] The reason is that three lowest triplet states, $^3A_2$ and ^3E, which provide the main second-order SOC contribution to the ZFS parameters (because they are almost degenerate and have very small ΔE denominator) all have $^3(\pi\pi^*)$ nature. There is no efficient SOC between such states and the ZFS is therefore determined mostly by spin–spin coupling.[108] For the lower C_2 symmetry the SOC contribution would be even smaller, because of the increased splitting of the $^3A_2$ and ^3E $^3(\pi\pi^*)$ states. The phosphorescence decay of the $[Ir(bpy)_3]^{3+}$ complex is non-exponential at 4 K, but becomes almost single exponential at 77 K.[105] This is due to the lack of thermal equilibrium between spin sublevels, which are split by $\sim$0.1 cm^{-1} ZFS. Each triplet sublevel has a quite different decay rate (Table 4), which in turn is faster than the spin–lattice relaxation rate at 4 K.[105] When a strong magnetic field (5 T) is applied, the ZFS spin sublevels get mixed in a polycrystalline sample and a larger degree of thermal equilibrium between the spin sublevels is established, even at 1.5 K. This results in a nearly exponential decay profile.[105] The radiative decay lifetimes calculated for a symmetric structure (Table 4) are equivalent for two short-lived sublevels (τ_x, τ_y). They should be slightly distorted at the lower C_2 symmetry,[61] which agrees with the decay measurements at different temperatures in ethanol–methanol glasses.[105] Rather different behavior is predicted for the mixed complexes as discussed below.

8.2. Phosphorescence of mixed Ir(III) complexes

The $[Ir(ppy)_2(bpy)]^+$ complex belongs to the C_2 point group. The T_1 state is determined explicitly by the HOMO–LUMO excitation. The plots of these molecular orbitals tell us that the $S_0 \rightarrow T_1$ transition constitutes a metal-to-ligand charge transfer (MLCT) from the 5d metal orbital to the bpy ligands with additional small CT between two ppy and bpy ligands (in contrast to pure $^3\pi\pi^*$ intraligand $S_0 \rightarrow T_1$ transition for the $[Ir(bpy)_3]^{3+}$ complex). The LUMO is localized on the bpy ligand and has a strong bonding character with respect to the C–C bridge, as usual. That is why the C–C bridge bond in the bpy ligands becomes stronger upon HOMO–LUMO excitation. The bond distance shortened from 1.483 to 1.429 A. This is the most dramatic structural change upon excitation (like in the previous case). The first $S_0 \rightarrow S_1$ absorption band is predicted to be very weak ($f = 0.0003$) and only 0.03 eV higher in energy than the $S_0 \rightarrow T_1$ vertical transition. This is a typical S–T splitting for all studied mixed-ligand cationic complexes, but not for the tris-complexes of the $[Ir(ppy)_3]$ and $[Ir(bpy)_3]^{3+}$ type, which have higher S–T splitting in the order of 0.2–0.8 eV.[61] The S_1 state corresponds to the same HOMO–LUMO excitation as the T_1 state does. The S–T splitting is very small because the HOMO and LUMO are localized at different moieties of the complex, which also supports the ligand-to-ligand LLCT nature of the S_1 and T_1 states.

At room temperature in fluid solvents an emission maximum of $[Ir(ppy)_2(bpy)]^+$ is observed at 595 nm, but in the solid glass (77 K) a structured emission in the range 527–550 nm is detected.[73] The emission lifetime ranges from 4.4 to 5.2 μs at 77 K. Our QR TD DFT calculations with SDD basis for the Ir atom (and 6-31G(d) for other light atoms) provide a good interpretation of the $[Ir(ppy)_2(bpy)]^+$ complex phosphorescence (Table 4).

Substitution of hydrogen atoms in the *para*-position to the Ir–N bonds in the bpy ligands by *tert*-butyl groups provides small but noticeable changes in the electronic structure of the chromophore. Such a substituted system, or [Ir(2-phenylpyridine)$_2$-(4,4′-*tert*-butyl-2,2′-bipyridine)](PF_6) complex in the following called $[Ir(ppy)_2(dtb\text{-}bpy)]PF_6$, is very similar to the previous $[Ir(ppy)_2(bpy)^+]$ molecule. This ionic complex was synthesized in an attempt to create a better OEL chromophore compared to the popular $[Ru(bpy)_3]^{2+}$ charge carrier in single-layer LEC devices.[67] Changing the metal center to the more stable Ir ion not only improves the stability of the complex, but also increases the ligand field splitting in comparison with the tris-orthometallated $[Ru(bpy)_3]^{2+}$ $[Rh(bpy)_3]^{3+}$ complexes.

The T_1 state of $[Ir(ppy)_2(dtb\text{-}bpy)]PF_6$ has ^3B symmetry: the adiabatic $S_0 \rightarrow T_1$ excitation energy is equal to 2.23 eV (Table 4), which corresponds to the 0–0 band wave-length, 555 nm, neglecting the difference in the zero vibrational energies. The observed maximum of the emission band of the Ir(ppy)$_2$-(dtb-bpy)PF_6 complex in dichloromethane at 298 K is at 581 nm.[67] The red shift can be explained by vibronic 0–1 bands which occur because of excitation of different vibrational modes in the ground state. We have calculated the Huang–Rhys factors for a number of important modes from the finger-print IR region by the mass-weighted displacement vector and the gradients.[51,98] The most active modes are 1052, 1059, 1330, 1511, 1569 and 1612 cm^{-1}. We neglect the changes in vibrational frequency and mixing of modes. An account of these modes with approximation of the vibronic line-shape by Gaussian bands of the 500 cm^{-1} band width at a half-maximum provides a total red shift of the emission band of 0.13 eV and a maximum at 590 nm. Thus only an FC analysis, the first term in eqn (59), can explain the red shift of the wide maximum in the low-resolution emission spectrum.[67] As follows from Table 4, the calculated phosphorescence lifetime for the termalized triplet state (4.76 μs) is in a reasonable agreement with a value of 2.32 μs, calculated from the radiative rate constant $k_r = 4.31 \times 10^5$ s^{-1} (ref. 90) (high temperature limit in deaerated solution). The most

active spin sublevel T^y (τ_y = 1.6 μs) emits light with z-polarization (along main axis); the calculated T → S transition moment is equal to 0.244 ea_0, being comparable to the weak allowed S → S transitions. In a low-temperature solid state the phosphorescence of the compound N925 should be strongly nonexponential.

The mixed-ligand cationic iridium complexes, considered above, exhibit lower quantum yields of phosphorescence in comparison with the tris-orthometalated complexes of the [Ir(ppy)$_3$] type. Now we need to consider the reason for this difference.

8.3. Phosphorescence of [Ir(ppy)$_3$]

The ground state of [Ir(ppy)$_3$] has C_3 symmetry (with the main z-axis).[61] In fact the ppy in common notations, like [Ir(ppy)$_3$], is not phenylpyridine: it is the phenylpyridinate anion, where the proton in the 2′ position of the phenyl ring is removed. Vertical excitation energies (eV) for the first six states of [Ir(ppy)$_3$] from TD DFT calculations of ref. 61 are equal to: 2.51 (^{3}A), 2.52 (^{3}E), 2.71 (^{1}A) and 2.77 (^{1}E). This group of states is connected with MLCT transitions and simultaneous ππ* excitations inside the ligands.[59,110]

The lowest T_1 state has two degenerate neighbors; these are higher ^{3}E states being extremely close in energy and which provide relatively large SOC contributions to ZFS. The lowest spin sublevel is T^z at both optimized S_0 and T_1 state geometries, which is almost dark (Table 4). The higher lying singlet states ^{1}E at 3 eV, which have almost pure MLCT character, produce the largest contributions to SOC mixing with the phosphorescent triplet and to the $T_1 \rightarrow S_0$ transition probability. Like in the cationic Ir complex with the bpy ligands, the large structural changes are obtained upon S_0–T_1 excitation only in one ligand: the C–C link between phenyl and pyridine rings in this ligand is shortened by 0.05 A.

The Ir–C and Ir–N asymmetric displacements in the excited ligand (ppy)* are the most important vibrational modes for vibronic activity in phosphorescence. These bonds are shortened by 0.035 A upon the $S_0 \rightarrow T_1$ transition (Table 4). A potential energy surface cross section along this vibrational mode indicates a big change in the force constant for the ground and excited states.[61]

Thus the phosphorescence from the lowest vibrational level at low temperature (1.4 K) should be very broad as it is detected in experiment (half width of about 3000 cm^{-1} in solid THF solvent[87]). The large displacements in the equilibrium positions for a number of local modes induce the red shifted and broadened maximum of the $T_1 \rightarrow S_0$ phosphorescent transition.

The electronic $S_0 \rightarrow T_1$ transition dipole moment is a strong function of the displacement since the phosphorescence lifetimes for the spin sublevels presented in ref. 61 indicate rather strong differences for two geometrical structures. The S_0-optimized geometry with C_3 symmetry emission from the T^x and T^y sublevels of the lowest ^{3}A state provides y and x polarization with an equally short radiative lifetime (Table 4). The T^z sublevel is almost dark in a pure electronic $T^z \rightarrow S_0$ transition. Thus at thermal equilibrium (high temperature limit at $T \geq 77$ K) the lowest triplet state will be depleted through emission from the T^x and T^y sublevels.[61]

The $T_1 \rightarrow S_0$ transition was assigned as MLCT. In fact the HOMO "metal" orbital has only 50% of Ir($5d_\pi$) character with the reminder of the orbital being localized at the π-AOs of the ligands; mostly at the phenyl parts of all three ppy ligands. The LUMO orbital has no metal contribution and includes the fully delocalized π-MO of all ligands. The SOC matrix element $\langle S_0|H_{SO}|T_1\rangle$, which is responsible for the nonradiative quenching of the triplet state, includes only the HOMO–LUMO SOC integral. Thus it has no SOC contribution from the metal and should be negligible.[61,80] It means a minor intrinsic quenching of the triplet state and high quantum yield of phosphorescence. The large contribution to the HOMO "metal" orbital is enough to produce very strong SOC mixing with high energy ^{1}E states of pure MLCT character, which include Ir($5d_\sigma$) orbital excitation. This explains the strong radiative power of the $T_1 \rightarrow S_0$ transition.

In fact, the T^x and T^y sublevels presented in ref. 59 and 61–63 do not correspond to the ZFS axes. The former frame was chosen by the structure obtained at the optimized ground state which is close to C_3 symmetry.[61,63] The ZFS sublevel energies were estimated separately by variational treatment of the SOC matrix calculated for 40 substates (the 10 lowest singlet and triplet states obtained by TDDFT method).[61] The lowest state was obtained as the T^z sublevel with energy 19 989 cm^{-1} (with respect to the ground state), the next two sublevels were found at 33 and 104 cm^{-1} higher energies at the ground state geometry,[61] but their wavefunctions and lifetimes were not analyzed. The reason for this was connected with the fact that the composition of the substrate mixture and the energies strongly depend on the choice of the starting geometry. The calculated lowest triplet sublevel was in good agreement with observation in THF matrix[87] for energy and lifetime. The averaged phosphorescence decay time of 2.1 μs[87] also agrees with our prediction.[61] The structure and energy of the upper sublevels are dependent on the pseudo Jahn–Teller effect; thus their exact assignment can be properly analyzed only by account of SOC and vibronic mixing. Sophisticated calculations by Koseki *et al.*[96,113] with an MCSCF + SOCI approach indicate an importance of the Jahn–Teller effect on the lowest ^{3}E state of the [Ir(ppy)$_3$] dye. All calculations with variational treatment of the ZFS problem in a large T and S environment[61,80,96] predict a large number of close-lying substates and interpretation of the [Ir(ppy)$_3$] phosphorescence therefore become complicated and uncertain.

Analyses of the old results with the above-described splitting of spin sublevels[61] predict that the upper triplet substrate (T^{III}) has a large contribution from the singlet S_4 and S_5 states, which provides the most active radiative decay. The ZFS for the two other sublevels is determined more by T–T spin states mixing. Thus, these substates have much lower decay rates.

8.4. Phosphorescence of phenylisoquinoline containing Ir(III) complexes

The C^N cyclometalated complexes of the Ir(III) ion, such as the green phosphorescent *fac*-[Ir(ppy)$_3$] and red emissive *fac*-[Ir(piq)$_3$],

are now well known as phosphor emitters in OLED applications.[114] Such devices doped with Ir complexes exhibit external quantum efficiency in the range of 20–29% with no optical outcoupling enhancements. According to the high quantum yield and short lifetime of phosphorescence in the cyclometalated Ir(III) complexes and the corresponding OLED applications there have been detailed studies of their photophysical characteristics including heteroleptic Ir dyes and cationic species with bipyridine ligands.[59]

It is interesting to calculate the relative set of complexes of the intermediate type $[Ir(piq)_x(ppy)_{3-x}]$ where x = 1–3 (Fig. 10) in order to scrutinize their photophysics in solutions and their electroluminescence performance in OLEDs.[64,114] The oxidation potential of the parent homoleptic complexes are almost identical;[114] thus the presence of the ppy ligands in the heteroleptic dyes cannot alter the degree of the metal 5d orbitals admixture in the HOMO–LUMO character (these are the orbitals involved in phosphorescence mostly based on piq ligands[64]), since the donor properties of the two organic species are nearly the same.[64,114] In fact the HOMO energies of the series including the *fac*-$[Ir(ppy)_3]$ dyes are nearly identical.[64]

It was also assumed at the beginning of the experimental project of Deaton *et al.*,[114] that the phosphorescence of the systems $[Ir(piq)_x(ppy)_{3-x}]$ (x = 1–3) originates from the piq ligands because of the lower T_1 state energy than that of the ppy ligand. This assumption is based on comparison of the phosphorescence data and is supported by TD DFT QR calculations[64] in those parts that the LUMOs are really localized mostly on piq ligands; the LUMO energy falls down drastically going from $[Ir(ppy)_3]$ to the first dye with a new piq ligand $[Ir(piq)(ppy)_2]$.[64] Therefore, the above series of dyes can provide a comparison of the effects upon photophysical properties of having one, two, or three emissive piq ligands without being confounded by effects from the differences in electron-donating between the radiatively passive (ppy) species and the active piq ligands.[114]

In ref. 64 the experimental results of Deaton *et al.*[114] have been interpreted on the ground of TD DFT calculations with account of quadratic response for the phosphorescence rate constant.

A series of *fac*-$[Ir(piq)_x(ppy)_{3-x}]$ complexes were studied[114] for comparison with the parent *fac*-$[Ir(ppy)_3]$ dye in order to reveal the position effects of placing emissive ligands in various coordination structures. All species were optimized with different DFT functional and basis sets[64] giving a similar quality of comparison with the X-ray experimental data. The Ir–C_{ppy} bond lengths are optimized to be longer (2.02–2.023 Å) than the Ir–C_{piq} bonds (2.014–2.017 Å) in agreement with experiment.[114] From x = 1 to x = 2 the Ir–C_2 and Ir–N_2 bonds are both significantly shortened, while the Ir–C_3 and Ir–N_1 are slightly elongated. Large structural changes occur upon the transition from x = 2 to x = 3. The Ir–C_3 and Ir–N_1 bonds are shortened by 0.007 and 0.005 Å, respectively, while Ir–N_2 is slightly elongated by 0.003 Å.

The spectral properties of the series have been calculated by theh TD DFT QR method with the PBE0 functional and the mixed basis sets, D95 and SDD (Stuttgart effective core potential basis for Ir).[103,115] The singlet–singlet absorption spectra consist of the visible bands system (400–500 nm) of increasing intensity (going from x = 1 to x = 3) and also of the intense UV system (starting from 370 nm in experiment[114]). The UV band system is predicted in the range 370–300 nm, though the experimental measurements are limited to long wavelength (350 nm). The solvent effect of tetrahydrofuran used in experiment is simulated by the polarized continuum model.[116]

The presence of an increasing number of the piq ligands results in a substantial enhancement of the absorption intensity in the whole spectrum. In the visible part of the experimental spectra a number of overlapping bands are seen[114] which are completely reproduced by the TD DFT QR calculations including a weak $S_0 \rightarrow T_1$ absorption at about 600 nm. The first $S_0 \rightarrow S_1$ transitions at 475 nm are very weak in agreement with experiment. These are HOMO → LUMO excitations of the MLCT character with a very small contribution of the intraligand (piq) and interligand transitions (Fig. 11).[64]

The HOMO represents mostly the Ir $5d_{z^2}$ AO with small admixtures from all ligands, while the LUMO is localized on piq ligands with a small decreasing admixture of the $5d_{xy}$ AO. The most intense bands in the visible range also have MLCT character but with larger contributions from the intraligand ππ* excitations. The relative absorption intensity of these bands

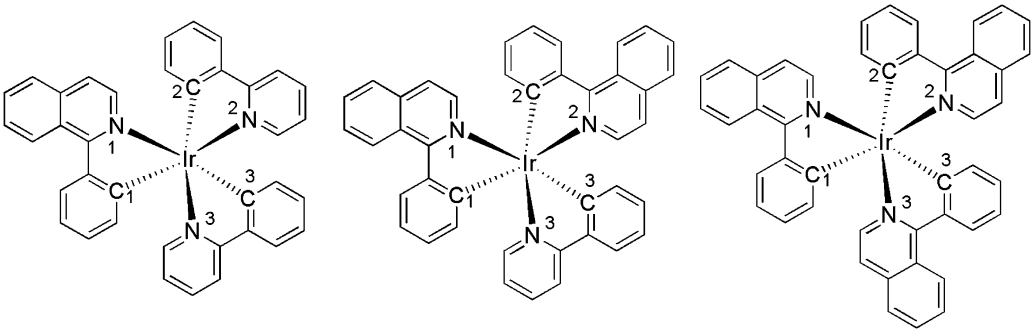

Fig. 10 Series of the *fac*-$[Ir(piq)_x(ppy)_{3-x}]$ complexes (x = 1, a; x = 2, b; x = 3, c). Reprinted with permission from ref. 64. Copyright 2011 American Chemical Society.

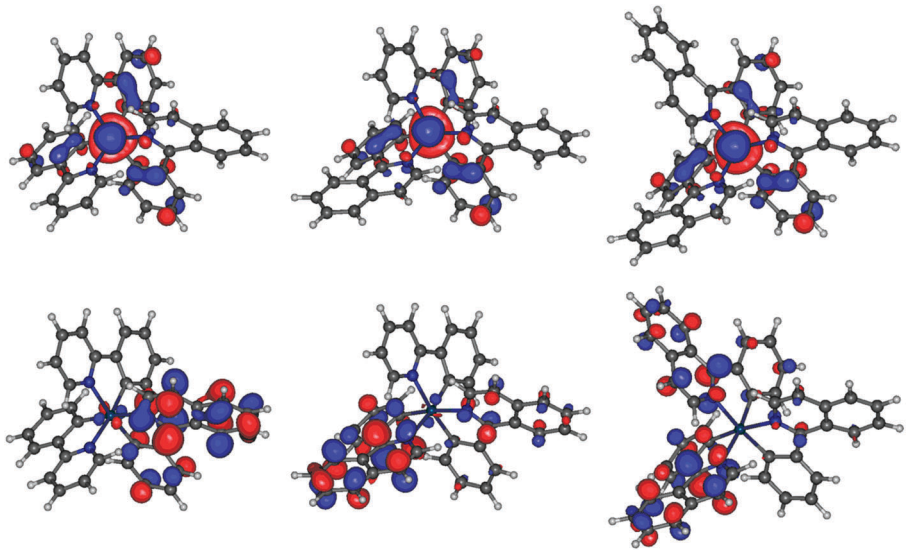

Fig. 11 Calculated HOMOs (top) and LUMOs (bottom) of the *fac*-[Ir(piq)$_x$(ppy)$_{3-x}$] complexes (x = 1, 2, and 3 from left to right). Reprinted with permission from ref. 64. Copyright 2011 American Chemical Society.

follows the order *fac*-[Ir(piq)(ppy)$_2$] < *fac*-[Ir(piq)$_2$(ppy)] < *fac*-[Ir(piq)$_3$], their wavelengths and the standard molar absorptivities are qualitatively reproduced.[64,114] In the 440–420 nm region the calculations predict that there are three dominant electronic transitions (with oscillator strength close to 0.1) for *fac*-[Ir(piq)$_3$], two for *fac*-[Ir(piq)$_2$(ppy)] and one for *fac*-[Ir(piq)(ppy)$_2$], leading to the increase of absorption intensity with increasing x number. Thus, the additivity of absorption from several ligands explains the observed trend.

In accordance with the QR TD DFT approach the radiative rate constants, $k_{r,calc}$ are calculated and compared with room temperature measurements as shown in Table 5, where all values correspond to the high-temperature limit of k_r. The numbers are to be compared with experimental radiative rate constants obtained from the lifetime and quantum yield: $k_{r,expt} = \Phi_{em}/\tau_0$ where Φ_{em} is the photoluminescence quantum yield and τ_{obs} is the observed emission decay time measured in 2-methyl-tetrahydrofuran (2-MeTHF) at 293 K.[114] The radiative lifetimes of phosphorescence are also shown. Overall, the accuracy and reliability of the theoretical computations are quite satisfactory.

Deaton *et al.*[114] have also measured emission decay in doped PMMA matrices at various temperatures from 295 down to 2 K. The decay rates of the individual sublevels of the T_1 state and their ZFS energies have been extracted from the temperature dependence, as it is usually performed in studies of Yersin *et al.*[34,35,87] The highest spin sublevel demonstrates the most prompt decay: $k_{III} = 2.37 \times 10^6$ s^{-1} for *fac*-[Ir(piq)$_3$]. There is no contradiction with results presented in Table 5. The average lifetime is still close to 1.26 μs for this dye in PMMA, since it is about three times larger than the individual radiative lifetime of the prompt sublevel T^{III}. This is a typical result for Ir dyes, when two other spin sublevels demonstrate much slower decay. In ref. 64 the ZFS parameters were though not calculated. From our experience with other Ir dyes we can easily transform the results of the SOC calculations in ref. 64 and confirm qualitatively the spinlevel selectivity obtained by Deaton *et al.*[114] for the PMMA matrix.

The k_r values are nicely reproduced for *fac*-[Ir(ppy)$_3$], *fac*-[Ir(piq)$_2$(ppy)] and *fac*-[Ir(piq)$_3$], indicating a promising use of density functional theory calculations in phosphorescence intensity studies of iridium complexes. In all our works we have calculated the electronic parameters of the T → S transition moment in terms of perturbation theory at the vertical geometry, and all perturbing states are fixed at the S_0 geometry, since the transition ends in the S_0 state and its vibrations determine the vibronic parameters of the emission. In fact, calculations at the T_1 geometry are not as successful. They suggest that the electronic T → S transition moment decreases as the geometry of the molecule is changed from S_0 to T_1, and

Table 5 Phosphorescence emission energies and radiative rate constants calculated at the ground state geometry using B3LYP TDDFT linear and quadratic response theory in comparison with experimental data. Based on ref. 64

Complex	ΔE(S–T)$_{expt}$/eV	$\Delta E_{S-T,calc}$/eV	$k_{r,expt}$/s^{-1}	$k_{r,calc}$/s^{-1}	Φ_{em}	τ_{obs}/μs
fac-[Ir(ppy)$_3$]	2.40[a]	2.48	6.4×10^5 [a]	6.1×10^5	0.9	1.3
fac-[Ir(piq)(ppy)$_2$]	1.97[b]	2.05	2.9×10^5 [b]	2.2×10^5	0.4[b]	1.38[b]
fac-[Ir(piq)$_2$(ppy)]	1.98[b]	1.99	2.7×10^5 [b]	2.7×10^5	0.37[b]	1.39[b]
fac-[Ir(piq)$_3$]	1.99[b]	1.99	3.6×10^5 [b]	3.5×10^5	0.45[b]	1.25[b]

[a] In degassed CH_2Cl_2 at room temperature.[117] [b] In 2-MeTHF at 293 K.[114]

that the energy of the vertical $T_1 \rightarrow S_0$ transition is much smaller (as it is expected accounting for the preference in elongation of numerous bonds). Just because of the smaller E_{ST} gap and its third power dependence, the computed lifetime τ would be unreasonably large at the T_1 geometry. One should also note that at room temperature the phosphorescence band is wide and structureless; both 0–0 and other vibronic transitions contribute to this band. In the case of Ir dyes with their low symmetry, the pure electronic T–S transitions are allowed with SOC account and the vertical $S_0 \rightarrow T_1$ band corresponds to the most intense peak in the emission spectrum. Thus, it is used in our calculation to obtain the radiative rate constant k_r and the phosphorescence lifetime.

The experimental Stokes shift in the studied series of Ir dyes clearly indicates a relatively large distortion upon S–T transition, which is well reproduced by DFT geometry optimizations.[64] The final good results for the calculated phosphorescence wavelength and lifetime is probably a result of some error cancellation. In fact our TD DFT calculations underestimate to some extent the vertical $S_0 \rightarrow T_1$ excitation energy. Thus some better agreement is occasionally obtained in this approach for the calculated phosphorescence wavelength. Despite these details one has to stress that the agreement for the radiative phosphorescence lifetime between theory and experiment is much more impressive and reliable. The quadratic response method for the summation of a huge number of contributions in the estimation of the electric dipole T–S transition moment, is more relevant when it is implemented at the final S_0 ground state structure. SOC calculations presented in ref. 64 indicate that the non-radiative rate constants k_{nr} should diminish going from *fac*-[Ir(piq)$_2$(ppy)] to *fac*-[Ir(piq)$_3$] and the phosphorescence quantum yields should increase – a trend that is supported by experiment.[114] This is because the iridium d-orbital contribution to the LUMO becomes smaller as x increases from 2 to 3 in the *fac*-[Ir(piq)$_x$(ppy)$_{3-x}$] series, suggesting that the SOC matrix element between the ground singlet (S_0) and first excited triplet (T_1) states $\langle S_0|H_{SO}|T_1\rangle$ decreases, from 289 to 169 cm^{-1}.[64] The latter is reduced to the HOMO–LUMO single-electron SOC integral and strongly depends on the small d-orbital admixture of the LUMO.

8.5. Phosphorescence of heteroleptic Ir(III) complexes with various ancillary ligands

A number of theoretical phosphorescence studies of new cyclometalated heteroleptic Ir(III) complexes with SOC account have been published recently.[62–64,97] TD DFT QR calculations of the above-described approach have been presented for heteroleptic complexes with the picolinate (pic) ligand of the [Ir(ppy)$_2$(pic)] type in ref. 62. The main subject of that study was a comparison with amino-derivatives of the picolinate species. The phosphorescent, structural and electrochemical properties of [Ir(ppy)$_2$(pic)] and [Ir(ppy)$_2$(dmapic)] complexes (Fig. 9 and 12) were thus studied and compared.

The [bis(2-phenylpyridine)(2-carboxy-4-dimethylaminopyridine)] iridium(III) complex (denoted as N984)[68] has been reported to exhibit a relatively strong phosphorescence with high quantum

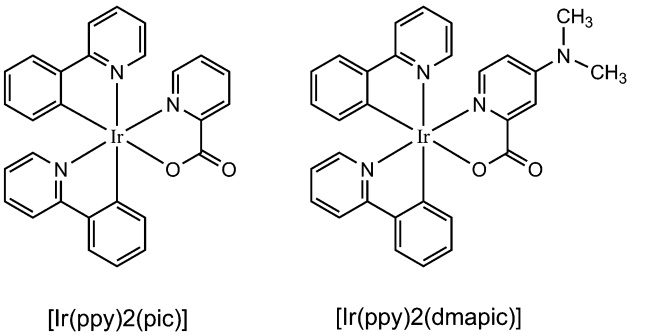

Fig. 12 Structure of cyclometalated [Ir(ppy)$_2$(pic)] and [Ir(ppy)$_2$(dmapic)] complexes.

yield in a PMMA matrix.[62,68] In contrast, the phosphorescence of the [Ir(ppy)$_2$(pic)] species is very weak.[68] The LUMO in this species is localized on the picolinate ligand, while in N984 both LUMO and LUMO + 1 are distributed on the ppy′ and ppy ligands, respectively. (The HOMOs are universally delocalized on Ir and ppy ligands in all heteroleptic cyclometalated Ir(III) complexes presented in Fig. 9.[9a,69,97,110]) In the N984 species the first excited triplet state represents the MLCT configuration with a large admixture of interligand (ppy)–(ppy)′ and intraligand excitations. The calculated averaged radiative lifetime of the N984 phosphorescence in the high-temperature limit is equal to 3.08 μs,[62] which is in a reasonable agreement with the measured lifetime (2.42 μs) for N984 dopant in a PMMA film.[68] In the [Ir(ppy)$_2$(pic)] species the nature of the T_1 state is rather different.[62,69] The charge transfer to both ppy and pic ligands are present; thus, the triplet state is more delocalized than in the N984 complex, where the ancillary pic ligand is not involved in the S_0–T_1 transition.[62] The introduction of the N(CH$_3$)$_2$ group in the picolinate moiety of the N984 species provides a strong shift of the LUMO level from the weakly bound pic ligand to the π^* MO at the tightly bound ppy′ ligand. By this introduction of the donor dimethylamino group into the pic moiety the N984 complex returns back to the wide family of bright phosphorescent Ir(III) dyes discussed in this chapter: a strong SOC-mixing between T and S states of the MLCT type with electron transfer from 5d$_\pi$ and 5d$_\sigma$ orbitals induced by exchange interaction with local excited $\pi\pi^*$ excitations in the ppy ligands is the general characteristic of their phosphorescence mechanism.[61–64] A fast ISC together with a short radiative lifetime of the microsecond scale (order of magnitude shorter than nonradiative quenching time) thus provide a strong phosphorescence in this group of Ir(III) dyes. The quantum yield of phosphorescence (Φ_p) of the [Ir(ppy)$_2$(pic)] complex is much lower (0.033) than Φ_p of the N984 dye (0.70) in similar solvents at room temperature[68] because of the above-mentioned deformation of the LUMO and the change of nature of the lowest triplet state orbital.[62]

8.6. Fluorinated organoiridium complexes for blue-phosphorescent OLEDs

Implementation of fluorine substituents into the cyclometalated ligands has been widely used in attempts to develop blue-phosphorescent dopants for emissive layers in white

OLEDs.[9,35,63,97,113] A series of Ir(III) complexes with fluorinated ppy ligands have been studied in ref. 63 and 97 with an account of the SOC effect on their phosphorescence. Xin Li *et al.*[63] calculated, by the TDDFT QR method, a series of three- and four-F atom substituted phenylpyridines in *fac*- and *mer*-isomers of homoleptic Ir(III) dyes, while Koseki *et al.*[97] studied various fluorinated homoleptic and heteroleptic Ir(III) complexes including pic and acac ancillary ligands. Introduction of two F atoms at the 2′ and 4′ positions of the ppy ligands in combination with the employment of picolinate as an ancillary ligand provides a very efficient blue-emitting bis-cyclometalated dye, the so-called FIrpic.[118] Koseki *et al.*[97] calculated SOC effects in this and similar complexes taking the FIrpic as the first target and discussed the substituent fluorine and ancillary ligand effects on stability and phosphorescence. They have shown that the use of two ancillary ligands is inappropriate for blue-phosphorescent dopants in OLEDs.

Xin Li *et al.*[63] considered in particular the phosphorescence radiative rate constants and lifetimes in the series of *fac*-[Ir(F3-ppy)$_3$], *fac*-[Ir(F4-ppy)$_3$], *mer*-[Ir(F3-ppy)$_3$], and *mer*-[Ir(F4-ppy)$_3$] complexes. In Fig. 9 these ligands are denoted as 2,4,5-tFppy and 2,3,4,5-tetFppy, respectively. The authors of ref. 63 explained why the green-emitting *fac*-[Ir(ppy)$_3$] becomes blue-emitting upon fluorination and showed that the meridional isomers are less efficient emitters; this is supported by experiment for the *mer*-[Ir(F4-ppy)$_3$] complex.[119] Like in other studied Ir(III) complexes[61–64] the MLCT phosphorescent transition is rather localized in one ligand, which moves closer to the Ir atom after relaxation in the T1 state.[63] Introduction of the fourth fluorine substituent into the ppy ligand leads to an increase of the phosphorescence radiative lifetime by destroying the balance of various T–T and S–S contributions in the T_1–S_0 transition moment, eqn (50). The calculated lifetimes for the *fac*-[Ir(F3-ppy)$_3$] and *fac*-[Ir(F4-ppy)$_3$] dyes are 2.7 and 3.2 μs,[63] which can be compared with the experimental results in butyronitrile glass at 77 K, 3.9 and 4.2 μs,[119] respectively.

The SOC matrix element between the T_1 and S_0 states was determined to be 100 and 500 cm^{-1} in the facial and meridional isomers of the [Ir(F3-ppy)$_3$] complex.[63] Accounting that the square of this matrix element determines the nonradiative quenching of phosphorescence the authors of ref. 63 explained the lower quantum yield of the meridional dye. The electrochemical and photophysical properties of this series of dyes studied in solvents and in the solid state[119] agree with the theoretical studies.[63] The fabricated OLEDs with doped PVK provide electro-generated blue luminescence (similar to that in solution); the stability and efficiency of the devices made with the studied series of homoleptic fluorinated Ir(III) dyes strongly depend on the stereochemistry of these complexes and the higher external quantum efficiency measured for the facial isomers.[119]

We must remind that the blue PhOLEDs are hard to fabricate (compared with the red and green ones) due to the big TS energy gap, which leads to insufficient carrier injection and exciton confinement.[54,113] Recently, the FIrpic compound could provide nearly 100% when doped into the wide energy gap host of *N*,*N*′-dicarbazolyl-3,5-benzene; such an electron transport material with high electron mobility as well as high triplet energy is needed to confine the T excitons and to improve the electron–hole recombination.[113]

Phosphorescent OLED devices based on Ir(III) complexes as highly efficient blue-emissive dopants have by now entered the market.[97,113] The color tuning method is widely applied to multicolor and white light OLED devices. Quadratic response DFT calculations assist the scrutiny of the details of spin–orbit coupling effects on singlet–triplet states mixing in the organo-iridium dyes. The required red–green–blue (RGB) primary color emitters[97] are firmly based on the structural platform of the [Ir(C^N)$_2$(L^X)] type of dyes (Fig. 9). The recent quantum chemical studies with SOC account[63,97] show that the selection of geometrical isomers is important to obtain brighter blue-color phosphorescence.

9. Some new approaches to increase the efficiency of OLEDs

A few alternative ways have recently been considered in order to compel triplet excitons to do useful work in pure organic materials.[28,35,55a] The general idea is to induce the reverse ISC up-conversion from the triplet T_1 to the singlet S_1 state and then to use a sufficiently strong $S_1 \rightarrow S_0$ fluorescence. The SOC-induced mixing coefficient between the T_1 and S_1 states, eqn (46), (n = 1), is inversely proportional to the energy gap. This means that heavy elements are not required if the ΔE_{ST} energy gap is small and the SOC matrix element is non-vanishing.

Adachi *et al.*[28] have used a novel pathway to obtain the greatest possible electroluminescence efficiency from rather small and simple aromatic molecules, carbazolyl dicyanobenzenes (CDCB), that exhibit efficient thermally activated delayed fluorescence (TADF). In organic dyes the S_1–T_1 energy gap is usually big (0.5–1 eV) because of the large exchange integral, eqn (12), for the ππ* excitations in conjugated systems. In a series of the CDCB molecules the unusually small S_1–T_1 energy gap (less than 0.1 eV) was found because of charge transfer from the carbazolyl parts to the dicyanobenzene moiety in these excited states. In spite of the CT nature, the S_1 state has a large transition moment for the S_1–S_0 fluorescent emission due to the common area of electron density corresponding to the HOMO–LUMO deexcitation. Like in the simple example, eqn (13), both molecular orbitals should produce overlapping electron densities in order to get the large S_1–S_0 transition moment, eqn (17). In all studied CDCB molecules an efficient spin up-conversion from the non-radiative triplet state to the bright fluorescent S_1 state has been obtained.[28] The transient luminescence of all CDCB species indicates both a prompt component and a microsecond-scaled delayed emission increasing with temperature, which confirms the TADF nature. These molecules harness both S and T excitons for light emission through the S_1–S_0 channel in OLEDs composed of ITO, NPB, LiF,

Al, BCP (Fig. 5) and other carbazolyl-containing materials with an external quantum efficiency more than 19%.[28]

The lowest S_1 state in all studied metalloorganic complexes of the Pt(II) and Ir(III) ions has rather low radiative rate for transitions to the ground S_0 state (and low absorption intensity). Therefore, the ISC process (5 in Fig. 4) is highly competitive with the emission (process 4, Fig. 4). All singlet recombined e–h pairs which produce the intermediate S_1 excitons finally lead to triplet excitons by ISC. In this condition the triplet–triplet annihilation (TTA) is a parasitic phenomenon which just quenches the electroluminescence. In principle, such pure organic molecules could be chosen when the TTA rate, see k_4 and k_5 rate constants in Fig. 4, are in a proper balance so that fluorescence is relatively strong. The triplet excitons produced by e–h recombination are not emissive, but can generate the S_1 state by the TTA process. Thus, the internal quantum efficiency of fluorescence could be strongly increased and the search for such organic dyes is in steady progress.[120] The triplet–triplet annihilation processes have recently been shown to provide an attractive route to achieving high efficiencies in small molecule (SMOLED) fluorescent systems.[120,121] The 25% limit on internal quantum efficiency imposed by the S : T ratio may be boosted up to a theoretical limit of 62.5% if the materials could be designed in such a way as to harvest all the triplets generated. The analysis of the impact of TTA processes on the efficiency of a polymer (P-OLED) fluorescent system shows that an efficiency boost of ~20% can be obtained in a prototypical materials set. Introduction of a ''stable TTA'' material, designed to accept triplets and stabilize the TTA contribution, results in a dramatic improvement in device stability without loss of device efficiency.[120]

An additional way to harness triplet excitons in pure organic materials is based on the intermolecular triplet–singlet energy transfer. Combinations of various substituted carbazole compounds as the host and guest species at resonance conditions for the energy transfer between the triplet host and the S_1 state of the guest molecule have been achieved.[122] The T–S energy transfer in similar solids is well known[37a] and is realized in very efficient blue OLEDs.[122b] The delayed components of the guest fluorescence have been detected and more than 19% external quantum efficiency obtained. Carbazole is considered as one of the few molecules with both good hole transport properties and a high T_1 state energy (about 3 eV), thus its derivatives are the best host materials for blue OLEDs. It is not difficult to choose the carbazolyl derivative with the similar S_1 state energy as a guest dopant.[122] The T–S energy transfer depends on intermolecular mixing of the T and S states, which is inversely proportional to the energy gap.[122b] When the guest molecules overlap with the host species a nonzero SOC matrix element between their S and T states has been estimated.[122b] Following eqn (46), (n = 1), a high T–S energy transfer rate can be achieved because of the inverse proportionality to the T–S energy gap at the close-to-resonance conditions.

Thus, various types of delayed fluorescence originating in triplet excitons can be realized in efficient OLEDs without heavy metal dopants. Weak and proper balanced spin–orbit coupling in such organic materials is still a key issue for OLED design.

10. Conclusions

Organic molecules were considered as insulators in chemistry textbooks until the discovery of conducting polymers by Heeger, MacDiarmid and Shirakawa (Nobel Prize in chemistry in 2000). Later on small elementoorganic molecules of the Alq_3 type[10] and conjugated polymers[12,25] were found to be light-emissive upon bias in film-multilayer OLED devices. The general concept of organic electronics includes now OLEDs,[123] organic photovoltaics and thin-film transistors;[9–28] it is a fast growing field of research because of commercialization and the promising merits of being cheap, flexible, printable and technologically designable. OLEDs provide the next generation of flat panel displays because of their numerous advantages comparable with the use of liquid crystals and plasma display panels.[113] At the end of 2013 a number of companies (Samsung, Sony, LG) launched commercial OLED TV sets based on RGB platforms of organic emissive layers doped with heavy ion complexes.

In the case of pure organic fluorescent molecules and polymers about 25% internal quantum efficiency (IQE) (or 5% external quantum efficiency (EQE)) can be obtained from the singlet excited states produced by electron–hole recombination. A huge amount of electricity is spent for nothing in such OLEDs since the triplet excitons are quenched by non-radiative decay. However, the emissive layer doped by metalloorganic complexes, such as those containing Pt(II) and Ir(III) ions, can provide close to 100% IQE (about 20% of EQE) because the S and T states are mixed by effective spin–orbit coupling.

Nowadays the phosphorescent OLED devices based on Ir(III) complexes as highly efficient blue-emissive dopants have firmly entered the market. The color tuning method is widely applied to multicolor and white light OLED devices. Modern theory, like quadratic response TDDFT briefly reviewed here, can assist in the scrutiny of the details of phosphorescence and spin–orbit coupling effects for singlet–triplet state mixing in the organoiridium dyes. The required red–green–blue (RGB) primary color emitters are firmly based on the structural platform of the $[Ir(C\hat{}N)_2(L\hat{}X)]$ type of dyes reviewed here.

A theme emphasized in this review is that spin–orbit coupling plays a crucial role in modern OLEDs. The first devices made with organic polymers provided only 25% efficiency since the singlet excitons produced by electron–hole recombination were emissive and 75% of the remaining electric power spent for triplet exciton generation was wasted for heating. To produce 100% internal quantum efficiency the triplet excitons have to be involved in the light emission process. Spin–orbit coupling is very weak in organic dyes and the triplet radiative lifetime is too long to produce efficient phosphorescence in order to compete with the nonradiative decay in the polymer matrix at room temperature. In contrast, the SOC effects in Ir(III) complexes are sufficiently strong to produce mixing between the triplet and singlet states which provides effective

$T_1 \rightarrow S_0$ emission. Thus, the triplet excitons can perform useful work in OLEDs leading to an internal quantum efficiency that can reach close to 100%.

In this review we have considered basic principles and modern computational techniques to design efficient phosphorescent OLEDs. We outlined particularly important applications on elemento-organic complexes of Ir, Pt and Al ions that have been widely used in emissive layers of modern OLEDs; the calculated rate constants of their phosphorescence could be compared with the electroluminescent parameters of the devices. A prime example was the tris(8-hydroxyquinoline) aluminium complex (Alq_3) which is known to be a good fluorescent emitter, as used already in the first multilayer devices. SOC calculations show that its phosphorescence cannot be explained as a pure electronic triplet state emission without taking account of vibrations and spin–orbit–vibronic coupling, as deemed important in many cases. We showed, as an example, that such calculations can reproduce the big difference in phosphorescence lifetime between the neutral complexes of the type $[Ir(ppy)_3]$ and cationic species $[Ir(bpy)_3]^{3+}$, where ppy = 2-phenylpyridinate and bpy = 2,2′-bipyridine ligands, and could explain SOC effects on the triplet decay for the various phenylisoquinoline and fluorinated ppy ligands. The studies of different types of auxiliary ligands thus helped to explain the color tuning and decay time of Ir(III) phosphors. The first principle calculations of phosphorescence in organic and organometallic compounds provide a theoretical background for contemporary recognized and widely acknowledged ideas about the working mechanisms phosphorescent OLEDs.

However, in spite of great achievements in understanding the physical–chemical background of numerous mechanisms of charge and energy transfer, quantum-chemical simulations of elementary recombination steps and radiation processes in organic and metalloorganic species of emitting layers, a complete theoretical design of new materials for effective OLEDs is impossible. So many factors are still difficult to predict, like non-radiative rates, the length of exciton diffusion and separation between layers, the processes at interfaces, *etc.* Thus the OLED development is more a realm of the art of experiment than being a predictive and theoretically determined science. Nevertheless, key features, like the S–T states mixing, and some other crucial parameters and aspects of OLED efficiency, can be quite reliably considered by theory. The main subject of this review was to demonstrate the most important peculiarities for elementoorganic phosphors and to apply this knowledge for practical considerations in the design and fabrication of phosphorescent OLEDs.

Acronyms

Alq_3	Tris(8-hydroxyquinoline) aluminium
AM1	Austin model 1 semiempirical SCF approach
AO	Atomic orbital
B3LYP	Three-parameter Becke–Lee–Yang–Parr exchange–correlation functional
BCP	2,9-Dimethyl-4,7-diphenyl-1,10-phenanthroline
BP	Benzophenone
bpy	2,2′-Bipyridine
CBP	4,4′-*N*,*N*′-Dicarbazolebiphenyl
CDCB	Carbazolyl dicyanobenzenes
CI	Configuration interaction
CIC	Cyclometalated iridium complexes
CNDO/S	Complete neglect of differential overlap for spectroscopy semiempirical approach
CT	Charge transfer
CzVD	Carbazol–vinylene derivative
DFT	Density functional theory
DSSC	Dye-sensitized solar cells
DZR	Double zeta Rydberg basis set
ECP	Effective core potential
EDTM	Electric-dipole transition moment
e–h	Electron–hole pair
EL	Electroluminescence
EML	Emission layer
EPR	Electronic paramagnetic resonance
EQE	External quantum efficiency
ETL	Electron-transfer layer
FBP	Free-base porphine
FC	Franck–Condon factor
HBL	Hole-blocker layer
HOMO	Highest occupied molecular orbital
HTL	Hole-transport layer
INDO/S	Intermediate neglect of differential overlap for spectroscopy semiempirical approach
IQE	Internal quantum efficiency
IR	Infra-red
ISC	Intersystem crossing
ITO	Indium tin oxide
Lanl2DZ	Los Alamos National Laboratory double zeta basis set
LCM	Linear coupling model
LEC	Light-emitting electrochemical cell
LED	Light-emitting diode
LUMO	Lowest unoccupied molecular orbital
MCQR	Multi-configurational quadratic response
MLCT	Metal-to-ligand charge transfer
MO	Molecular orbital
NPB	4,4′-Bis[*N*-(1-naphthyl)-*N*-phenylamino]biphenyl
ODMR	Optical detection of magnetic resonance
OEL	Organic electroluminescence
OLEDs	Organic light-emitting diodes
PEDOT:PSS	Poly(3,4-ethylenedioxythiophene): poly(styrenesulfonate) matrix
PES	Potential energy surface
PF	Polyfluoren
PFO	Poly(9,9-di-*n*-octyl-2,7-fluorene)
PhOLEDs	Phosphorescent organic light-emitting diodes
pic	Picolinate
PMMA	Poly(methyl methacrylate)
P-OLED	Polymer organic light-emitting diode
PPV	Polyphenylene vinylene

ppy	2-Phenylpyridine anion
PT	Polythiophene
PtOEP	Octaethyl-porphine Pt(II) complex
PtP	Pt-porphyrin
PVK	Polyvinylcarbazole
QM/MM	Quantum mechanics/molecular mechanics calculations
QR	Quadratic response methodology
RGB	Red, green and blue platform
RS	Russel–Saunders scheme
S	Singlet state
SCF	Self-consistent field
SLR	Spin–lattice relaxation
SMOLED	Small molecule organic light-emitting diode
SOC	Spin–orbit coupling
SSC	Spin–spin coupling
T	Triplet state
TADF	Thermally activated delayed fluorescence
TD DFT	Time-dependent density functional theory
TTA	Triplet–triplet annihilation
WOLED	White organic light-emitting diode
ZFS	Zero-field splitting

References

1 R. Kane and H. Sell, *Revolution in Lamps: A Chronicle of 50 Years of Progress*, The Fairmont Press, Inc., 2nd edn, 2001.
2 G. Destriau, *J. Chim. Phys.*, 1936, **33**, 587.
3 J. B. Birks, *Photophysics of Aromatic Molecules*, Wiley-Interscience, London, 1970.
4 S. P. McGlynn, T. Azumi and M. Kinoshita, *Molecular Spectroscopy of the Triplet State*, Prentice Hall, Engelwood Cliffs, New Jersey, 1969.
5 A. Bernanose and P. Vouaux, *J. Chim. Phys.*, 1953, **52**, 509.
6 H. Kallman and M. Pope, *Nature*, 1960, **186**, 4718.
7 M. Pope, H. Kallman and P. Magnate, *J. Chem. Phys.*, 1963, **38**, 2042.
8 W. Helfrish and W. Schneider, *Phys. Rev. Lett.*, 1965, **14**, 229.
9 (*a*) B. Minaev, X. Li, Z. Ning, H. Tian and H. Agren, *Experimental and Theoretical Studies of New Organometallic Materials for Electroluminescent and Photovoltaic Devices in Organic Light Emitting Diodes - Material, Process and Devices*, Seung Hwan Ko, InTech, Rijeka, 2011, p. 61; (*b*) P. Vicca, S. Steudel, J. Genoe and P. Heremans, *J. Adhes. Sci. Technol.*, 2010, **24**, 1145; (*c*) Y. Yamada, K. Takeda, H. Takahashi and S. Ikegami, *J. Org. Chem.*, 2003, **68**, 7733; (*d*) Y. Koga, K. Ueno and K. Matsubara, *J. Polym. Sci., Part A: Polym. Chem.*, 2006, **44**, 4204.
10 C. Tang and S. VanSlyke, *Appl. Phys. Lett.*, 1987, **51**, 913.
11 S. Perumal, B. Minaev and H. Agren, *J. Phys. Chem. C*, 2013, **117**, 3446.
12 J. Burroughes, D. Bradley, A. Brown, R. Marks, K. MacKay, R. Friend, P. Burns and A. Holmes, *Nature*, 1990, **347**, 539.
13 (*a*) P. Stakhira, V. Cherpak, D. Volynyuk, F. Ivastchyshyn, Z. Hotra, V. Tataryn and G. Luka, *Thin Solid Films*, 2010, **518**, 7016; (*b*) S. Kappaun, C. Slugovc and E. J. W. List, *Int. J. Mol. Sci.*, 2008, **9**, 1527.
14 I. Shkrob, V. Tarasov and A. Buchachenko, *Chem. Phys.*, 1991, **153**, 443.
15 (*a*) L. Salem, *Electrons in Chemical Reactions*, J. Willey and Sons, New York, 1982; (*b*) S. Moore, *Atomic Energy Levels*, Nat. Bur. Stand., Washington, CD, 1949, p. 1952; (*c*) S. Fraga, K. M. S. Saxena and J. Karwowski, *Handbook of Atomic Data. Physical Sciences Data*, Elsevier, Amsterdam, The Netherlands, 1976, vol. 5; (*d*) P. A. Clark and J. L. Ragle, *J. Chem. Phys.*, 1967, **46**, 4235.
16 A. Monkman, H. Burrows, I. Hamblett and S. Navaratnam, *Chem. Phys. Lett.*, 2001, **340**, 467.
17 S. King, H. Vaughan and A. Monkman, *Chem. Phys. Lett.*, 2007, **440**, 268.
18 (*a*) J. Cornil, I. Gueli, A. Dkhissi, J. C. Sancho-Garcia, E. Hennebicq, J. Calbert, V. Lemaur and D. Beljonne, *J. Chem. Phys.*, 2003, **118**, 6615; (*b*) E. Doktorov, I. Malkin and V. Man'ko, *J. Mol. Spectrosc.*, 1975, **56**, 1; (*c*) P. Macak, Y. Luo and H. Agren, *Chem. Phys. Lett.*, 2000, **330**, 447; (*d*) B. Minaev, Y. H. Wang, C. K. Wang, Y. Luo and H. Agren, *Spectrochim. Acta, Part A*, 2006, **65**, 308.
19 (*a*) K. Pakbaz, C. Lee, A. Heeger, T. Hagler and D. McBranch, *Synth. Met.*, 1994, **64**, 295; (*b*) E. Conwell, *Trends Polym. Sci.*, 1997, **5**, 218.
20 (*a*) E. Jansson, P. Jha and H. Agren, *Chem. Phys.*, 2007, **336**, 91; (*b*) D. Wasserberg, S. Dudek, S. Meskers and R. Janssen, *Chem. Phys. Lett.*, 2005, **411**, 273; (*c*) E. Jansson, P. Jha and H. Agren, *Chem. Phys. Lett.*, 2006, **424**, 23.
21 W. Meeto, S. Suramitr, S. Vannarat and S. Hannongbua, *Chem. Phys.*, 2008, **349**, 1.
22 D. Beljonne, Z. Shuai, G. Pourtois and J. Bredas, *J. Phys. Chem. A*, 2001, **105**, 3899.
23 J. Cornil, D. Beljonne, C. Heller, I. Campbell and J. Bredas, *Chem. Phys. Lett.*, 1997, **278**, 139.
24 A. Monkman, C. Rothe, S. King and F. Dias, *Adv. Polym. Sci.*, 2008, **212**, 187.
25 N. Colaneri, D. Bradley, R. Friend, P. Burn, A. Holmes and C. Spangler, *Phys. Rev. B: Condens. Matter*, 1990, **42**, 11670.
26 J. Bredas, D. Beljonne, D. DosSantos and Z. Shuai, *Acc. Chem. Res.*, 1999, **32**, 267.
27 H. Gao, J. Jiang, J. Ma and Y. Luo, *J. Phys. Chem. C*, 2008, **112**, 11018.
28 H. Uoyama, K. Goushi, K. Shizu, H. Nomura and C. Adachi, *Nature*, 2012, **492**, 234.
29 A. Terenin, *Acta Physicochim. URSS*, 1943, **18**, 210.
30 M. Goeppert-Mayer and A. Sklar, *J. Chem. Phys.*, 1938, **6**, 645.
31 M. Baldo, S. Forrest and M. Thompson, in *Organic Electroluminescence*, ed. Z. H. Kafafi, Taylor and Francis, Boca Raton, 2005, p. 267.
32 (*a*) M. Baldo, D. O'Brien, Y. You, A. Shoustikov, S. Sibley, M. Thompson and S. Forrest, *Nature*, 1998, **395**, 151; (*b*) M. Baldo, S. Lomansky, P. Burrows, M. Thompson and S. Forrest, *Appl. Phys. Lett.*, 1999, **75**, 4.
33 M. Baldo and S. Forrest, *Phys. Rev. B: Condens. Matter Mater. Phys.*, 2000, **62**, 10958.

34 H. Yersin, *Highly efficient OLEDs with Phosphorescent Materials*, Wiley-VCH, 2008.
35 H. Yersin, A. Rausch, R. Czerwieniec, T. Hofbeck and T. Fischer, *Coord. Chem. Rev.*, 2011, **255**, 2622.
36 A. Terenin and A. Vartanian, *J. Phys.*, 1941, **4**, 173.
37 (*a*) A. Terenin and V. Ermolaev, *Trans. Faraday Soc.*, 1956, **52**, 1042; (*b*) V. Ermolaev, *Izv. Akad.Nauk SSSR, Ser. Fiz.*, 1963, **27**, 617.
38 B. Minaev, *Fizika Molecul, Naukova Dumka, Kiev*, 1979, **7**, 34.
39 Z. Shuai, D. Beljonne, R. Silbey and J. Bredas, *Phys. Rev. Lett.*, 2000, **84**, 131.
40 Y. Tao, C. Yang and J. Qin, *Chem. Soc. Rev.*, 2011, **40**, 2943.
41 M.-H. Tsai, H.-W. Lin, H.-C. Su, T.-H. Ke, C. Wu, F.-C. Fang, Y.-L. Liao, K.-T. Wong and C.-I. Wu, *Adv. Mater.*, 2006, **18**, 1216.
42 Y. Serebrennikov and B. Minaev, *Chem. Phys.*, 1987, **114**, 359.
43 O. Rubio-Pons, O. Loboda, B. Minaev, B. Schimmelpfenning and H. Agren, *Mol. Phys.*, 2003, **101**, 2103.
44 (*a*) O. Rubio-Pons, B. Minaev, O. Loboda and H. Agren, *Theor. Chem. Acc.*, 2004, **113**, 15; (*b*) Q. Peng, Y. Niu, Q. Shi, X. Gao and Z. Shuai, *J. Chem. Theory Comput.*, 2013, **9**, 1132; (*c*) B. F. Minaev, V. A. Minaeva, G. V. Baryshnikov, M. A. Girtu and H. Agren, *Russ. J. Appl. Chem.*, 2009, **82**, 1211.
45 J. Dekkers, G. Hoornweg, W. Cofino, C. MacLean and N. Velthorst, *Chem. Phys. Lett.*, 1979, **67**, 24.
46 H. Agren, B. Minaev and S. Knuts, *J. Phys. Chem.*, 1994, **98**, 3943.
47 (*a*) B. Minaev, *Izv. Vyssh. Uchebn. Zaved., Fiz.*, 1971, **5**, 93; (*b*) B. Minaev, *Izv. Vyssh. Uchebn. Zaved., Fiz.*, 1971, **8**, 118.
48 B. Minaev and A. F. Terpugova, *Izv. Vyssh. Uchebn. Zaved., Fiz.*, 1960, **10**, 30.
49 D. S. McClure, *J. Chem. Phys.*, 1952, **20**, 682.
50 B. Minaev, S. Knuts, H. Agren and O. Vahtras, *Chem. Phys.*, 1993, **175**, 245.
51 (*a*) B. Minaev and H. Agren, *Chem. Phys.*, 2005, **315**, 215; (*b*) I. Tunnel, Z. Rinkevicius, P. Salek, O. Vahtras and H. Agren, *J. Chem. Phys.*, 2003, **119**, 11024; (*c*) B. Minaev, I. Tunnel, P. Salek, O. Loboda, O. Vahtras and H. Agren, *Mol. Phys.*, 2004, **102**, 1391; (*d*) B. Minaev, O. Loboda, O. Vahtras, K. Ruud and H. Agren, *Theor. Chem. Acc.*, 2004, **111**, 168.
52 Y. Luo, H. Agren, S. Knuts, B. Minaev and P. Jorgensen, *Chem. Phys. Lett.*, 1993, **209**, 513.
53 (*a*) S. Knuts, B. Minaev, H. Agren and O. Vahtras, *Theor. Chim. Acta*, 1994, **87**, 343; (*b*) H. Agren, O. Vahtras and B. Minaev, *Adv. Quantum Chem.*, 1996, **27**, 71; (*c*) S. Koseki, M. Schmidt and M. Gordon, *J. Phys. Chem. A*, 1998, **102**, 10430; (*d*) S. Koseki, M. Schmidt, M. Gordon and N. Matsunaga, *J. Phys. Chem.*, 1995, **99**, 12764.
54 Y. Sun, N. Giebink, H. Kanno, B. Ma, M. Thompson and S. Forrest, *Nature*, 2006, **440**, 908.
55 (*a*) S. Reineke and M. Baldo, *Phys. Status Solidi A*, 2012, **209**, 2341; (*b*) T. Rosenow, M. Furno, S. Reineke, S. Olthof, B. Lssem and K. Leo, *J. Appl. Phys.*, 2010, **108**, 113113.
56 (*a*) A. Kohler and H. Bassler, *Mater. Sci. Eng., R*, 2009, **66**, 71; (*b*) J. S. Kim, R. H. Friend, I. Grizzi and J. H. Burroughes, *Appl. Phys. Lett.*, 2005, **87**, 023506; (*c*) S. A. Choulis, V. E. Choong, M. K. Mathai and F. So, *Appl. Phys. Lett.*, 2005, **87**, 113503.
57 (*a*) B. F. Minaev, *J. Appl. Spectrosc.*, 1985, **43**, 249; (*b*) B. F. Minaev, S. Knuts and H. Agren, *Chem. Phys.*, 1994, **181**, 15; (*c*) B. F. Minaev, *Spectrochim. Acta, Part A*, 2004, **60**, 3213.
58 (*a*) R. S. Mulliken and W. B. Person, *Molecular Complexes*, Willy Intersci. Publ., NY, 1969; (*b*) R. S. Mulliken, *J. Am. Chem. Soc.*, 1952, **74**, 811.
59 B. Minaev, H. Agren and F. De Angelis, *Chem. Phys.*, 2009, **358**, 245.
60 (*a*) B. Minaev, E. Jansson, H. Agren and S. Schrader, *J. Chem. Phys.*, 2006, **125**, 234704; (*b*) W. G. Van Dorp, W. H. Schoemaker, M. Soma and J. H. Van der Waals, *Mol. Phys.*, 1975, **30**, 1701; (*c*) B. F. Minaev and A. B. Minaev, *Opt. Spectrosc.*, 2005, **98**, 248; (*d*) P. Devolder, N. V. Dijk and H. Van der Waals, *Mol. Phys.*, 1981, **43**, 335; (*e*) O. Loboda, I. Tunell, B. Minaev and H. Agren, *Chem. Phys.*, 2005, **312**, 299; (*f*) M. P. Tsvirko, K. N. Solovjev, A. T. Gradyushko and S. S. Dvornikov, *Opt. Spectrosc.*, 1975, **38**, 400; (*g*) M. Sharnoff, *Chem. Phys. Lett.*, 1968, **2**, 498; (*h*) M. Schwoerer and H. Sixl, *Chem. Phys. Lett.*, 1968, **2**, 14; (*i*) I. Cheng and A. Kwiram, *Chem. Phys. Lett.*, 1969, **4**, 457.
61 E. Jansson, B. Minaev, S. Schrader and H. Agren, *Chem. Phys.*, 2007, **333**, 157.
62 B. Minaev, V. Minaeva and H. Agren, *J. Phys. Chem. A*, 2009, **113**, 726.
63 X. Li, B. Minaev, H. Agren and H. Tian, *Eur. J. Inorg. Chem.*, 2011, 2517.
64 X. Li, B. Minaev, H. Agren and H. Tian, *J. Phys. Chem. C*, 2011, **115**, 20724.
65 S. Tokito, M. Suzuki, F. Sato, M. Kamachi and K. Shirane, *Org. Electron.*, 2003, **4**, 105.
66 P. Coppo, E. Plummer and L. D. Cola, *Chem. Commun.*, 2004, 1774.
67 J. Slinker, A. Gorodetsky, M. Lowry, J. Wang, S. Parker, R. Rohl, S. Bernhard and G. Malliaras, *J. Am. Chem. Soc.*, 2004, **126**, 2763.
68 M. Nazeeruddin, R. Wegh, Z. Zhou, C. Klein, Q. Wang, F. D. Angelis, S. Fantacci and M. Grätzel, *Inorg. Chem.*, 2006, **45**, 9245.
69 S. Fantacci and F. D. Angelis, *Coord. Chem. Rev.*, 2011, **255**, 2704.
70 Y. You and W. Nam, *Chem. Soc. Rev.*, 2012, **41**, 7061.
71 T. Ye, J. Chen and D. Ma, *Phys. Chem. Chem. Phys.*, 2010, **12**, 15410.
72 L. Gonzlez-Urbina, S. Bonhommeau, V. Rodrigue and K. Clays, *Chem. Phys. Lett.*, 2011, **517**, 71.
73 F. Garces, K. King and R. Watts, *Inorg. Chem.*, 1988, **27**, 3464.
74 F. Garcs, K. Dedeiam, N. Keder and R. Watts, *Acta Crystallogr., Sect. C: Cryst. Struct. Commun.*, 1993, **49**, 1117.
75 R. Garcia and S. Solomon, *J. Geophys. Res.*, 1994, **99**, 12937.
76 T. Tsuboi and N. Aljaroudi, *Jpn. J. Appl. Phys.*, 2005, **44**, 591.
77 (*a*) A. Hagfeldt and M. Grätzel, *Chem. Rev.*, 1995, **95**, 49; (*b*) A. Hagfeldt and M. Grätzel, *Acc. Chem. Res.*, 2000, **33**, 269.

78 T. Meyer, *Acc. Chem. Res.*, 1978, **11**, 94.
79 (*a*) T. Tsutsui, C. Adachi and S. Saito, in *Photochemical Processes in Organized Molecular Systems*, ed. K. Honda, Elsevier, North Holland, Amsterdam, 1991, p. 445; (*b*) B. Minaev and H. Agren, *International Conference on Molecular Electronics*, Linkoping, 1993, p. 12; (*c*) S. Hoshino and H. Suzuki, *Appl. Phys. Lett.*, 1996, **69**, 224.
80 K. Nozaki, *J. Chin. Chem. Soc.*, 2006, **53**, 101.
81 J. Slinker, D. Bernards, P. Houston, H. Abruna, S. Bernhard and G. Malliaras, *Chem. Commun.*, 2003, 2392.
82 Y. Cao, I. Parker, G. Yu, C. Zhang and A. Heeger, *Nature*, 1999, **397**, 414.
83 M. Baldo, D. O'Brien, M. Thompson and S. Forrest, *Phys. Rev. B: Condens. Matter Mater. Phys.*, 1999, **60**, 14422.
84 J. Wilson, A. Dhoot, A. Seeley, M. Khan, A. Kohler and R. Friend, *Nature*, 2001, **413**, 828.
85 M. Wohlgenannt, K. Tandon, S. Mazumdar, S. Ramasesha and Z. Vardeny, *Nature*, 2001, **409**, 494.
86 Y. Noh, C. Lee, J. Kim and K. Yase, *J. Chem. Phys.*, 2003, **118**, 2853.
87 W. Finkenzeller and H. Yersin, *Chem. Phys. Lett.*, 2003, **377**, 299.
88 F. Gao and A. Bard, *J. Am. Chem. Soc.*, 2000, **122**, 7426.
89 M. Buda, G. Kalyuzhny and A. Bard, *J. Am. Chem. Soc.*, 2002, **124**, 6090.
90 F. D. Angelis, S. Fantacci, N. Evans, C. Klein, S. Zakeeruddin, J. Moser, K. Kalyanasundaram, H. Bolink, M. Grätzel and M. Nazeeruddin, *Inorg. Chem.*, 2007, **46**, 5989.
91 (*a*) H. Rudmann, S. Shimada and M. Rubner, *J. Appl. Phys.*, 2003, **94**, 115; (*b*) L. Schulz, L. Nuccio, M. Willis, P. Desai, P. Shakya, T. Kreouzis, V. K. Malik, C. Bernhard, F. L. Pratt, N. A. Morley, A. Suter, G. J. Nieuwenhuys, T. Prokscha, E. Morenzoni, W. P. Gillin and A. J. Drew, *Nat. Mater.*, 2010, **10**, 39.
92 O. Vahtras, H. Agren, J. Jorgensen, H. J. Aa. Jensen, T. Helgaker and J. Olsen, *J. Chem. Phys.*, 1992, **97**, 9178.
93 J. Olsen and P. Jorgensen, *J. Chem. Phys.*, 1985, **82**, 3235.
94 M. Casida, *THEOCHEM*, 2009, **914**, 3.
95 S. Koseki, M. Schmidt and M. Gordon, *J. Phys. Chem.*, 1992, **96**, 10768.
96 T. Matsushita, T. Asada and S. Koseki, *J. Phys. Chem. C*, 2007, **111**, 6897.
97 S. Koseki, N.-O. Kamata, T. Asada, S. Yagi, H. Nakazumi and T. Matsushita, *J. Phys. Chem. C*, 2013, **117**, 5314.
98 B. Minaev, Y.-H. Wang, C.-K. Wang, Y. Luo and H. Agren, *Spectrochim. Acta, Part A*, 2006, **65**, 308.
99 (*a*) A. Becke, *J. Chem. Phys.*, 1993, **98**, 5648; (*b*) C. Lee, W. Yang and R. G. Parr, *Phys. Rev. B*, 1988, **37**, 785.
100 P. Hay and W. Wadt, *J. Chem. Phys.*, 1985, **82**, 299.
101 M. J. Frisch, G. W. Trucks, H. B. Schlegel, G. E. Scuseria, M. A. Robb, J. R. Cheeseman, J. A. Montgomery, T. Vreven, K. N. Kudin and J. C. Burant, *et al.*, *Gaussian 03, Revision C.02*, Gaussian, Inc., Wallingford, CT, 2004.
102 W. Hehre, R. Ditchfield and J. Pople, *J. Chem. Phys.*, 1972, **56**, 2257.
103 M. Andrae, U. Haeussermann, M. Dolg, H. Stoll and H. Preuss, *Theor. Chim. Acta*, 1990, **77**, 123.
104 C. Angeli, K. L. Bak, V. Bakken, O. Christiansen, R. Cimiraglia, *et al.*, *DALTON 2011 – A molecular electronic structure program*, 2011, http://www.daltonprogram.org.
105 E. Krausz, J. Higgins and H. Reizen, *Inorg. Chem.*, 1993, **32**, 4053.
106 K. Nozaki, K. Takamori, Y. Nakatsugawa and T. Ohno, *Inorg. Chem.*, 2006, **45**, 6161.
107 O. Loboda, B. Minaev, O. Vahtras, B. Schimmelpfennig, H. Ågren, K. Ruud and D. Jonsson, *Chem. Phys.*, 2003, **286**, 127.
108 O. Vahtras, B. Minaev, O. Loboda, H. Agren and K. Ruud, *Chem. Phys.*, 2002, **279**, 133.
109 S. Clark and D. Tinti, *Chem. Phys.*, 1980, **51**, 17.
110 P. Hay, *J. Phys. Chem. A*, 2002, **106**, 1634.
111 L. Yu, G. Sriniras and M. Schwartz, *THEOCHEM*, 2003, **625**, 215.
112 W. Humbs and H. Yersin, *Inorg. Chem.*, 1996, **35**, 2220.
113 L. Xiao, Z. Chen, B. Qu, J. Luo, S. Kong, Q. Gong and J. Kido, *Adv. Mater.*, 2011, **23**, 926.
114 J. C. Deaton, R. H. Young, J. R. Lenhard, M. Rajeswaran and S. Huo, *Inorg. Chem.*, 2010, **49**, 9151.
115 T. H. Dunning and P. J. Hay, in *Modern Theoretical Chemistry*, ed. H. F. Schaefer III, Plenum, New York, 1976.
116 V. Barone and M. Cossi, *J. Phys. Chem. A*, 1998, **102**, 1995.
117 A. Endo, K. Suzuki, T. Yoshihara, S. Tobita, M. Yahiro and C. Adachi, *Chem. Phys. Lett.*, 2008, **460**, 155.
118 Y. Kawamura, K. Goushi, J. Brooks, J. J. Brown, H. Sasabe and C. Adachi, *Appl. Phys. Lett.*, 2005, **86**, 071104.
119 R. Rangi, E. A. Plummer, K. Brunner, J. W. Hofstraat, F. Babudri, G. M. Farinola, F. Naso and L. De Cola, *J. Mater. Chem.*, 2006, **16**, 1161.
120 M. Roberts, S. King, M. Cass, M. Pintani, C. Coward, N. Akino, H. Nakajima and M. Anryu, *Dig. Tech. Pap. - Soc. Inf. Disp. Int. Symp.*, 2011, **42**, 820.
121 S. M. King, M. Cass, M. Pintani, C. Coward, F. B. Dias, A. P. Monkman and M. Roberts, *J. Appl. Phys.*, 2011, **109**, 074502.
122 (*a*) A. Tomkeviciene, G. Puckyte, J. V. Grazulevicius, K. Kazlauskas, S. Jursenas and V. Jankauskas, *Dyes Pigm.*, 2013, **96**, 574; (*b*) D. Volyniuk, V. Cherpak, P. Stakhira, B. Minaev, G. Baryshnikov, M. Chapran, A. Tomkeviciene, J. Keruckas and J. V. Grazulevicius, *J. Phys. Chem. C*, 2013, **117**, 22538.
123 (*a*) M. Zhu and C. Yang, *Chem. Soc. Rev.*, 2013, **42**, 4963; (*b*) H. Sasabe and J. Kido, *Chem. Mater.*, 2011, **23**, 621; (*c*) L. Xiao, Z. Chen, B. Qu, J. Luo, S. Kong, Q. Gong and J. Kido, *Adv. Mater.*, 2011, **23**, 926; (*d*) H. Sasabe and J. Kido, *J. Mater. Chem. C*, 2013, **1**, 1699.

